Advanced materials based on carbon dots for technological applications

(Article begins on next page)

02 May 2024

Department of Electrical and Information Engineering
INDUSTRY 4.0
Ph.D. Program
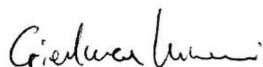SSD: CHIM/02–PHYSICAL CHEMISTRY

Final Dissertation

Advanced Materials Based on Carbon Dots for Technological Applications

by

Minervini Gianluca
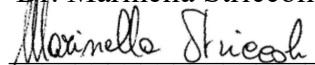
Referees:

Dr. Ermelinda Maçôas

Dr. Giulio Ragazzon

Supervisors:

Prof. Elisabetta Fanizza
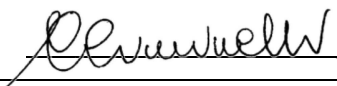
Dr. Marinella Striccoli

Dr. Annamaria Panniello

Coordinator of Ph.D Program:
Prof. Caterina Ciminelli

Course n°36, 01/11/2020-31/01/2024

Abstract

Carbon Dots (CDs), a recent class of biocompatible carbonaceous nanoparticles of only few nm in size, have the potential to permeate into the current scenario of lighting materials and transform diverse technological sectors, thanks to their unique blend of sustainability and attractive visible fluorescence. Indeed, such zero-dimensional nanostructures can be considered the carbon-based alternative to semiconductor quantum dots, awarded with the Nobel Prize in Chemistry in 2023. Respect to the quantum dots, however, challenges persist due to limited understanding of the chemical and photophysical mechanisms governing CD synthesis and optical properties. Current research aims to develop synthetic methods for controlled preparation of CDs with tailored optical properties, particularly targeting intense red emission.

This study addressed such current challenges still hindering pervasive use of CDs in technological devices. More specifically, it analyzed different bottom-up synthetic strategies, improving currently existing methodologies or contributing to develop new rational synthetic routes for CDs. Enhanced red emission components was tackled and obtained both *via* synthetic approaches and through post-synthetic coupling with plasmonic metal nanoparticles. Physicochemical properties of the synthesized CDs were accurately scrutinized, with particular attention on photophysical emission dynamics. Investigations into the resistance of CDs to photochemical degradation are pivotal for elucidating key technological aspects associated with their implementation in devices and for clarifying the contribution of molecular fluorophores to nanoparticle emission. Finally, two technological applications in lighting and chemical sensing devices, were selected for their relevance for industrial innovation and the applicative potential of synthesized CDs in these fields was demonstrated. This involved the fabrication of polymer color-conversion nanocomposites, of laser active media and of a fluorescence based portable platform for sensing of pH and antioxidant activity of chemical compounds.

Ultimately, this work joins the research community's effort to exploit the emission properties of CDs in *bottom-up* procedures, providing original perspectives and preparative strategies while highlighting crucial considerations. In the applicative sections, it contributed to facilitate solution-based processing procedures of these nanoparticles, integrating whenever possible experimental procedures with numerical optimizations, at the aim of proving the outstanding potential of CDs for the technological world.

Chapter 1 – General Introduction

Chapter 2 – Experimental Methods

Chapter 3 – Synthesis and Characterization of Carbon Dots

Chapter 4 – Photobleaching of CDs and Enhancement of Red Emission

Chapter 5 – Light Emitting Applications

Chapter 6 – Sensing Applications

List of abbreviations

Abbreviation	Definition
AA	Ascorbic acid
AIQ	Aggregation induced quenching
ALIP	Absorption loss in photobleaching
AOC	Antioxidant capacity
AuNPs	Gold nanoparticles
CA	Citric acid
CCD	Charged coupled device
CCT	Correlated Color Temperature
CDs	Carbon dots
CNDs	Carbon Nanodots
CNPs	Circular nitrocellulose pads
CoOOH	Cobalt oxyhydroxide
CQDs	Carbon Quantum Dots
CRI	Color Rendering Index
CTAB	Cetyltrimethylammonium bromide
DCDs	CDs solvothermally synthesized from citric acid, urea and Polyethyleneimine
DFT	density functional theory
DLS	Dynamic Light Scattering
DMF	N,N-dimethylformamide
EDA	Ethylenediamine
EDTA	Ethylene Diamine Tetra Acetic Acid
EG	Ethylene glycol
F-CNPs	Functionalized circular nitrocellulose pads
FCS	Fluorescence Correlation Spectroscopy
FLIP	Fluorescence loss in photobleaching
F-P	Fabry-Perot
FRAP	Fluorescence Recovery After Photobleaching
FWHM	Full width at half maximum
GIWAXS	Grazing Incidence Wide Angle X-Ray Scattering
GQDs	Graphene Quantum Dots
HDA	1-hexadecylamine

HOMO-LUMO	Highest unoccupied molecular orbital - lowest occupied molecular orbital
HPPT	4-hydroxy-1H-pyrrolo [3,4-c]pyridine-1,3,6(2H,5H)-trione
IPCA	imidazo[1,2-α]pyridine-7-carboxylic acid, 1,2,3,5-tetrahydro-5-oxo-
LOD	Limit of detection
MnO_2 NSs	Manganese dioxide nanosheets
MnO_2/GQDs	Manganese dioxide/graphene quantum dots
NIR	Near infrared
NMR	Nuclear Magnetic Resonance
NR	Neutral Red
NR-CDs	Neutral Red derived carbon dots
ODE	1-octadecene
OH-PAHs	OH-substituted polycyclic aromatic hydrocarbons
o-PD	o-phenylenediamine
ox-OPD	Oxidized o-phenylenediamine
PAHs	Polycyclic aromatic compounds
PB	Photobleaching
PDs	Polymer Dots
PEI	poly(ethyleneimine)
PI-FRAP	Partial illumination Fluorescence Recovery After Photobleaching
PLQY	Photoluminescence quantum yield
PMIA	Poly(m-phenylene isophthalamide)
p-PD	p-phenylenediamine
PRET	Plasmonic resonance energy transfer
PVA	Poly(vinyl alcohol)
QDs	Quantum dots
RCDs	Resorcinol-derived carbon dots
RE	Rare earth
RGB	Red–green–blue
RL	Random lasing
ROI	Region of interest
ROSs	Reactive oxygen species
SPR	Surface plasmon resonance
TA	Transient absorption
TCSPC	Time correlated single photon counting
TEM	Transmission electron microscopy

THF	Tetrahydrofuran
TI-FRAP	Total illumination fluorescence recovery after photobleaching
TMB	Tetramethybenzidine
TR-PL	Time-resolved photoluminescence
WLEDs	White emitting LEDs

1

General Introduction

"Nanoparticles are the tools with which we fashion new realities. Their synthesis marks the artisan's hand at the molecular level, crafting solutions that bridge the gap between the unimaginable and the achievable."

Paul L. Richards

Abstract

This chapter marks the beginning of my exploration into the realm of Carbon Dots (CDs) and their applications in the technological world. I embark on this journey by emphasizing how CDs, with their unique blend of sustainability, cost-effectiveness and compelling fluorescence properties, may impact the current development of luminescent material in various technological sectors. The chapter provides a current definition of CDs and classification of their structures. Additionally, I conduct a thorough review of methods for their synthesis and application in technological devices. Among all the possible applications of such intriguing nanomaterials, I focus on their processing for fabricating lighting devices and smart chemical sensors. The survey reported in this chapter serves as a basis for highlighting the contributions and innovative ideas presented in this thesis work with respect to the current state of research in this field.

1.1. What are Carbon Dots (CDs)?

1.1.1. The relevance of CDs in the current panorama of fluorescent materials

Fluorescent materials are ubiquitous in many technological areas: biomedical imaging, drug delivery, tissue engineering, antimicrobials, (bio)sensors, photocatalysis, photovoltaics, photonics and optoelectronics, are some notable examples [1,2]. There is no doubt that advancements towards sustainable, digital and more automated technologies will need materials with enhanced functionalities. Innovation in fluorescent materials could make a significant impact in several enabling technologies of current industrial transition, for example in sectors as healthcare, optoelectronics, automated manufacturing, anti-counterfeiting, information storage devices, photocatalysis of environmental pollutants, energy-efficient lighting devices [3–7].

In this perspective, nanoscience and nanotechnology are very good candidates to fill the gap between planning an interconnected and smarter world and realizing this project [8–10]. Especially, in the field of fluorescent materials, zero dimensional luminescent nanoparticles can be applied in several applicative areas while adding functionalities, efficiency, and optimizing benefit-cost ratios [4,11,12]. As an example, fluorescent nanoparticles could help field of light emitting diodes (LEDs) and display technology.

At present, in most commercial white emitting LEDs (WLEDs), implementation of rare earth (RE) phosphors (e.g. based on Eu, Ce, Dy, ...) in the epoxy encapsulant is necessary to convert the semiconductor chip monochromatic emission [13,14]. RE phosphor technology is highly mature. However, the preparation of these phosphors requires high temperature synthetic procedures, increasing the energy waste. Moreover, the starting materials are critical raw materials and are obtained from non-renewable sources, implying progressive increase of environmental pollution [15–17]. Thus, the European Union is spending a lot of effort investing in research, innovation and skills to replace such fluorophores with materials with lower economic and environmental impact.

As a second example, the sensor and biosensor field currently make a very widespread use of fluorescent tags, labels and other kinds of optically active trackers and/or signal generators [18–20]. Traditional materials employed for this purpose are organic molecular dyes [18,19]. Absorption and fluorescence properties of these molecules have been improved over time, to satisfy specific technological needs. Nonetheless, their synthesis typically requires multiple reaction steps, again leading to high costs and energy expenses. Additionally, molecular dyes are renown to suffer from easy degradation of their optical properties over time [21–25]. Another relevant limitation is that molecular

fluorophores must be excited in resonance with their absorption band [26–28], thereby imposing additional applicative restrictions to the employed excitation and revelation strategies.

In this panorama, colloidal quantum dots (QDs) have witnessed a huge global interest in recent past years. The awarding of the 2023 Nobel Prize in Chemistry to M. G. Bawendi, L. E. Brus, and A. Yekimov, for their discovery and development, may serve as a robust testimony to this [29]. Prototypical colloidal QDs are zero-dimensional nanoparticles of II-VI semiconductors (e.g. CdSe, CdS, PbSe, CdTe, …) in the regime of strong quantum confinement. Moreover, these nanoparticles have surface that is passivated by amphiphilic molecules, constituting an organic layer [30–32]. Nonetheless, recent nanoscience advantages have also brought to more sophisticated (and very advantageous) architectures, such as core-shell QDs or to alternative materials, such as perovskite QDs [33–36]. The attention for these photoluminescent nanoparticles is fueled by both fundamental scientific interest in their quantum-governed properties and applicative benefits that QDs may give [37]. The most widespread applications of colloidal QDs nowadays are in LEDs [38], particularly for display technology (QLED TV sets use colloidal QDs) and for biosensor screening products, where they are used for the labelling of large biomolecules. Nonetheless, many other applications at the market stage may soon find benefit from implementation of QDs [29].

The main concern associated with the use of QDs is that they contain toxic and/or polluting elements. The presence of such elements, as for example Cd or Pb, imposes that serious environmental and toxicological considerations are done to regulate the use of these colloidal nanoparticles on the global market scale [39]. In this panorama, CDs emerged as sustainable and cost-effective materials, concomitantly characterized by very intriguing fluorescence properties [40–42]. As opposed to QDs, CDs do not contain heavy metals. Moreover, they can be synthesized from inexpensive carbon sources, very often from simple, one-pot and energy-saving preparative procedures [43]. Moreover, many studies are highlighting that CDs exhibit very high characteristics of chemical stability in various environments and biocompatibility [44]. Therefore, current research on CDs is currently trying to explore different routes to prepare nanoparticles whose fluorescence can span the whole visible range. Additionally, another key point is clarifying how much these optical properties can actually impact the technological world in the different opportunities offered by the present landscape. Could transition towards carbon be the guiding line towards the advent of nanotechnology in our industry and everyday life? This is the question that leads us in the exploration of these carbon nanoparticles and all their intriguing properties.

1.1.2. Definition of CDs and their classification

CDs are zero-dimensional nanoparticles with a carbonaceous structure characterized by visible-light fluorescence. Their size is typically of 1-10 nm and they are chemically composed of light elements (C, O, H, and eventually N, S, P, B, ...) [42,45–48].

Albeit research community has been already active on the study of CDs for around 20 years, there is still no rigorous uniformly defined classification of these nanoparticles. In fact, many different classification have been proposed in the literature based on synthetic methods, crystallinity, optical properties, ...[49,50]. Concerning the structural characteristics of CDs, they can be conceptually schematized with a core-shell representation (Figure 1.1). According to this conceptualization, CDs are composed of an inner carbonaceous core and an outer surface layer [51]. The core can be generally based on either sp^2 or sp^3 carbon-based domains, eventually present in different ratios. Depending on the extension of such domains, the core can have either a graphitic crystalline structure or a carbonaceous amorphous nature. .
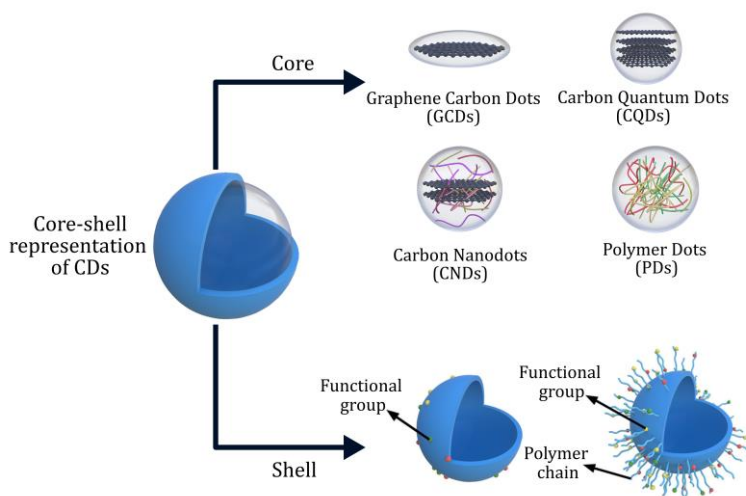
Figure 1.1: *schematic description of core-shell representation of CDs and their classification based on the crystalline structure of the carbogenic core, adapted from [51].*

Classification of CDs based on the structure and composition of their carbonaceous core is very common and widely accepted [49,52–55]. CDs with a core composed of one or a few nanometer-sized graphene layers are frequently referred to as Graphene Quantum Dots (GQDs). These stand out for having the graphene layer stacking dimension much lower than the other two dimensions, resulting in a distinctive disk shape. In contrast, Carbon Quantum Dots (CQDs)

feature multiple ordered graphene layers stacked in the core forming a spheroidal nanoparticle. Notably, both GQDs and CQDs exhibit optical fluorescence intricately linked to the quantum confinement effect, albeit with possible contributions from surface state recombinations [49,52,54,55]. When the carbonaceous core contains both ordered graphitic and amorphous domains, the nanoparticles are commonly denoted as Carbon Nanodots (CNDs). Lastly, Polymer Dots (PDs) are CDs derived from polymeric carbonaceous precursors. Thus, these consist of repeating units from polymer or co-polymer chains. They may incorporate aromatic groups forming conjugated sp^2 carbon domains or sub-fluorophore groups embedded within a cross-linked polymeric structure [56,57].

Besides the core, the CD surface can host small chemical groups with different polarity ($-OH$, $-COOH$, , $-NH_2$, $-CONH_2$, etc.). Often, these groups are inherited or formed by condensation reactions of the molecular carbonaceous precursors employed for CD synthesis. In some other cases, the surface may also contain long aliphatic carbon chains, deriving, for example, from polymers or surfactants added to synthetic mixtures.

The core-shell representation provides a very general and useful representation of CDs. Notably, this conceptualization can be also extended to CDs synthesized in this work, described in Chapter 3. In particular, CDs synthesized from citric acid (CA), urea and polyethyleneimine (DCDs, Sec. 3.1) can be regarded as CNDs with a polymeric surface. On the other hand, resorcinol derived CDs (RCDs) and Neutral Red derived CDs (NR-CDs), can be very well schematically represented as formed by molecular emitting units embedded within an amorphous carbogenic core (Sec. 3.2-3.3). This picture, in fact, emerges from a deep characterization of their physicochemical and optical properties. Therefore, following the classification above, we can regard RCDs and NR-CDs as CNDs or PDs where the inner cores contain emitting polyaromatic fluorophores.

1.2. Synthetic approaches to CDs

Developing highly fluorescent CDs with cost- and energy-effective methods in the visible range is one of the major scopes of the current scientific effort in the CD area. As a consequence, an outstanding large variety of methods has been reported so far enabling their preparation [40–42,51,58]. It has been found that CDs are frequently generated in several chemical or physical processes involving treatment of carbonaceous matter [40,59,60]; namely, broadly speaking when thermal energy or a high chemical oxidation potential is applied to a starting carbonaceous material. The most traditional way to classify these preparative approaches is the division between *top-down* and *bottom-up* approaches [61–64] (Figure 1.2).

Figure 1.2: *Schematic illustration of division between top-down and bottom-up synthetic techniques for CDs. Adapted from [65].*

In top-down methods, CDs are obtained from reduction of size of bulk carbon materials (e.g. graphite, candle soot, natural and renewable materials…) or larger carbon nanoparticles (e.g. carbon nanotubes, graphene oxide, fullerenes, …) [61,63]. The cutting can be achieved by a physical process (e.g. laser ablation, arc discharges) or by electrochemical oxidation [63].

On the other hand, in *bottom-up* approaches thermal energy is supplied to a carbon source in specific synthetic conditions to induce carbonization leading to fluorescent carbonaceous nanoparticles (Figure 1.2b). The organic precursors for these *bottom-up* approaches are typically selected based on their chemical structure and sustainability. In fact, first, it is commonly required that these molecules have some desired chemical reactivity, according to specific synthetic needs [42,47,51,59,66,67]. Moreover, cost-effectiveness, eco-sustainability and abundance of these compounds are key factors to consider, often also from the perspective of circular economy processes [60,68–70].

First, a broad distinction can be made between precursors being macromolecules or small molecules as starting materials. In the first category can be listed precursors such as polymers, biological macromolecules, organic waste or biomass (containing cellulose, lignin, and proteins) [70]. On the other hand, small

molecular precursors can be divided in three main categories considering their different chemical structures: (i) small polar organic molecules [47,66,71], (ii) aromatic or polycyclic aromatic compounds (PAHs) terminated by hydroxyl or amino groups [72,73], (iii) other small molecules selected to impart specific properties to the final nanoparticles [74–77]. Category (i) includes organic acids (e.g. CA or citrates, and Ethylene Diamine Tetra Acetic Acid (EDTA), ...), amines (e.g., urea, ethylenediamine (EDA), ...), glycols (e.g., ethylene glycol, glycerol, ...), natural carbohydrates (e.g. glucose, fructose, sucrose, ...), amino acids (e.g. tryptophane, lysine, cysteine, ...); while category (ii) includes, for example: phenols, arylamines, naphthols, amino anthracenes. Finally, examples for category (iii) may be specific organic dyes, organometallic compounds or chiral molecules [75,77]. An overview of CDs obtained from such different precursors and emitting in different regions of the visible spectrum is shown in Figure 1.3 [71].
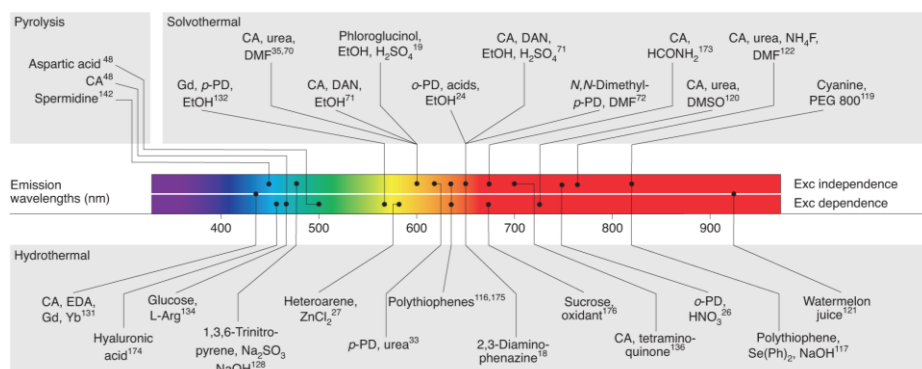
Figure 1.3: (a) overview of CDs synthesized with common bottom-up approaches and of their emission optical properties, reproduced from [71].

The synthetic mechanisms and thus the strategies to control the carbonization and the final CD properties, depend tightly on the molecular structure of the precursor [47,66,67,71]. Therefore, to better elucidate these distinctions, in the following, some relevant examples reported in the literature will be provided for each individuated category.

For the category (i), the use of CA and diamines as CD precursors holds a significant importance [66,78]. Notably, these reagents were employed in the seminal work by Zhu et al. [79], demonstrating for the first time, the *bottom-up* synthesis of blue-emitting CDs by means of a hydrothermal method. Later on, the use of CA and diamines has been thoroughly investigated in several works, varying reaction parameters, relative concentration of reagents, reaction solvent, ... Presently, these precursors have been demonstrated to produce CDs with multiple different optical properties, with single or multiple emission bands across the whole visible spectrum [47,66,67,71].

Synthesis of CDs by CA and diamines most frequently consist in hydrothermal, solvothermal or microwave treatments of these molecules. Thus, provided with thermal energy, CA and diamines give rise to different chemical processes, occurring simultaneously during the nanoparticle synthesis (Figure 1.4a) [78].
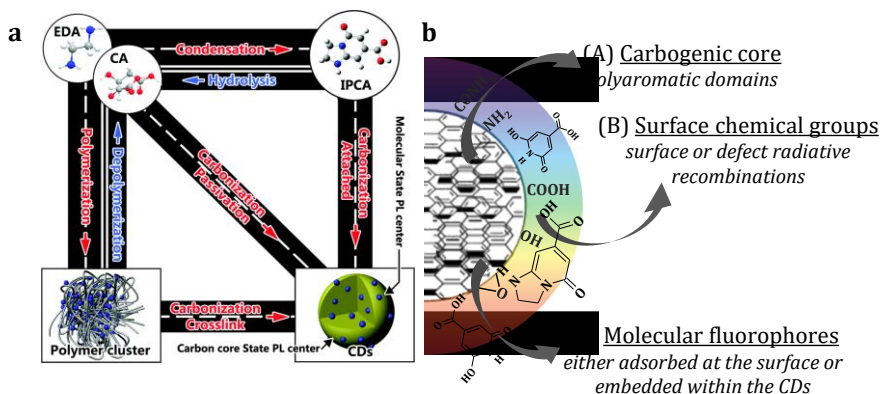
Figure 1.4: (a) schematic summary of reaction mechanisms, intermediates and products obtained in solvothermal synthesis of CDs from citric acid (CA) and ethylenediamine (EDA), reproduced from [78] and (b) schematic representation of main components contributing to the PL of CDs typically obtained from bottom-up syntheses.

Specifically, one of the reaction processes may lead to the formation of aromatic compounds with optical fluorescence in the visible region [48,78,80–82]. A notorious example of such fluorescent dyes is blue emitting imidazo[1,2-α]pyridine-7-carboxylic acid, 1,2,3,5-tetrahydro-5-oxo- (IPCA) while 4-hydroxy-1H-pyrrolo [3,4-c]pyridine-1,3,6(2H,5H)-trione (HPPT) has a green emission [83]. In general, formation of different fluorophores emitting across the whole visible spectrum has been hypothesized [48,80–82,84,85]. Besides molecular fluorophore formation, condensations between CA carboxylic and EDA amino groups can drive the carbonization *via* different pathways, including polymerization, dehydration, cross-linking, molecular fluorophore incorporation in the carbonaceous nanoparticles or its adsorption at their surface (Figure 1.4a).

As a consequence, the optical fluorescence of CDs synthesized from these precursors can mainly stem from three contributions (Figure 1.4b): polyaromatic domains in the carbogenic core, radiative recombinations at nanoparticle surface or defect states, or molecular fluorophores being either within the carbonaceous nanoparticle or adsorbed at its surface [47,48]. Often, these tree possible mechanisms co-exist in the same *bottom-up* synthesized nanoparticles, which gives rise to very complex emission characteristics and recombination dynamics [49,61,63].

Presently, the ultimate goal of these *bottom-up* CD syntheses is achieving a rational and fine modulation of the final optical properties of CDs all over the visible emission spectrum. To attain this control, several strategies have been proposed in the literature, such as: tuning opportunely the reaction conditions (e.g. temperature, pressure, microwave power, reaction time, ...), introducing "doping" elements (e.g., N, S, P, B, Fe^{3+}, Zn^{2+}, ...) to tune the emission centers in the nanoparticles, changing the reaction solvent, to obtain "solvent-engineered" CDs, altering CD surface states through nanoparticle surface modification [58,65–67,86–91] (Figure 1.5).
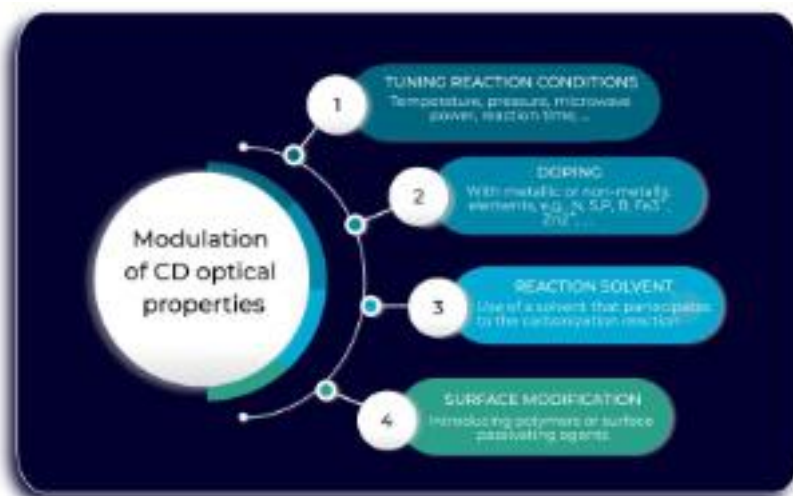
Figure 1.5: *schematic diagram of principal methods enabling modulation of CDs optical properties in bottom-up syntheses from small molecular precursors.*

Although research has been very productive in this specific synthetic pathway, some desired goals still remain elusive [49,51,71]. Specifically, numerous recent literature works emphasized that a considerable issue to overcome for these synthetic methods is the absence of uniform or standardized preparative protocols [49,92,93]. Currently, these preparative strategies may employ different synthetic setups, such as microwave, solvothermal reactors or make use of direct pyrolysis from solid state molecular precursors, or ultrasound to induce the precursor carbonization [42,60,92]. However, solvothermal reactors may differ in constructive features, according to manufacturer's specifications [94–96]. The same applies to microwave reactors, or even more remarkably for domestic microwave ovens [97,98]. Ultimately, these approaches lack in enabling precise monitoring and control of the reaction conditions (e.g. internal temperature, or eventually pressure) during the carbonization process. This results in a non-uniformity of reaction conditions actually employed in different synthetic experiments.

Furthermore, scientific literature has always denoted a poor capability of these procedures to achieve CDs emitting in the red region with high efficiencies [58,65–67,89,90]. This has been ascribed to the difficulty of obtaining sufficiently large polyaromatic structures, or poly-heteroaromatic fluorophores emitting in the red. An important consequence of this, it that it is currently difficult to attain a complete CD emission modulation covering also longer visible wavelengths. As described in Sec. 3.1, the effort in this PhD work addressed this open point, contributing to provide further insights and advancements.

The use of small polar organic molecules able to give condensation reactions for the carbonaceous core growth has as a shortcoming the difficulty of reaching a rational control over the process due to the complexity of involved reaction mechanism. On the other hand, simplifying the carbonization reaction mechanisms may lead to a better control of synthetic processes. At this scope, category (ii) precursors, namely aromatic compounds with –OH or –NH₂ functional groups were exploited as carbonaceous precursors (Figure 1.6). Thus, the formation of fluorescent polyaromatic structures proceeds through the polycondensations of the starting molecules, thereby involving a much more easily understandable mechanism.
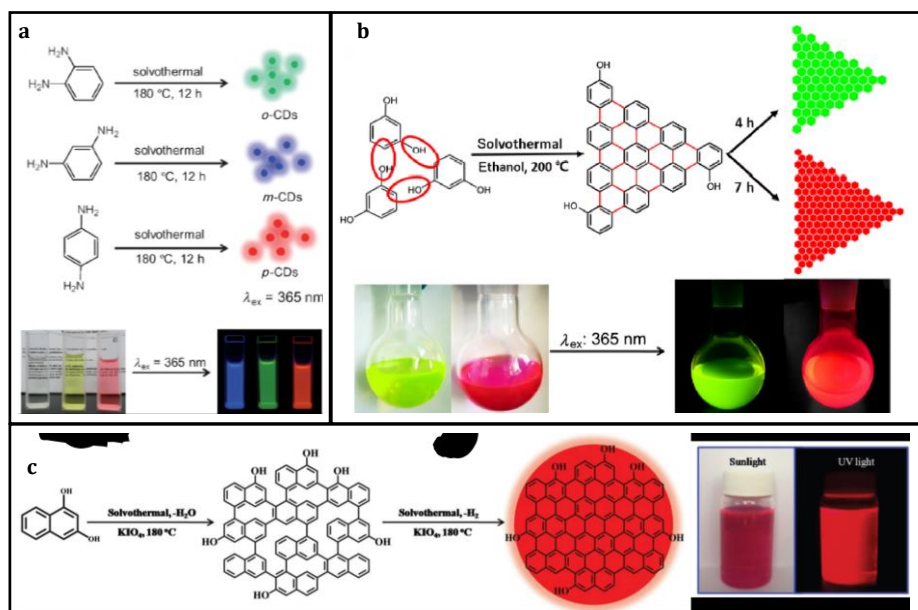
Figure 1.6: (a) preparation of red-, green- and blue-emitting CDs from three different phenylenediamine isomers, reproduced from [90]; (b) schematic description of synthesis of triangular shaped CDs by solvothermal treatment of resorcinol, reproduced from [99]; schematic diagram showing the preparation and

growth mechanism of highly efficient red emitting CDs from 1,3-dihydroxynaphthalene, adapted from [100].

A pioneering work in this context was that of Jiang et al. (2015) [90] that prepared CDs emitting blue, green, and red light from three isomers of phenylenediamine (Figure 1.3a). Aromatic amines stand out as CD precursors because N atoms embedded in planar polycyclic structures were demonstrated, in some cases, to enhance photoluminescence quantum yield (PLQY). To date, several works have employed phenylenediamines and CDs with efficient emissions ranging from blue to red have been demonstrated with these precursors [72]. Other compounds that have frequently been used to this scope are phenols with one or two hydroxyl substituents [67,99,101–109]. It is in fact known that phenolic compounds are the most prevalent class of chemicals in plants and may have structural diversity ranging from small to larger molecules [72]. Supplying thermal energy these molecules can undergo direct coupling, through condensation reactions that produce one H_2O molecule [73]. Moreover, hydroxyl substituents can also introduce oxygen defects in the polyaromatic layers, which can have different effects on their optical properties [67,102–107]. In 2018, Yuan et al. [101] employed 1,3,5-trihydroxybenzene to design triangular-shaped graphene quantum dots with variable emission from ~480 to ~600 nm according to selected reaction conditions. A year later, Yuan et al. [99] also synthesized triangular graphene quantum dots with a PL peak at 610 nm using 1,3-dihydroxybenzene (resorcinol). This precursor allowed a lowering of condensation energy barriers, thus to obtain larger conjugated polyaromatic and a PL emission below 600 nm. In the perspective of facilitating the formation of larger polycyclic domains, rather than aromatic precursors with a single ring, PAHs were tested as CD precursors [72]. Notably, Wang et al. [100] employed the 1,3-dihydroxynaphthalene, a naphthalene (the simplest PAH) substituted with two –OH groups, to synthesize CDs by a solvothermal method, making use of KIO_4 as oxidation agent, and reported the formation of red emitting CDs with unprecedented PLQY of 53%.

One of the current aims of syntheses starting from aromatic precursors is preparing CDs with exactly controlled properties, e.g. of the emission maximum wavelength [72]. This is hindered by the fact that condensation reaction mechanisms are very dependent on the employed combinations of precursors, as well as from carbonization reaction conditions. Therefore, further insights on the actual condensation mechanisms occurring during the CD synthesis are required. Furthermore, most synthetic procedures report low reaction yields of CDs or require time-consuming or solvent-expensive purification procedures, including column chromatography [72,101,108]. This hinders practical application of these CDs, especially at the industrial level. This work thus contributes to provide advancements of these points, investigating the mechanism of the formation of PAHs during CD synthesis, specifically addressing synthetic tools aimed at

increasing the reaction yields, and developing rational and environmentally friendly purification procedures (Sec. 3.2).

Lastly, in category (iii) of CD molecular precursors, specific compounds are selected to generate functional or multi-functional CDs with precisely designed properties. Very notable examples belonging to this category are the use of organic dyes to impart determined optical fluorescence to the final nanoparticles [74]. Other examples are the use of luminescent metal complexes [77] or the use of chiral molecular precursors [75].

In general, the use of these precursors implicates that the carbonization reaction has to be regarded from a different perspective. In fact, for precursor category (i) and (ii)precursors, the carbonization serves to form both optically active components (being molecular fluorophores, or polyaromatic domains) and a carbonaceous nanoparticle matrix. On the contrary, with category (iii) precursors, the final CD fluorescence properties are already encoded in the precursor molecules, while the carbonization only serve to form a carbogenic matrix that incorporates such emissive units. The advantage is that in this way, the CD fluorescence can be decided *a priori*, i.e. by selection of molecular precursor. As examples of these precursor category, Figure 1.7a shows the use of chiral compounds to obtain CDs with circularly polarized luminescence, while Figure 1.7b displays the use of a organometallic compound to obtain CDs with a dual property of fluorescence in the near infrared (NIR) and response to magnetic fields, useful for application in photodynamic therapy or local tumor treatment.
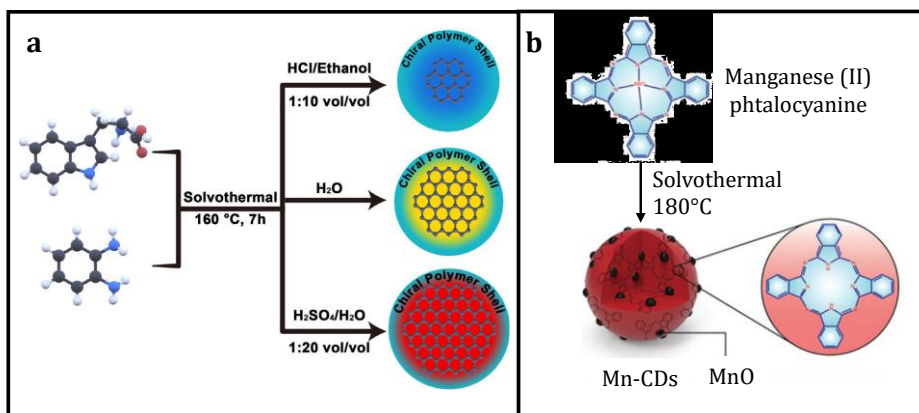
Figure 1.7: *(a) use of L-/D-tryptophan and phenylenediamine for the preparation of multicolor chiral CDs circularly polarized luminescence, adapted from [76]; (b) synthesis of magneto-fluorescent CDs using a Manganese (II) phthalocyanine as carbonaceous precursor, adapted from [77].*

For the study in Figure 1.7a, the authors employed L-/D-tryptophan and phenylenediamine to solvothermally synthesize CD emitting in the blue, yellow

and red, altering reaction conditions [77]. The obtained CDs had high PLQY ranging from 31% to 54%, that self-assembled into structures giving circularly polarized emission. On the other hand, magneto-fluorescent CDs in Figure 1.7b were synthesized by a Manganese (II) phtalocyanine; the authors further demonstrate their use as a contrast agent for both NIR fluorescence and magnetic resonance imaging. Moreover, thanks to the capability of Mn(II) of catalyzing hydrogen peroxide decomposition forming singlet oxygen, the resulting CDs demonstrated to act as sensitizers for enhanced photodynamic therapy. This work also contributes to the development of CDs with *a priori* designed optical properties. In particular, as described in Sec. 3.3, a laser dye (Neutral Red) is employed to produce nanoparticles with outstanding properties, including stimulated emission in the red.

1.3. Technological applications of CDs

Considering the unique feature of CDs of combining high sustainability with advanced optical properties, their potential impact could on several technological areas is evident. As the level of understanding and the ability to harness the optical properties of CDs increase, research is seeking to define what could be the most relevant applicative areas that might more rapidly benefit from the adoption of CDs. In general, thanks to their properties, the application of CDs is being tested in several sectors, such as: photocatalysis for the degradation of environmental pollutants [5], anti-counterfeiting [110,111], optical telecommunications [112], photovoltaics [113–115] and nanomedicine [4,60], including bioimaging [40,116] and drug delivery [44]. Within the scopes of this work, two particular areas are considered, envisioned as very promising for a CD-based technological development. These areas are the use of CDs in optoelectronic and lighting devices, particularly as color-converter materials, and the use of CDs as sensitive materials in smart chemical sensors. In Chapter 4 and Chapter 5, the experimental effort to demonstrate the full potentialities of CDs for such applications is described. In the following sections, I provide a comprehensive review on the current status on the use of fluorescent materials and specifically CDs in these specified fields. Moreover, I describe the working principles of fluorescent materials implemented in such devices, highlighting the properties that CDs should have to respond to the current requests.

1.3.1. Use of CDs in optoelectronic and lighting devices

Miniaturized optoelectronic and lighting devices are crucial for current technological progress, especially according to paradigms envisioned in the Industry 4.0 program [117–119]. Their compact size and high efficiency enable the development of smart systems with enhanced capabilities and reduced energy consumption. These devices are fundamental components to a variety of applications, including displays, devices for high-speed communication, optical data storage, optical computing, wearable devices and compact lighting solutions for machine vision systems [120–122]. By facilitating automation, improving process control, and enabling predictive maintenance, these miniaturized devices contribute significantly to the increased productivity and efficiency thus driving the digital transformation of industries.

Lasers play a key role in this scenario [123–125]. However, application of CDs for these devices is currently facing remarkable challenges [126]. Compared to other luminescent materials used as laser gain media, such as organic fluorophores, or semiconductor or perovskite QDs, CDs are very interesting due to their low toxicity and eco-friendliness [41,42,60,111]. Additionally, some reports have highlighted that CD optical properties in terms of PLQY, lifetime and photochemical stability

are compatible with achievement of lasing action in various devices with diverse configurations and geometrical characteristics [127–130]. Nonetheless, major issues for a widespread application of lasing CDs reside in the complexity and lack of precise understanding of the photophysical mechanisms underlying their optical properties. Furthermore, with most commonly employed synthetic strategies it is challenging to design accurately the CD optical properties in a way to enhance their capabilities as laser gain media. In this work, particularly with the preparation of NR-CDs (Sec. 3.3), a strategy to circumvent this issue is proposed. In fact, by using the intrinsic lasing capabilities of the starting precursor, CDs that have *a-priori* established high stimulated emission capabilities is achieved.

Notably, another class of optoelectronic devices, LEDs, only employ spontaneous emission of fluorophores, and thus could realize numerous advantages in the short term from implementation of CDs [131–133]. In recent years, LEDs have revolutionized the lighting industry, thanks to their efficiency and durability [134,135]. In response to the demand for more and more sustainable lighting solutions, CDs have emerged from the beginning of their studies as promising candidates for improving LED performance.

In principle, CDs can be employed in WLEDs either as electroluminescent active materials, or as fluorescent down-converters [62,132,136–138]. In the first case, CDs can be incorporated in a conductive polymer matrix and used as active material in a LED geometry fabricated by solution-based processing procedures [62,132,136]. In the second case, the CDs are embedded in the epoxy resin or in a coating layer situated on the top of a monochromatic semiconductor LED. Their scope is to convert the LED monochromatic light into white light.

The use of CDs in LED active layer is presently mainly limited by the need of injecting charges to create excited states in the nanoparticles, and to the fact that most CDs exhibit singlet radiative transitions [61,112]. In fact, as it has been very well established, the use of singlet fluorescent materials as active emissive centers in LEDs may limit their external quantum efficiency to around 5% [139]. On the other hand, the design of triplet-state emitting CDs that could better respond to this task is a current object of research [136,137].

Conversely, the use of CDs as fluorescent color-converters, does not imply excitation by electrical current. Therefore, these components may more rapidly support the implementation of CDs as functional materials [62,132,138]. Color-conversion-based WLEDs can be divided into four categories according to their working principle (Figure 1.8a).
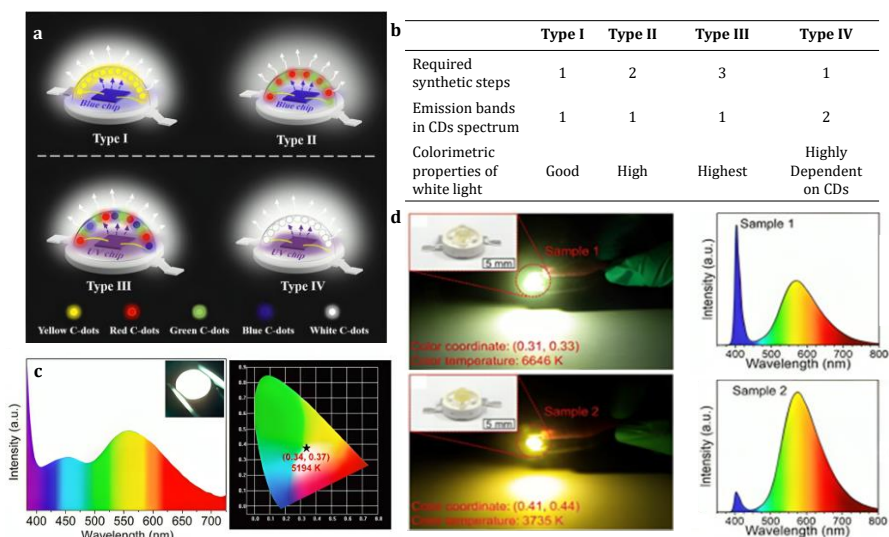
Figure 1.8: (a) four typical structures for the construction of WLEDs: blue LED with yellow emitting CDs (top-left), blue LED chip with green and red emitting CDs (top-right), UV LED with red, green, and blue emitting CDs (bottom-left), UV LED chip with white light emitting CDs (bottom-right); (b) table comparing the characteristics of Type I-IV strategies effort needed to obtain the CD fluorophores, achievable colorimetric properties of final white light (e.g., high CRI, modulable CCT, …) stability of white light color over time; examples of WLEDs fabricated using (c) Type I and (d) Type III strategies, showing device photographs and spectral and colorimetric properties. Adapted from [132]

In Type I, a blue semiconductor LED is coupled with CDs emitting yellow light [140]. A portion of the blue light emitted by the LED chip excites the CDs to emit yellow light. The remaining portion of blue light is combined with the yellow CD fluorescence resulting in white light (Figure 1.8c). In Type II, a blue LED chip is combined with CDs emitting green and red light. As in Type I, the LED serves as both an excitation light source and contributes for the blue light component to the final white light spectrum. In Type III, a UV LED chip is combined with CDs with a single-band emission in the blue, green and red (Figure 1.8d). Therefore, the primary light solely serves to excite the CDs and does not contribute to the final spectrum. Finally, in Type IV, a UV LED is paired with CDs with multiple band emission, exhibiting white light upon UV excitation.

All different strategies come with strengths and weaknesses in terms of complexity associated to fluorophore material preparation and quality of the final white light (Figure 1.8b) [132]. In Type I strategy, a single type of CD fluorophore with a yellow emission spectrum is prepared, and the final white light properties are determined by the blue spectrum and the CD PL spectrum. This may limit the

possibilities of device designers to adjust the spectral properties of the white light, potentially leading to low Color Rendering Index (CRI) and high Correlated Color Temperature (CCT), resulting in cold light with limited capability to reproduce natural colors of objects. Type II and III strategies address this limitation by using distinct CDs with green and red (for Type II) or blue, green and red (for Type III) emission bands. This results in higher CRI and enhances the flexibility in adjusting color properties. However, this obviously come with an increase in the number of synthetic steps needed to obtain the distinct fluorophores, thus increasing the effort needed for the fluorescent material preparation.

Type IV strategy involves synthesizing CDs with multiple emission bands in a single synthetic step. Thus, this strategy aims at diminishing the number of required separate CD syntheses, while the properties of the final white light will be highly dependent on the spectroscopic properties of the synthesized CDs. Specifically, this strategy requires that the emission spectrum of the CDs overall comprises two emission bands, one in the blue and one in the complementary region, covering yellow-red wavelengths. At this aim, different synthetic strategies have been proposed, namely (i) one-pot synthesis of CDs with multiple-emitting states, (ii) employment of concentration-dependent emission properties of CDs, (iii) control over aggregation in CD nanosystems in order to obtain multiple visible emission bands [141–152]. Notably, adoption of Type IV strategy implies that the properties of the CDs and their ability to produce a high-quality white light must be optimized during the one-pot preparative steps [153–161]. In Sec. 5.1, a slight modification with respect to this Type IV strategy is proposed, combining a blue LED with one-pot synthesized CDs having green-red emission bands of equal intensity. Moreover, a numerical and experimental optimization of the final white light properties is performed. Thus, this may further help to enhance white light quality and CCT versatility in these WLEDs, while at the same time reducing the complexity of their fabrication procedures.

1.3.2. Use of CDs in chemical sensing devices

In the context of advancing smart industrial technologies according to Industry 4.0 plans, developing integrable chemical sensors plays a determining role. These devices are in fact, principal responsible in real-time monitoring and control of various processes, enabling manufacturers to make informed decisions and take immediate action when necessary. Thus, these devices enable industries to ensure product quality, enhance efficiency, and maintain safety standards [162,163]. Traditional materials employed for fluorescence sensing in this area are organic dyes and molecular tags [164,165], while the use of nanoparticles has emerged in the recent years to enhance the performances and improve versatility of a broad variety of chemical sensors [166,167].

1.3.2.1.pH-sensing devices

Among the multitude of chemical sensors useful to advance smart manufacturing, pH sensors hold a central importance. In fact, these sensors are indispensable in industries such as food and beverage, agriculture, wastewater treatment, and pharmaceuticals [162,163]. In these fields in fact, maintaining given pH levels at an optimal value is often essential for several industrial processes and to ensure product quality [168–170]. CDs have attracted scientific attention as pH sensitive materials since the early stages of their discovery [171–173]. In fact, alongside with their notable attributes of high stability and low toxicity, many CDs synthesized via carbonization of water-soluble molecules display a native responsiveness of fluorescence properties to pH [172,173]. This is generally ascribed to the presence of acid/base active chemical groups (such as –COOH, –NH$_2$, –OH, ...) on their surface, while the exact mechanisms governing this pH responsivity can be various, as depicted in Figure 1.9 [171]. In particular, pH conditions can change the energy of the excited states involved in the emissive electronic transitions (Figure 1.9a), thus producing alterations spectroscopic properties of the CDs [174]. On the other hand, alterations of protonation-deprotonation equilibria of nanoparticle surface groups can lead to quenching or enhancement of PL bands related to surface state emission (Figure 1.9b) [175–179]. Furthermore, changes of CD surface charge induced from pH variations, can induce aggregation of the nanoparticles. This can cause a modification of their fluorescence (e.g. an aggregation-induced quenching) (Figure 1.9c) [180,181] Finally, some works highlighted that graphitic and/or pyridinic nitrogen present within CDs participate to protonation-deprotonation equilibria upon pH changes [182]. For example, these groups can accept protons from other surface groups upon pH decrease. This, in turn, alters the chemical composition of both surface groups and N groups, thus modifying the nanoparticle fluorescence.
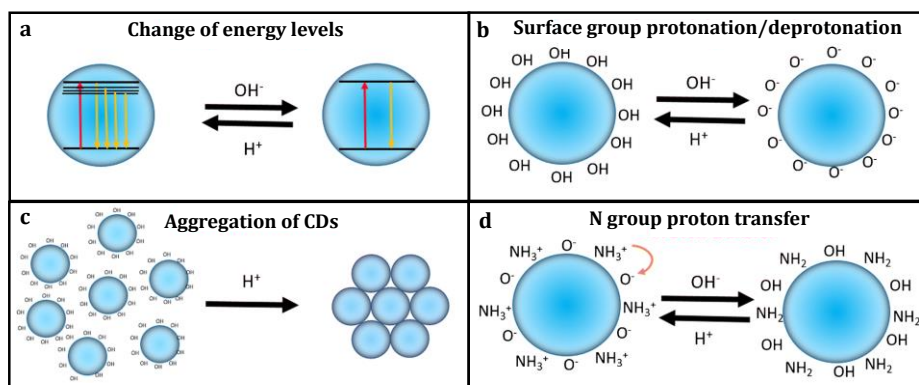
Figure 1.9*: schematic illustration of mechanisms giving CDs responsivity to pH, namely (a) change of energy level, (b) protonation and/or deprotonation of surface*

groups, (c) pH change-induced aggregation of CDs, (d) proton transfer. Adapted from [171].

These remarkable pH sensitivity led researchers to explore widely the use of CDs as pH-sensitive materials in acqueous dispersions [171–173]. More specifically, depending on their spectroscopic features, single-band emitting CDs have been employed for pH sensing based on fluorescence quenching, while multiple band emitting CDs have been often proposed for ratiometric fluorescence sensing [178,183–185]. However, using the CDs as pH sensors in aqueous dispersion inevitably entails the necessity of appropriate equipment for solution preparation and fluorescence revelation, as well as necessitating trained personnel to perform the analyses [171,186,187]. This constrains the potential applications of these nanoparticles to lab-scale analytical methodologies. On the other hand, incorporation of CDs in sensing devices can help attaining the sensing in a broader variety of operational conditions.

In a wide array of practical scenarios, pH measurements are currently performed relying on three-electrode potentiometry (pH meters) or colorimetric pH test paper strips [188–192]. These technologies for pH measurements are very well-established, nonetheless, they also have shortcomings for some practical situations. For example, potentiometric pH meters allow high-resolution and broad detectable pH range, but contend with drawbacks such as electrode vulnerability, need for large sample volumes, necessity of frequent calibration and trained operators. On the other hand, pH test strips provide rapid pH detection, yet with a much lower resolution, that is typically not higher than around ±0.5 pH units [193,194]. Additionally, some of these colorimetric tests rely on visual interpretation of the results, which is sometimes disadvantageous, as personal biases to the determined pH values can be done [195,196].

Recently, scientific effort was directed towards the development of pH sensing technologies enabling rapid and accurate responses while resulting adaptable to a broad range of demands, sample volumes, human operators [196–210]. In this direction, an intriguing approach involves introducing some technological advances to the classical colorimetric pH paper strips, leading to fabrication of more sophisticated colorimetric pH sensor devices. These devices, similarly to pH paper strips, also consist of a substrate matrix, often paper- or polymer-based, and of an active sensing material, that responds to pH variations with alterations of optical properties. The optical variations are then revealed either via naked-eye visual comparisons or via smartphone- or desktop-scanner-based detection methods [196,200,202–204,206–210].

Despite numerous examples were reported in the recent literature for the fabrication of such devices, in some cases, the presented technologies still suffer from technical limitations, such as dynamic range limited to few pH units, high

response times, need for soaking in large sample volumes, pH determination accuracy not significantly improved compared to that of commercial pH strips [197–199,201,204,205,207–210]. Moreover, some of the reported methods require multi-step elaborate fabrication procedures, such as high-resolution laser patterning of the substrate, or ink-jet printing using separate custom-made inks [196,200–203,205–210]. Consequently, there is generally still demand for development of robust colorimetric pH sensors ensuring user-friendliness and compatibility in different chemical environments. Implementation of environmentally- and cost-effective materials such as CDs in such devices has been reported only in few examples. Wang *et al.* [211] prepared pH test strips embedding orange-emitting CDs that exhibited naked-eye observable changes in fluorescence intensity across the pH range of 1-14 when examined under UV light (Figure 1.10a). Zhang *et al.* [212] ink-jet printed pieces of filter paper with tricolor emitting CDs to obtain pH test strips that could successfully measure pH in a broad range by visual inspection of color changes (Figure 1.10b). Huo et *al.* [213], reported a polymer based pH sensor based on CDs as sensing materials that, after soaking for 5 s in a buffer solution, allowed quantitative pH assessment after recording the fluorescence with a spectrofluorometer and employing fluorescence or colorimetry to quantify the sensing signal (Figure 1.10c).

Within this work, experiments carried out during my internship abroad, at the laboratories of Prof. Arben Merkoçi at ICN2, Barcelona (Spain) provided further advances to the development of smart pH portable sensors (Chapter 5). Specifically, a nitrocellulose-based platform was developed, employing RCDs as sensitive fluorescent materials, without combination with other types of nano-sensitizers. The exploited method, using a smartphone-based fluorescence colorimetric detection, shows very good performances in quantitative pH measurements (in the range of 2.2-7) with resolution up to ±0.2 pH units.
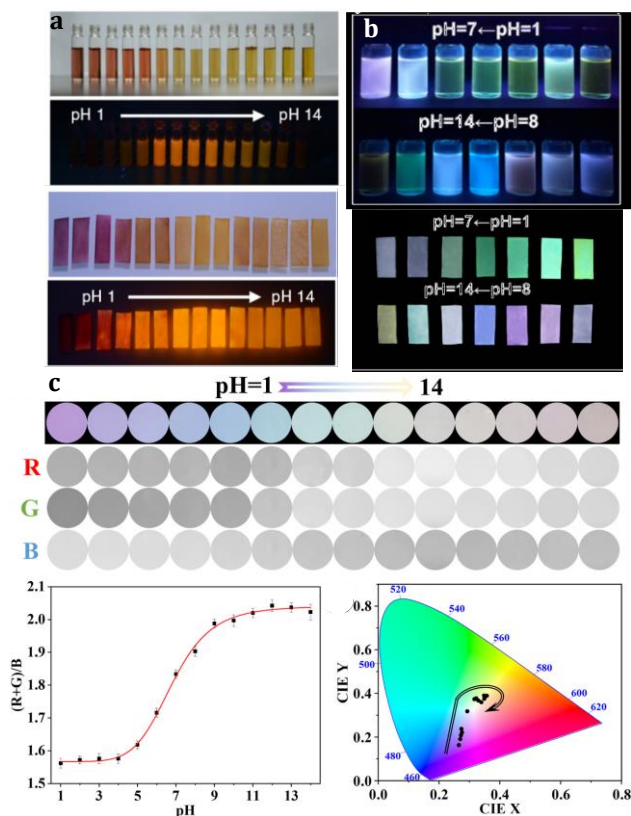
Figure 1.10: (a) use of orange-emitting CDs for pH evaluation through visual inspection: photographs of CD solutions (top) and pH test paper loaded with CDs (bottom) under visible and UV light, adapted from [211]; (b) use of CDs with three emission bands (centered at 440, 510 and 620 nm) for colorimetric visual determination of pH from 1 to 14: photographs of CD solutions and CD-loaded pH test under sunlight and 365 nm light, adapted from [212]; (c) use of multicolor CDs for pH determination via colorimetric analysis: photographs and split channel intensities (R red, B blue and G green) of CDs incorporated in a poly(m-phenylene isophthalamide) (PMIA) matrix, soaked in buffers at different pHs (top), plot and fitting curve of (R+G)/B versus pH, where R, G and B represents the intensities of the split channels (bottom-left), CIE 1931 diagram showing the obtained chromaticity coordinate change as a function of pH, adapted from [213].

1.3.2.2. Devices for sensing of antioxidant activity of chemical compounds

Within the context of advancing sensing technologies to meet the demands of accuracy in a variety of operational settings, there has been a significant increase of interest for the monitoring of the antioxidant activity, especially in food and beverage analysis [214–217]. In fact, in this sector, detection of target chemical

compounds still predominantly relies on laboratory-based protocols, requiring specific analytical instrumentation for UV-Vis spectroscopy or electrochemical signal revelation. Moreover, some of the employed protocols necessitate extraction or separation procedures, often chromatographic, which increases time and energy-consumptions as well as the need of large volumes of organic solvents [214,218]. Recent literature has presented numerous examples of sensing devices designed for assessing antioxidant capacity (AOC) of chemical compounds, avoiding the use of laboratory instrumentation. These devices mostly involve transposition of already known AOC assays on portable – e.g. paper-based– devices or rely on enzymatic activity for target antioxidant recognition [35,219–233]. The integration of nanoparticles in these devices was also shown to produce significant enhancements of the final sensing performances [166,219,220,227,231,233]. The use of CDs in such portable devices was reported in a very limited number of cases [183,233,234]. More specifically,

CDs were combined with other nanoparticles to enable specific target recognition through a specific sensing mechanism. Li et al. [233], coupled CDs with cobalt oxyhydroxide (CoOOH) nanoflakes for triple-channel (colorimetric, absorbance and fluorescence) detection of ascorbic acid (AA) in the range of 0.5-10 μM with a detection limit of 0.09 μM, also tested in real fruit juice samples. The sensing mechanism was based on the ability of AA of protecting the oxidation of p-phenylenediamine (p-PD) catalyzed by CoOOH. The CDs were employed as fluorescence sensitizers, as their PL resulted quenched by the oxidized product of p-PD. Facure et al. [234], employed a solvothermal method to obtain composites of manganese dioxide/graphene quantum dots (MnO$_2$/GQDs) exhibiting oxidase-like nanozyme activity. The MnO$_2$/GQDs were then exploited to evaluate the AOC of gallic acid, tannic acid, and AA in a colorimetric 3,3′,5,5′-tetramethybenzidine (TMB) test, showcasing promise for the development of a portable and rapid food analysis sensing device. Finally, Zhao et al. [183], developed a ratiometric fluorescence-based colorimetric sensor for portable analysis of AOC using CDs in combination with manganese dioxide nanosheets (MnO$_2$ NSs) and o-phenylenediamine (o-PD). In the absence of a target, MnO$_2$ NSs quench the PL of CDs; concurrently, MnO$_2$ NSs catalyze o-PD oxidation to a yellow fluorescent oxidized product (ox-OPD). Upon introduction of a target, MnO$_2$ NSs undergo degradation into Mn^{2+}, leading to the elimination of the fluorescence quencher and catalytic function. Consequently, the fluorescence of the CDs is restored, accompanied by a reduction in the yellow fluorescence of ox-OPD. The system fluorescence color shift from yellow to blue was quantified using a smartphone through red–green–blue (RGB) analysis. Employing glutathione as the proof-of-concept target, the detection limits were achieved at 1.84 μM and 8.33 μM for the two readout modes, fluorescence spectra, and RGB analysis, respectively. Again, the proposed strategy showed a great potential in assessing the AOC of food

samples and controlling food quality, as demonstrated using glutathione as proof-of-concept target (Figure 1.11).

Figure 1.11: *Schematic description of the working principle of a ratiometric fluorescence-based colorimetric sensor for the portable detection of antioxidants with smartphone detection, reproduced from [183].*

Notably, the nitrocellulose sensing platform developed within this thesis (Chapter 5) did not require the use of other nanoparticles or catalysts to support the sensing activity of CDs. On the contrary, alteration of RCD optical properties in response to reactive oxygen species (ROSs) was employed to monitor directly the AOC of AA. In particular, the platform proved capable of qualitative AOC evaluation of pH-dependent antioxidant activity of Vitamin C, with a limit of detection (LOD) of 20 mg/100 mL.

1.4. Objectives of the work

The present work joins current efforts in bridging the gap that separates advanced nanomaterials from their utilization in innovative technological applications. Specifically, the focus is on CDs, highly promising nanoparticles that combine environmental sustainability with very intriguing PL properties.

After the present Chapter 1, dedicated to a general overview of the state of the art regarding CD main properties, preparation methods and current research exploring also their potential in lighting and sensing application, the rest of the Thesis is structured as follows:

Chapter 2 describes the synthetic methodologies for the synthesis of CDs used in this work and the main experimental methods for their optical and morphological characterization.

Presentation and discussion of the experimental results is divided in the following chapters:

In Chapter 3, three distinct synthetic strategies for the synthesis of CDs are explored, with particular focus on structure-properties relationships. A surface passivation method allowing a modulation of CD optical properties, especially in the longer wavelength region of the visible was tested. In addition, reaction mechanisms involved in the CD formation were analyzed during the synthesis in an open reactor. Finally, an innovative approach to synthesize CDs with a-priori designed optical properties was described.

In Chapter 4 this work was committed to pinpoint and accurately characterize target properties of CDs that may constitute weak points in possible CD application. Among them, photobleaching resistance of CDs is a very critical issue, and it was thoroughly addressed. Moreover, attention was also concentrated on enhancing or self-quenching mechanisms of CD fluorescence in solid state polymeric matrices, or in association with plasmonic nanoparticles.

Chapter 5 was devoted on improving current strategies for the solution-based processing of CDs and their nanocomposites towards efficient lighting applications. The final scope is to demonstrate the effectiveness of using the synthesized CDs for the fabrication of optically active functional materials for light-emitting devices (LEDs, lasers)

Finally, in Chapter 6, the chemical sensing properties of CDs were combined with a smartphone-based fluorescence colorimetric detection to develop a portable chemical sensing platform on paper for pH and AOC, with improved resolution with respect to commercially available systems.

Overall, effort was dedicated to demonstrating the advantages and innovations that CDs can bring over currently available or marketed fluorescent materials. Concurrently, the feasibility of their manufacturing through cost-effective and easily scalable processes was pointed out.

References

[1] H.-Z. Li, F.-M. Xie, Y.-Q. Li, J.-X. Tang, J. Mater. Chem. C 11 (2023) 6471–6511.

[2] B. Pedras, ed., Fluorescence in Industry, Springer International Publishing, Cham, 2019.

[3] T.H. Kim, W. Wang, Q. Li, Front. Chem. Sci. Eng. 6 (2012) 13–26.

[4] D. Xiao, H. Qi, Y. Teng, D. Pierre, P.T. Kutoka, D. Liu, Nanoscale Res Lett 16 (2021) 167.

[5] R.M.S. Sendão, J.C.G. Esteves da Silva, L. Pinto da Silva, Catalysts 13 (2023) 179.

[6] H. Wang, X. Ji, Z.A. Page, J.L. Sessler, Mater. Chem. Front. 4 (2020) 1024–1039.

[7] A. Saravanan, P.S. Kumar, D.-V.N. Vo, P.R. Yaashikaa, S. Karishma, S. Jeevanantham, B. Gayathri, V.D. Bharathi, Environ Chem Lett 19 (2021) 441–463.

[8] K. Stopar, D. Drobne, K. Eler, T. Bartol, Scientometrics 106 (2016) 563–581.

[9] U. Finardi, C. Lamberti, J Nanopart Res 23 (2021) 7.

[10] J. Guan, Y. Shi, Scientometrics 93 (2012) 609–633.

[11] J.E. Abraham, M. Balachandran, J Fluoresc 32 (2022) 887–906.

[12] Z. Wang, T. Hu, R. Liang, M. Wei, Frontiers in Chemistry 8 (2020).

[13] W. Zhao, H. Wen, X. Yang, X. Qiao, Materials Letters 261 (2020) 127104.

[14] W. P. Lustig, Z. Shen, S. J. Teat, N. Javed, E. Velasco, D. M. O'Carroll, J. Li, Chemical Science 11 (2020) 1814–1824.

[15] K. Binnemans, P.T. Jones, B. Blanpain, T. Van Gerven, Y. Yang, A. Walton, M. Buchert, Journal of Cleaner Production 51 (2013) 1–22.

[16] L. Omodara, S. Pitkäaho, E.-M. Turpeinen, P. Saavalainen, K. Oravisjärvi, R.L. Keiski, Journal of Cleaner Production 236 (2019) 117573.

[17] A.H. Tkaczyk, A. Bartl, A. Amato, V. Lapkovskis, M. Petranikova, J. Phys. D: Appl. Phys. 51 (2018) 203001.

[18] M. Soler, L.M. Lechuga, Anal Bioanal Chem 414 (2022) 5071–5085.

[19] C. Li, A.G. Tebo, A. Gautier, International Journal of Molecular Sciences 18 (2017) 1473.

[20] H. Qu, C. Fan, M. Chen, X. Zhang, Q. Yan, Y. Wang, S. Zhang, Z. Gong, L. Shi, X. Li, Q. Liao, B. Xiang, M. Zhou, C. Guo, G. Li, Z. Zeng, X. Wu, W. Xiong, Journal of Nanobiotechnology 19 (2021) 403.

[21] S. Yadav, K. Shakya, A. Gupta, D. Singh, A.R. Chandran, A. Varayil Aanappalli, K. Goyal, N. Rani, K. Saini, Environ Sci Pollut Res 30 (2023) 71912–71932.

[22] G.P. Singh, J. Singh, K.M. Batoo, A.A. Ibrahim, O. Prakash, A.S. Nindrayog, K.J. Singh, Water Air Soil Pollut 235 (2024) 117.

[23] S. Zafar, Mohd. Shahid Khan, in: Z.H. Khan (Ed.), Emerging Trends in Nanotechnology, Springer, Singapore, 2021, pp. 359–382.

[24] P. Gheorghe, A. Petris, A.M. Anton, Polymers 16 (2024) 96.

[25] K. Mahendra, J. Anupriya, N. Gajendra, C.K. Madhusudhan, B.S. Nagaraja, J. Pattar, N.K. Udayashankar, J Mater Sci: Mater Electron 34 (2023) 730.

[26] C. Xu, W.W. Webb, J. Opt. Soc. Am. B, JOSAB 13 (1996) 481–491.

[27]   Y. Yang, F. Zhang, Eur J Nucl Med Mol Imaging 49 (2022) 3226–3246.

[28]   I. Seddiki, B.I. N'Diaye, W.G. Skene, Molecules 28 (2023) 3225.

[29]   L. Manna, Nano Lett. 23 (2023) 9673–9676.

[30]   D.L. Nida, N. Nitin, W.W. Yu, V.L. Colvin, R. Richards-Kortum, Nanotechnology 19 (2007) 035701.

[31]   P. Sarkar, S. Ghosh, K. Sarkar, Colloids and Surfaces B: Biointerfaces 197 (2021) 111382.

[32]   S. Yan, S. Tang, M. Luo, L. Xue, S. Liu, E.E. Elemike, B.S. Bae, J. Akram, J. Chen, Z. Zhao, Z. Zhu, X. Zhang, W. Lei, Q. Li, J. Mater. Chem. C 9 (2021) 10089–10100.

[33]   M. Aleksandrova, J Mater Sci: Mater Electron 33 (2022) 23900–23909.

[34]   D. Yan, M. Liu, Z. Li, B. Hou, Journal of Materials Chemistry A 9 (2021) 15522–15541.

[35]   S. Kumar, R. Singh, Q. Yang, S. Cheng, B. Zhang, B.K. Kaushik, IEEE Sensors J. (2020) 1–1.

[36]   X. Tang, J. Yang, S. Li, Z. Liu, Z. Hu, J. Hao, J. Du, Y. Leng, H. Qin, X. Lin, Y. Tian, M. Zhou, Q. Xiong, Advanced Science 6 (2019) 1900412.

[37]   D. Bera, L. Qian, T.-K. Tseng, P.H. Holloway, Materials 3 (2010) 2260–2345.

[38]   J. Chen, V. Hardev, J. Yurek, Information Display 29 (2013) 12–17.

[39]   F. Ahmad, A.K. Pandey, A.B. Herzog, J.B. Rose, C.P. Gerba, S.A. Hashsham, J Nanopart Res 14 (2012) 1038.

[40]   S. Hui, J Nanopart Res 25 (2023) 68.

[41]   D. Bharathi, B. Siddlingeshwar, R.H. Krishna, V. Singh, N. Kottam, D.D. Divakar, A.A. Alkheraif, J Fluoresc 28 (2018) 573–579.

[42]   S. Chahal, J.-R. Macairan, N. Yousefi, N. Tufenkji, R. Naccache, RSC Adv. 11 (2021) 25354–25363.

[43]   X. Zhang, M. Jiang, N. Niu, Z. Chen, S. Li, S. Liu, J. Li, ChemSusChem 11 (2018) 11–24.

[44]   R. Negro, R. Mastrogiacomo, L. Carrieri, F. Rizzi, V. Arrè, G. Minervini, E. Fanizza, G. Bianco, A. Panniello, M. Striccoli, R. Comparelli, R. Armentano, M.L. Curri, G. Giannelli, N. Depalo, M.P. Scavo, ACS Appl. Mater. Interfaces 15 (2023) 33322–33334.

[45]   J. Wan, X. Zhang, Y. Jiang, S. Xu, J. Li, M. Yu, K. Zhang, Z. Su, J. Mater. Chem. B 10 (2022) 6991–7002.

[46]   B. Han, X. Hu, X. Zhang, X. Huang, M. An, X. Chen, D. Zhao, J. Li, RSC Adv. 12 (2022) 11640–11648.

[47]   A. Sharma, J. Das, Journal of Nanobiotechnology 17 (2019) 92.

[48]   A. Sharma, T. Gadly, S. Neogy, S.K. Ghosh, M. Kumbhakar, J. Phys. Chem. Lett. 8 (2017) 1044–1052.

[49]   M.G. Giordano, G. Seganti, M. Bartoli, A. Tagliaferro, Molecules 28 (2023) 2772.

[50]   A. Banger, S. Gautam, S. Jadoun, N.K. Jangid, A. Srivastava, I.N. Pulidindi, J. Dwivedi, M. Srivastava, Catalysts 13 (2023) 858.

[51]   B. Wang, G.I.N. Waterhouse, S. Lu, Trends in Chemistry 5 (2023) 76–87.

[52]   A.M. El-Shafey, Green Processing and Synthesis 10 (2021) 134–156.

[53]   C. Hu, M. Li, J. Qiu, Y.-P. Sun, Chem. Soc. Rev. 48 (2019) 2315–2337.

[54]   V. Hinterberger, C. Damm, P. Haines, D.M. Guldi, W. Peukert, Nanoscale 11 (2019) 8464–8474.

[55]   B.D. Mansuriya, Z. Altintas, Nanomaterials 11 (2021) 2525.

[56]   S. Zhu, Y. Song, J. Shao, X. Zhao, B. Yang, Angewandte Chemie International Edition 54 (2015) 14626–14637.

[57]   L. Lin, S. Zhang, Chem. Commun. 48 (2012) 10177–10179.

[58]   Y. Huo, S. Xiu, L.-Y. Meng, B. Quan, Chemical Engineering Journal 451 (2023) 138572.

[59]   G. Ge, L. Li, D. Wang, M. Chen, Z. Zeng, W. Xiong, X. Wu, C. Guo, J. Mater. Chem. B 9 (2021) 6553–6575.

[60]   H.H. Jing, F. Bardakci, S. Akgöl, K. Kusat, M. Adnan, M.J. Alam, R. Gupta, S. Sahreen, Y. Chen, S.C.B. Gopinath, S. Sasidharan, Journal of Functional Biomaterials 14 (2023) 27.

[61]   A. Sciortino, A. Cannizzo, F. Messina, C 4 (2018) 67.

[62]   T. Yuan, T. Meng, P. He, Y. Shi, Y. Li, X. Li, L. Fan, S. Yang, J. Mater. Chem. C 7 (2019) 6820–6835.

[63]   S. Zhu, Y. Song, X. Zhao, J. Shao, J. Zhang, B. Yang, Nano Res. 8 (2015) 355–381.

[64]   Z. Li, L. Wang, Y. Li, Y. Feng, W. Feng, Materials Chemistry Frontiers 3 (2019) 2571–2601.

[65]   M.M. Hussain, W.U. Khan, F. Ahmed, Y. Wei, H. Xiong, Chemical Engineering Journal 465 (2023) 143010.

[66]   Y. Liu, F. Liang, J. Sun, R. Sun, C. Liu, C. Deng, F. Seidi, Nanomaterials 13 (2023) 2869.

[67]   M. Moniruzzaman, B. Anantha Lakshmi, S. Kim, J. Kim, Nanoscale 12 (2020) 11947–11959.

[68]   L. Chen, C.-F. Wang, C. Liu, S. Chen, Small 19 (2023) 2206671.

[69]   Y. Sahu, A. Hashmi, R. Patel, A.K. Singh, M.A.B.H. Susan, S.A.C. Carabineiro, Nanomaterials 12 (2022) 3434.

[70]   T. Li, D. Zhao, L. Li, Y. Meng, Y. Xie, D. Feng, F. Wu, D. Xie, Y. Liu, Y. Mei, Bioresource Technology 394 (2024) 130268.

[71]   L. Đorđević, F. Arcudi, M. Cacioppo, M. Prato, Nat. Nanotechnol. 17 (2022) 112–130.

[72]   S. Xue, P. Li, L. Sun, L. An, D. Qu, X. Wang, Z. Sun, Small 19 (2023) 2206180.

[73]   J. Han, J. Hong, H. Lee, S. Choi, K. Shin, M. Gu, S.-H. Kim, European Polymer Journal 197 (2023) 112354.

[74]   Y. Xu, C. Wang, H. Zhuo, D. Zhou, Q. Song, Nano Research 16 (2023).

[75]   A. Döring, E. Ushakova, A.L. Rogach, Light Sci Appl 11 (2022) 75.

[76]   Y. Ru, L. Sui, H. Song, X. Liu, Z. Tang, S.-Q. Zang, B. Yang, S. Lu, Angewandte Chemie 133 (2021) 14210–14218.

[77]   Q. Jia, J. Ge, W. Liu, X. Zheng, S. Chen, Y. Wen, H. Zhang, P. Wang, Advanced Materials 30 (2018) 1706090.

[78]   Y. Song, S. Zhu, S. Zhang, Y. Fu, L. Wang, X. Zhao, B. Yang, J. Mater. Chem. C 3 (2015) 5976–5984.

[79]   S. Zhu, Q. Meng, L. Wang, J. Zhang, Y. Song, H. Jin, K. Zhang, H. Sun, H. Wang, B. Yang, Angewandte Chemie International Edition 52 (2013) 3953–3957.

[80]   J. Schneider, C.J. Reckmeier, Y. Xiong, M. von Seckendorff, A.S. Susha, P. Kasák, A.L. Rogach, J. Phys. Chem. C 121 (2017) 2014–2022.

[81]   M. Fu, F. Ehrat, Y. Wang, K.Z. Milowska, C. Reckmeier, A.L. Rogach, J.K. Stolarczyk, A.S. Urban, J. Feldmann, Nano Lett. 15 (2015) 6030–6035.

[82]   E.A. Stepanidenko, I.A. Arefina, P.D. Khavlyuk, A. Dubavik, K.V. Bogdanov, D.P. Bondarenko, S.A. Cherevkov, E.V. Kundelev, A.V. Fedorov, A.V. Baranov, V.G. Maslov, E.V. Ushakova, A.L. Rogach, Nanoscale 12 (2020) 602–609.

[83]   W. Kasprzyk, T. Świergosz, S. Bednarz, K. Walas, N.V. Bashmakova, D. Bogdał, Nanoscale 10 (2018) 13889–13894.

[84]   X. Yao, Y. Wang, F. Li, J.J. Dalluge, G. Orr, R. Hernandez, Q. Cui, C.L. Haynes, Nanoscale 14 (2022) 9516–9525.

[85]   N.L. Kothalawala, S.W. Kim, N. Kim, C.J. Henderson, M. Seol, F. Yang, S.-Y. Kwak, K.Y. Hwang, W.-J. Son, H.-J. Shin, H. Choi, B.-S. Kim, D.Y. Kim, New J. Chem. 46 (2022) 8324–8333.

[86]   Y. Cheng, G. Yu, Molecules 28 (2023) 7473.

[87]   Z. Sun, F. Yan, J. Xu, H. Zhang, L. Chen, Nano Research 15 (2022) 414–422.

[88]   Z. He, Y. Sun, C. Zhang, J. Zhang, S. Liu, K. Zhang, M. Lan, Carbon 204 (2023) 76–93.

[89]   D. Benner, P. Yadav, D. Bhatia, Nanoscale Adv. 5 (2023) 4337–4353.

[90]   K. Jiang, S. Sun, L. Zhang, Y. Lu, A. Wu, C. Cai, H. Lin, Angewandte Chemie International Edition 54 (2015) 5360–5363.

[91]   F. Du, L.-P. Yang, L.-L. Wang, J. Mater. Chem. B 11 (2023) 8117–8135.

[92]   D.S. Chauhan, M.A. Quraishi, C. Verma, Carbon Lett. 32 (2022) 1603–1629.

[93]   D. Qu, Z. Sun, Materials Chemistry Frontiers 4 (2020) 400–420.

[94]   C.A. Zito, M.O. Orlandi, D.P. Volanti, J Electroceram 40 (2018) 271–292.

[95]   M.-R. Azani, A. Hassanpour, N. Plaia, M. Meshkat-Mamalek, Nanoscale Adv. 1 (2019) 2732–2739.

[96]   G. Demazeau, J Mater Sci 43 (2008) 2104–2114.

[97]   V.J. Law, D.P. Dowling, International Journal of Chemical Engineering 2018 (2018) e2957194.

[98]   M.P. Romero, F. Alves, M.D. Stringasci, H.H. Buzzá, H. Ciol, N.M. Inada, V.S. Bagnato, Frontiers in Microbiology 12 (2021).

[99]   F. Yuan, P. He, Z. Xi, X. Li, Y. Li, H. Zhong, L. Fan, S. Yang, Nano Res. 12 (2019) 1669–1674.

[100] Z. Wang, F. Yuan, X. Li, Y. Li, H. Zhong, L. Fan, S. Yang, Advanced Materials 29 (2017) 1702910.

[101] F. Yuan, T. Yuan, L. Sui, Z. Wang, Z. Xi, Y. Li, X. Li, L. Fan, Z. Tan, A. Chen, M. Jin, S. Yang, Nat Commun 9 (2018) 2249.

[102] T. Yoshinaga, M. Shinoda, Y. Iso, T. Isobe, A. Ogura, K. Takao, ACS Omega 6 (2021) 1741–1750.

[103] P. Yang, Z. Zhu, X. Li, T. Zhang, W. Zhang, M. Chen, X. Zhou, Journal of Alloys and Compounds 834 (2020) 154399.

[104] F. Yan, H. Zhang, N. Yu, Z. Sun, L. Chen, Sensors and Actuators B: Chemical 329 (2021) 129263.

[105] P.D. Khavlyuk, E.A. Stepanidenko, D.P. Bondarenko, D.V. Danilov, A.V. Koroleva, A.V. Baranov, V.G. Maslov, P. Kasak, A.V. Fedorov, E.V. Ushakova, A.L. Rogach, Nanoscale 13 (2021) 3070–3078.

[106] M. Sun, C. Liang, Z. Tian, E.V. Ushakova, D. Li, G. Xing, S. Qu, A.L. Rogach, J. Phys. Chem. Lett. 10 (2019) 3094–3100.

[107] J. Wang, C. Cheng, Y. Huang, B. Zheng, H. Yuan, L. Bo, M.-W. Zheng, S.-Y. Yang, Y. Guo, D. Xiao, J. Mater. Chem. C 2 (2014) 5028–5035.

[108] Y. Lu, J. Wang, H. Yuan, D. Xiao, Anal. Methods 6 (2014) 8124–8128.

[109] S. Ghosh, H. Ali, N.R. Jana, (n.d.) 12.

[110] S. Kalytchuk, Y. Wang, K. Poláková, R. Zbořil, ACS Appl. Mater. Interfaces 10 (2018) 29902–29908.

[111] M. Cheng, L. Cao, H. Guo, W. Dong, L. Li, Sensors 22 (2022) 2944.

[112] E.A. Stepanidenko, E.V. Ushakova, A.V. Fedorov, A.L. Rogach, Nanomaterials 11 (2021) 364.

[113] B. Vercelli, Coatings 11 (2021) 232.

[114] N. Gao, L. Huang, T. Li, J. Song, H. Hu, Y. Liu, S. Ramakrishna, Journal of Applied Polymer Science 137 (2020).

[115] G.A.M. Hutton, B.C.M. Martindale, E. Reisner, Chem. Soc. Rev. 46 (2017) 6111–6123.

[116] K.O. Boakye-Yiadom, (n.d.) 34.

[117] F. Yang, S. Gu, Complex Intell. Syst. 7 (2021) 1311–1325.

[118] A. Sigov, L. Ratkin, L.A. Ivanov, L.D. Xu, Inf Syst Front (2022).

[119] A. Massaro, Applied Sciences 13 (2023) 4582.

[120] H.S. Wasisto, J.D. Prades, J. Gülink, A. Waag, Applied Physics Reviews 6 (2019) 041315.

[121] H. Zhang, Y. Peng, N. Zhang, J. Yang, Y. Wang, H. Ding, Micromachines 13 (2022) 1069.

[122] P. Niu, L. Pei, Y. Mei, H. Bai, J. Shi, Applied Sciences 13 (2023) 7514.

[123] A. Sona - Cise - Segrate, in: O.D.D. Soares, M. Perez-Amor (Eds.), Applied Laser Tooling, Springer Netherlands, Dordrecht, 1987, pp. 25–41.

[124] N. Padiyakkuth, S. Thomas, R. Antoine, N. Kalarikkal, Materials Advances 3 (2022) 6687–6706.

[125] A. Gomersall, in: A. Gomersall (Ed.), Lasers in Materials Processing: A Bibliography of a Developing Technology, Springer, Berlin, Heidelberg, 1986, pp. 135–157.

[126] Y. Zhang, S. Lu, Chem 10 (2024) 134–171.

[127] Y. Zhang, L. Wang, Y. Hu, L. Sui, L. Cheng, S. Lu, Small 19 (2023) 2207983.

[128] W.-C. Liao, Y.-M. Liao, C.-T. Su, P. Perumal, S.-Y. Lin, W.-J. Lin, C.-H. Chang, H.-I. Lin, G. Haider, C.-Y. Chang, S.-W. Chang, C.-Y. Tsai, T.-C. Lu, T.-Y. Lin, Y.-F. Chen, ACS Appl. Nano Mater. 1 (2018) 152–159.

[129] Y. Ni, H. Wan, W. Liang, S. Zhang, X. Xu, L. Li, Y. Shao, S. Ruan, W. Zhang, Nanoscale 13 (2021) 16872–16878.

[130] H. Zhu, W. Zhang, S.F. Yu, Nanoscale 5 (2013) 1797.

[131] S.-N. Li, J.-L. Pan, Y.-J. Yu, F. Zhao, Y.-K. Wang, L.-S. Liao, Nanomaterials 13 (2023) 1695.

[132] C. Ji, W. Xu, Q. Han, T. Zhao, J. Deng, Z. Peng, Nano Energy 114 (2023) 108623.

[133] Q. Fu, K. Zhang, K. Lu, N. Li, S. Sun, Z. Dong, Journal of Alloys and Compounds 971 (2024) 172688.

[134] P. Meredith, A. Armin, Nature 562 (2018) 197–198.

[135] R. Soler, E. Voss, Frontiers in Neuroscience 15 (2021).

[136] T. Yuan, Q. Teng, C. Li, J. Li, W. Su, X. Song, Y. Shi, H. Xu, Y. Han, S. Wei, Y. Zhang, X. Li, Y. Li, L. Fan, F. Yuan, Mater. Horiz. 11 (2024) 102–112.

[137] C. Zhang, T. Li, Y. Zheng, M. Zhang, M. Liu, Z. Liu, K. Zhang, H. Lin, ACS Appl. Mater. Interfaces 13 (2021) 43241–43246.

[138] X. Feng, F. Zhang, Y. Wang, Y. Zhang, Y. Yang, X. Liu, Journal of Elec Materi 45 (2016) 2784–2788.

[139] H. Yersin, Highly Efficient OLEDs with Phosphorescent Materials, John Wiley & Sons, 2008.

[140] Z. Wan, Y. Li, Y. Zhou, D. Peng, X. Zhang, J. Zhuang, B. Lei, Y. Liu, C. Hu, Advanced Functional Materials 33 (2023) 2207296.

[141] X. Xu, L. Mo, Y. Li, X. Pan, G. Hu, B. Lei, X. Zhang, M. Zheng, J. Zhuang, Y. Liu, C. Hu, Advanced Materials 33 (2021) 2104872.

[142] C. Wei, S. Hu, F. Liang, Z. Song, X. Liu, Chinese Chemical Letters 33 (2022) 4116–4120.

[143] M. Madhu, T.-H. Chen, W.-L. Tseng, Journal of Colloid and Interface Science 556 (2019) 120–127.

[144] A. Panniello, A.E. Di Mauro, E. Fanizza, N. Depalo, A. Agostiano, M.L. Curri, M. Striccoli, J. Phys. Chem. C 122 (2018) 839–849.

[145] Y. Chen, M. Zheng, Y. Xiao, H. Dong, H. Zhang, J. Zhuang, H. Hu, B. Lei, Y. Liu, Advanced Materials 28 (2016) 312–318.

[146] M. Ganiga, J. Cyriac, RSC Adv. 5 (2015) 101333–101337.

[147] Y. Wang, Y. Zhao, F. Zhang, L. Chen, Y. Yang, X. Liu, New J. Chem. 40 (2016) 8710–8716.

[148] Z. Wang, Y. Liu, S. Zhen, X. Li, W. Zhang, X. Sun, B. Xu, X. Wang, Z. Gao, X. Meng, Advanced Science 7 (2020) 1902688.

[149] F. Zhang, Y. Wang, Y. Miao, Y. He, Y. Yang, X. Liu, Appl. Phys. Lett. 109 (2016) 083103.

[150] Y. Zhang, P. Zhuo, H. Yin, Y. Fan, J. Zhang, X. Liu, Z. Chen, ACS Appl. Mater. Interfaces 11 (2019) 24395–24403.

[151] K. Ahmad, A. Pal, U.N. Pan, A. Chattopadhyay, A. Paul, J. Mater. Chem. C 6 (2018) 6691–6697.

[152] Y. Zhang, J. Xiao, P. Zhuo, H. Yin, Y. Fan, X. Liu, Z. Chen, ACS Appl. Mater. Interfaces 11 (2019) 46054–46061.

[153] X. Feng, K. Jiang, H. Zeng, H. Lin, Nanomaterials 9 (2019) 725.

[154] B. Wang, H. Song, Z. Tang, B. Yang, S. Lu, Nano Res. 15 (2022) 942–949.

[155] Z. Zhou, P. Tian, X. Liu, S. Mei, D. Zhou, D. Li, P. Jing, W. Zhang, R. Guo, S. Qu, A.L. Rogach, Advanced Science 5 (2018) 1800369.

[156] J. Zheng, Y. Wang, F. Zhang, Y. Yang, X. Liu, K. Guo, H. Wang, B. Xu, J. Mater. Chem. C 5 (2017) 8105–8111.

[157] S. Lu, R. Cong, S. Zhu, X. Zhao, J. Liu, J. S.Tse, S. Meng, B. Yang, ACS Appl. Mater. Interfaces 8 (2016) 4062–4068.

[158] F. Zhang, X. Feng, Y. Zhang, L. Yan, Y. Yang, X. Liu, Nanoscale 8 (2016) 8618–8632.

[159] F. Wang, M. Kreiter, B. He, S. Pang, C. Liu, Chemical Communications 46 (2010) 3309–3311.

[160] S. Gu, C.-T. Hsieh, Y. Ashraf Gandomi, J. Li, X.X. Yue, J.-K. Chang, Nanoscale 11 (2019) 16553–16561.

[161] T. Meng, T. Yuan, X. Li, Y. Li, L. Fan, S. Yang, Chem. Commun. 55 (2019) 6531–6534.

[162] A. Varshney, N. Garg, K.S. Nagla, T.S. Nair, S.K. Jaiswal, S. Yadav, D.K. Aswal, MAPAN 36 (2021) 215–226.

[163] A.T. Rosário, J.C. Dias, Sensors 23 (2023) 1165.

[164] A.P. Demchenko, in: A.P. Demchenko (Ed.), Introduction to Fluorescence Sensing: Volume 1: Materials and Devices, Springer International Publishing, Cham, 2020, pp. 167–236.

[165] K. S, B. Sam, L. George, S.Y. N, A. Varghese, J Fluoresc 31 (2021) 1251–1276.

[166] A. Sena-Torralba, R. Álvarez-Diduk, C. Parolo, A. Piper, A. Merkoçi, Chem. Rev. 122 (2022) 14881–14910.

[167] J.-H. Song, S.-H. Min, S.-G. Kim, Y. Cho, S.-H. Ahn, Int. J. of Precis. Eng. and Manuf.-Green Tech. 9 (2022) 323–347.

[168] H. Abdulla, M. Zamorano, M.L. Rodríguez, A. El Shahawy, S. Hosny, J. Martín-Pascual, S. El-Shatoury, Appl Water Sci 13 (2022) 47.

[169] H.F. Forsan, in: G.A.M. Ali, K.F. Chong, A.S.H. Makhlouf (Eds.), Handbook of Nanosensors: Materials and Technological Applications, Springer Nature Switzerland, Cham, 2024, pp. 1–30.

[170] P.C.O. Zapata-Mendoza, O.J. Berrios-Tauccaya, V.A. Tirado-Kulieva, J.A. Gonzales-Malca, D.R. Ricse-Reyes, A.A. Berrios-Zevallos, R.S. Seminario-Sanz, Sustainability 14 (2022) 14698.

[171] H. Ehtesabi, Z. Hallaji, S. Najafi Nobar, Z. Bagheri, Microchim Acta 187 (2020) 150.

[172] V.M. Naik, S.V. Bhosale, G.B. Kolekar, Anal. Methods 14 (2022) 877–891.

[173] A.O. Adeola, A. Clermont-Paquette, A. Piekny, R. Naccache, Nanotechnology 35 (2023) 012001.

[174] S. Dutta Choudhury, J.M. Chethodil, P.M. Gharat, P. P. K., H. Pal, J. Phys. Chem. Lett. 8 (2017) 1389–1395.

[175] L. Shi, Y. Li, X. Li, B. Zhao, X. Wen, G. Zhang, C. Dong, S. Shuang, Biosensors and Bioelectronics 77 (2016) 598–602.

[176] Z. Lian Wu, M. Xuan Gao, T. Ting Wang, X. Yan Wan, L. Ling Zheng, C. Zhi Huang, Nanoscale 6 (2014) 3868–3874.

[177] M. Yang, B. Li, K. Zhong, Y. Lu, J Mater Sci 53 (2018) 2424–2433.

[178] S. Qu, H. Chen, X. Zheng, J. Cao, X. Liu, Nanoscale 5 (2013) 5514–5518.

[179] Y. Liu, Q. Zhou, International Journal of Environmental Analytical Chemistry 97 (2017) 1119–1131.

[180] C. Zheng, X. An, J. Gong, RSC Advances 5 (2015) 32319–32322.

[181] M. Omidi, A. Yadegari, L. Tayebi, RSC Advances 7 (2017) 10638–10649.

[182] Z. Qian, J. Ma, X. Shan, H. Feng, L. Shao, J. Chen, Chemistry – A European Journal 20 (2014) 2254–2263.

[183] Q. Zhao, Y. Li, W. Wei, J. Huang, D. Lu, S. Liu, X. Shi, Microchemical Journal 190 (2023) 108625.

[184] H. Nie, M. Li, Q. Li, S. Liang, Y. Tan, L. Sheng, W. Shi, S.X.-A. Zhang, Chem. Mater. 26 (2014) 3104–3112.

[185] J. Zhang, H. Chen, K. Xu, D. Deng, Q. Zhang, L. Luo, Biosensors 13 (2023) 233.

[186] A. Heering, M. Lahe, M. Vilbaste, J. Saame, J. Paulo Samin, I. Leito, Analyst (2024).

[187] L. Deleebeeck, A. Snedden, D. Nagy, Z. Szilágyi Nagyné, M. Roziková, M. Vičarová, A. Heering, F. Bastkowski, I. Leito, R. Quendera, V. Cabral, D. Stoica, Sensors 21 (2021) 3935.

[188]   by M.F. Camões, Chemistry International -- Newsmagazine for IUPAC 32 (2010) 3–7.

[189] R.P. Buck, S. Rondinini, A.K. Covington, F.G.K. Baucke, C.M.A. Brett, M.F. Camoes, M.J.T. Milton, T. Mussini, R. Naumann, K.W. Pratt, P. Spitzer, G.S. Wilson, Pure and Applied Chemistry 74 (2002) 2169–2200.

[190] H.J. Park, J.H. Yoon, K.G. Lee, B.G. Choi, Nano Convergence 6 (2019) 9.

[191] P. Spitzer, K.W. Pratt, J Solid State Electrochem 15 (2011) 69–76.

[192] W. Xiao, Q. Dong, Catalysts 12 (2022) 1124.

[193] J. Guo, L. Qiu, Z. Deng, F. Yan, Polym. Chem. 4 (2013) 1309–1312.

[194] G. Li, H. Su, N. Ma, G. Zheng, U. Kuhn, M. Li, T. Klimach, U. Pöschl, Y. Cheng, Atmos. Meas. Tech. 13 (2020) 6053–6065.

[195] A. Collins, R.B. Scott, C.R. Hirsch, C. Ottaviani, C. Krahé, F. Meeten, Biological Psychology 173 (2022).

[196] Y. Li, Y. Wang, S. Chen, Z. Wang, L. Feng, Analytica Chimica Acta 1154 (2021) 338275.

[197] D. Öztürk, İ. Ömeroğlu, B. Köksoy, C. Göl, M. Durmuş, Dyes and Pigments 205 (2022) 110510.

[198] Z. Yan, X. Zhang, C. Bao, H. Tang, Q. Zhao, L. Hu, J. You, Sensors and Actuators B: Chemical 262 (2018) 869–875.

[199] T. Taweetanavanich, B. Wanno, T. Tuntulani, B. Pulpoka, C. Kaewtong, J Chinese Chemical Soc 66 (2019) 493–499.

[200] T. Lee, H.-T. Lee, J. Hong, S. Roh, D. Yeon Cheong, K. Lee, Y. Choi, Y. Hong, H.-J. Hwang, G. Lee, Analytical Methods 14 (2022) 4749–4755.

[201] N. Pourreza, H. Golmohammadi, Talanta 131 (2015) 136–141.

[202] J. Ling, G. Naren, J. Kelly, T.S. Moody, A.P. de Silva, J. Am. Chem. Soc. 137 (2015) 3763–3766.

[203] O.R. Chanu, A. Kapoor, V. Karthik, Materials Today: Proceedings 40 (2021) S64–S68.

[204] E.V. Ermakova, A.V. Bol'shakova, A. Bessmertnykh-Lemeune, Sensors 23 (2023) 2978.

[205] T.H. Nguyen, T. Venugopala, S. Chen, T. Sun, K.T.V. Grattan, S.E. Taylor, P.A.M. Basheer, A.E. Long, Sensors and Actuators B: Chemical 191 (2014) 498–507.

[206] K. Abe, K. Suzuki, D. Citterio, Anal. Chem. 80 (2008) 6928–6934.

[207] A. Abdollahi, A. Mouraki, M.H. Sharifian, A.R. Mahdavian, Carbohydrate Polymers 200 (2018) 583–594.

[208] H. Zhang, A. Hou, K. Xie, A. Gao, Sensors and Actuators B: Chemical 286 (2019) 362–369.

[209] N. Lopez-Ruiz, V.F. Curto, M.M. Erenas, F. Benito-Lopez, D. Diamond, A.J. Palma, L.F. Capitan-Vallvey, Anal. Chem. 86 (2014) 9554–9562.

[210] S. Movafaghi, M.D. Cackovic, W. Wang, H. Vahabi, A. Pendurthi, C.S. Henry, A.K. Kota, Advanced Materials Interfaces 6 (2019) 1900232.

[211] L. Wang, M. Li, W. Li, Y. Han, Y. Liu, Z. Li, B. Zhang, D. Pan, ACS Sustainable Chem. Eng. 6 (2018) 12668–12674.

[212] T. Zhang, S. Dong, F. Zhao, M. Deng, Y. Fu, C. Lü, Sensors and Actuators B: Chemical 298 (2019) 126869.

[213] K. Huo, J. Zhang, T. Lin, Y. Zhang, Y. Liu, X. Liu, Dyes and Pigments 219 (2023) 111574.

[214] A.A. Khalil, A.A. Khan, A. Khalid, Z. Abid, C. Proestos, Z.F. Bhat, M.U. Shahbaz, R.M. Aadil, Ultrasonics Sonochemistry 98 (2023) 106534.

[215] H.S. Farah, J.F. Alhmoud, A. Al-Othman, K.M. Alqaisi, A.M. Atoom, K. Shadid, A. Shakya, T. AlQaisi, Systematic Reviews in Pharmacy 11 (2020).

[216] C. Shang, T. Zhang, J. Xu, N. Zhao, W. Zhang, M. Fan, Food Chemistry: X 19 (2023) 100790.

[217] M. Sultana, E.S. Chan, P. Janarthanan, W.S. Choo, LWT 188 (2023) 115388.

[218] V. Spínola, E.J. Llorent-Martínez, P.C. Castilho, Journal of Chromatography A 1369 (2014) 2–17.

[219] H. Guan, S. Du, B. Han, Q. Zhang, D. Wang, LWT 184 (2023) 115043.

[220] D. Calabria, M. Guardigli, P. Severi, I. Trozzi, A. Pace, S. Cinti, M. Zangheri, M. Mirasoli, Sensors 21 (2021) 5432.

[221] D.M. dos Santos, R.M. Cardoso, F.L. Migliorini, M.H.M. Facure, L.A. Mercante, L.H.C. Mattoso, D.S. Correa, TrAC Trends in Analytical Chemistry 154 (2022) 116672.

[222] M. Grossi, G. Di Lecce, M. Arru, T. Gallina Toschi, B. Riccò, Journal of Food Engineering 146 (2015) 1–7.

[223] M. Arciuli, G. Palazzo, A. Gallone, A. Mallardi, Sensors and Actuators B: Chemical 186 (2013) 557–562.

[224] I.V.S. Arantes, J.S. Stefano, R.M.F. Sousa, E.M. Richter, C.W. Foster, C.E. Banks, R.A.A. Muñoz, Electroanalysis 30 (2018) 1192–1197.

[225] M. Grossi, A. Bendini, E. Valli, T. Gallina Toschi, Sensors 23 (2023) 5002.

[226] E. Sharpe, R. Bradley, T. Frasco, D. Jayathilaka, A. Marsh, S. Andreescu, Sensors and Actuators B: Chemical 193 (2014) 552–562.

[227] X. Zhu, J. Tang, X. Ouyang, Y. Liao, H. Feng, J. Yu, L. Chen, Y. Lu, Y. Yi, L. Tang, Biosensors and Bioelectronics 216 (2022) 114652.

[228] Z.G. Cerovic, N. Moise, G. Agati, G. Latouche, N. Ben Ghozlen, S. Meyer, Journal of Food Composition and Analysis 21 (2008) 650–654.

[229] H.A.J. Al Lawati, J. Hassanzadeh, N. Bagheri, I. Al Lawati, Talanta 234 (2021) 122648.

[230] J.S. Gomes, R.M.F. de Sousa, J.F. da S. Petruci, Anal. Methods 14 (2022) 2471–2478.

[231] E. Sharpe, T. Frasco, D. Andreescu, S. Andreescu, Analyst 138 (2013) 249–262.

[232] E. Ogliani, A.L. Skov, M.A. Brook, Advanced Materials Technologies 4 (2019) 1900569.

[233] N. Li, Y.Q. Zhong, S.G. Liu, Y.Q. He, Y.Z. Fan, J.H. Hu, X. Mai, Spectrochimica Acta Part A: Molecular and Biomolecular Spectroscopy 238 (2020) 118412.

[234] M.H.M. Facure, R.S. Andre, L.A. Mercante, D.S. Correa, ACS Appl. Nano Mater. 5 (2022) 15211–15219.

2

Experimental Methods

"The experimental method is the only method of knowledge at our disposal. Everything else is poetry, imagination."

Max Planck

Abstract

This chapter discusses the more relevant experimental methods used during the research activities for nanoparticle synthesis, purification, and investigation of their properties. The synthesis of CDs is carried out using two distinct setups, being an autoclave reactor and an open round-bottom flask vessel, and emphasis is provided on the reasons for selecting these setups and their advantages in controlling reaction parameters. Purification protocols are carefully setup for each synthetic procedure and their effectiveness in removing undesired compounds is evaluated. Colloidal synthesis of gold nanoparticles (AuNPs) and their surface functionalization to promote plasmonic coupling with CDs (Sec. 4.2) is also described. The chapter further delves into spectroscopic and microscopic techniques for characterizing nanoparticle and solid-state nanocomposites properties. Particular attention is given to fluorescence measurements, as well as electron microscopy techniques used for nanoparticles and nanocomposite film investigations. In essence, this chapter serves as a comprehensive guide, offering an overview of the technical expertise essential for subsequent presentation and discussion of experimental findings in the following sections.

2.1. Experimental methods for synthesis and purification of CDs

2.1.1. Chemicals

Citric acid (anhydrous, CA, 99.5%, Sigma Aldrich), urea (99.0–100.5%, Sigma Aldrich), resorcinol (≥99%, Sigma Aldrich), neutral red (NR, Sigma-Aldrich, ≥90%), hydrogen tetrachloroaurate (III) hydrate (HAuCl$_4$,99.999%, Sigma Aldrich), sodium citrate tribasic dihydrate (≥98%, Sigma Aldrich), cetyltrimethylammonium bromide (CTAB, ≥99.0%, Fluka) poly(ethyleneimine) (PEI, average Mw ~2000, solution 50 wt.% in H$_2$O, Sigma Aldrich), polyvinylpyrrolidone (PVP, K30, Sigma Aldrich), poly(vinyl alcohol) (PVA, Mw 9000–10,000, 80% hydrolyzed, Sigma Aldrich), sodium hydroxide (NaOH, 97%, Sigma Aldrich), hydrochloric acid (HCl, 37%, Sigma Aldrich), sulfuric acid (H$_2$SO$_4$, 95.0–98.0%, Sigma Aldrich), disodium hydrogen phosphate (Na$_2$HPO$_4$, 98-100.5%, Sigma Aldrich), monosodium dihydrogen phosphate (NaH$_2$PO$_4$, ≥99.0%, Sigma Aldrich), N,N-dimethylformamide (DMF, 99.8%, Sigma Aldrich), ethylene glycol (EG, ≥ 99%, Sigma Aldrich), acetone (C$_3$H$_5$OH, ≥ 99,5%, Sigma-Aldrich), ethanol (C$_2$H$_5$OH, ≥ 99,8%, Sigma-Aldrich), hexane (C$_6$H$_{14}$, ≥ 99%, Sigma-Aldrich). All chemicals were used as supplied, without using any further purification or distillation. All aqueous solutions were prepared using MilliQ water.

2.1.2. Autoclave reactor for synthesis of CDs

Bottom-up synthesis of CDs using sealed pressurized vessels is presently widely employed [1–3]. In fact, within these reactors, attaining temperature and pressure necessary for carbonization reactions is easy and rapid [4]. However, achieving a tight control on the temperature and pressure inside such reactors, directly in the reaction media, is a crucial point. Here, an autoclave apparatus of the Parr Instrument (4590 Micro Stirred Reactors), specifically designed to allow a monitoring and a very accurate control of the temperature and pressure during the reaction process, has been used. A schematic description of the employed autoclave reactor including all its parts is shown in Figure 2.1.
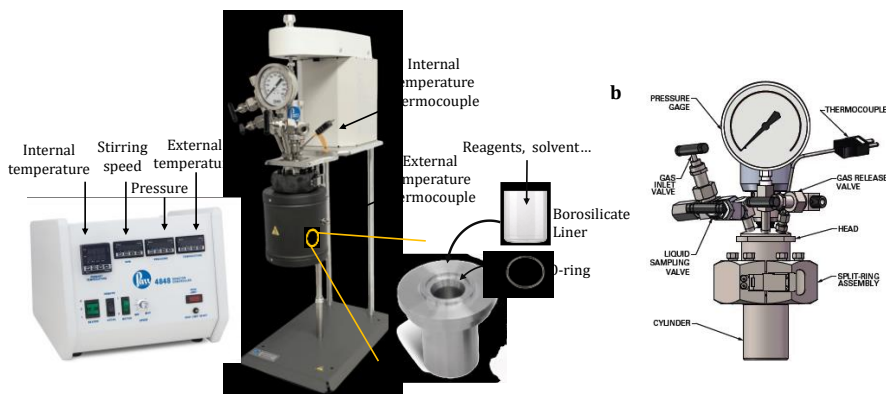
Figure 2.1*: (a) schematic description of the autoclave reactor employed for CD synthesis, including controller for selection of internal and external temperatures, stirring speed and pressure monitoring display, full photograph of the reactor with mounted heater (black cylinder), internal stainless steel vessel housing a liner that contains reactants and solvent; (b) close-up schematic diagram of the autoclave head.*

The reactor is constituted by a fixed head, at the bottom of which a 50 mL stainless-steel reactor is attached trough mechanical fastening system coupled with an O-ring. The reagents, solvents, and other chemicals are inserted into a borosilicate liner that is fitted into the vessel. Stirring of the reaction solution is possible at a controllable speed, thanks to a mechanical stirrer that can be inserted in the reaction solution from the head. The stirrer is moved by an magnetoelectrical motor situated on the back of the head (Figure2.1a). Thermal energy is provided by a heating mantle, concentric with the stainless-steel vessel. The internal reaction temperature can be set to a desired value, and the heating system, regulated by the controller, keeps the internal temperature constant for the whole duration of the reaction. Concurrently, the pressure is monitored continuously by a sensor installed in the head (Figure 2.1b) that is in communication with the reaction chamber.

Within this thesis, the autoclave reactor was employed for the synthesis of DCDs (Sec. 3.1) and for CDs prepared using as NR dye as starting precursor (NR-CDs, Sec. 3.3).

2.1.3. Round-bottom flask open reactor synthesis of CDs

Another option to provide an even tighter control of the reaction conditions is employing an open reaction vessel. In fact, this experimental setup allows concomitantly to access the reaction solution during the synthesis, which is very useful to monitor spectroscopically the carbonization process. A photograph and schematic description of the round-bottom flask reactor are shown in Figure 2.2.
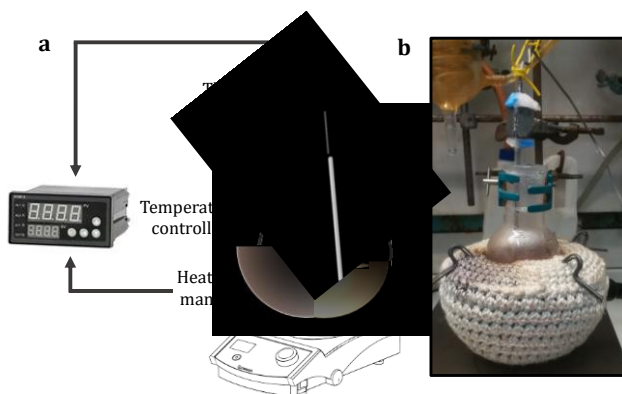
Figure 2.2: *(a) schematic description and (b) photograph of the open round-bottom flask apparatus employed for CD synthesis.*

The apparatus consists of a round-bottom flask inserted into a heating mantle. A thermocouple is also placed inside the reaction mixture to continuously measure its temperature over the reaction time. Both the heating mantle and the thermocouple are connected to a temperature controller that displays the current measured temperature and maintains it fixed to a selected value with a feedback control system. Continuous magnetic stirring is provided for the whole duration of the reaction by means of a magnetic anchor inserted in the reaction vessel and manipulated by a stirring plate underneath the heating mantle. Such open vessel was employed for the synthesis of RCDs (Sec. 3.2).

2.1.4. Purification methods of CDs

The raw reaction products were purified to remove undesired molecular reaction byproducts. The purification methods consisted in several steps of precipitation by centrifugation and redispersion of the collected precipitates. This was performed employing an opportune aqueous solution or solvent mixture to allow progressive dissolution of molecular byproducts and hence, at every cycle, their progressive removal from the nanoparticle precipitate. Separation of nanoparticles and molecular byproducts was therefore based on their different solubility in the employed solution or solvent mixture.

Purification of CDs synthesized by bottom-up carbonization methods is a still widely debated issue, and several purification techniques including dialysis, gel electrophoresis, chromatography and Nuclear Magnetic Resonance (NMR) spectroscopy have been proposed to deeply investigate the purification process of these nanoparticles [5,6]. Whitin this work, spectroscopic monitoring of either the precipitates or the supernatant phases obtained at every cycle was employed to ascertain the effectiveness of the purification process. Spectroscopic data and

further experimental details specific to each of the CD syntheses analyzed in this work are reported in Sec. 2.15-2.1.7. This spectroscopic monitoring allows to infer a significant removal of molecular byproducts showing absorption and/or fluorescence signals overlapping with those of the purified precipitates. Moreover, the presence of a residual molecular component in the purified products is further investigated case-by-case with careful characterizations of physicochemical and optical properties of the purified CDs (Sec. 3.1-3.3). On the other hand, precise identification and molecular structure characterization of molecular reaction side products is beyond the scope of this work.

2.1.5. Synthesis and purification of in-situ polymer passivated CDs synthesized from citric acid and urea (DCDs)

1.8 g of citric acid, 3.6 g of urea (molar ratio of 1:7) and 0.014 g of PEI (0.02 mM) were dissolved into 18 mL of DMF until forming an optically clear solution. Such solution was subsequently transferred into the borosilicate liner and heated in the autoclave reactor at 160°C for 6 h. At the end of the solvothermal treatment, the resulting crude reaction batch appeared to be dark-brown and opaque, remarking the occurrence of a carbonization process. Next, an effective purification procedure was carried out to remove un-reacted precursors.

For purifying the raw product, 5% HCl_{aq} was initially added in a volume ratio of around 1:10. After vigorous stirring, the acidified mixture was then centrifuged at 10krpm for 10 min; the dark precipitate was collected and afterwards further purified through several cycles of washing with 0.5% HCl_{aq} and successive centrifugation. The purification cycles were terminated when UV-Vis absorption characteristics of molecular components were no longer discernible in the supernatants (Figure 2.3, for complete discussion and attributions of observed bands in the UV-Vis absorption spectra see Sec. 3.1). Finally, the precipitate was dispersed in a 250 mM NaOH aqueous solution and freeze-dried before storing for further uses.
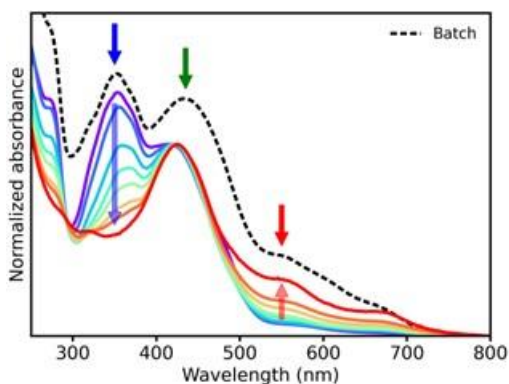
Figure 2.3: *UV-Vis absorption spectra of DCDs crude reaction batch (dashed black line) and of supernatants discarded at each purification step (colored lines from violet to red at increasing number of washing step).*

2.1.6. Synthesis and purification of resorcinol-derived CDs (RCDs)

For the synthesis of RCDs (n-RCDs), first, EG (12 mL) was heated at 180°C in a round bottom flask; then, a solution of resorcinol (1.5 g) in EG (3 mL) was quickly injected through a syringe. Subsequently, the system was allowed to react at 180°C for 6 h. During the whole duration of the reaction, the vessel was kept open, and the temperature set constant. For the synthesis of RCDs in presence of a catalyst, namely NaOH base catalyst (b-RCDs) and H_2SO_4 acid catalyst (a-RCDs), soon after the injection of the resorcinol solution, 500 μL of a 2 M aqueous solution of either NaOH or H_2SO_4 were quickly injected into the reaction vessel.

The obtained n-RCDs, b-RCDs and a-RCDs were purified by washing with a diluted ($\sim 10^{-4}$ M) HCl aqueous solution. In details, 2 mL of the raw reaction batch were mixed with 5 mL of HCl solution under vigorous stirring. Then, this solution was centrifuged (at 9000 rpm for 30 min), and a dark brown precipitate was obtained. The solid precipitate was further dispersed and centrifuged, repeating the same procedure 4 times. At the end of the purification, the dark precipitate was dried under vacuum and then weighted to calculate the mass reaction yield. Ethanol or acqueous solutions employed for nanoparticle characterization and further experiments were obtained dispersing the as-obtained purified dark powders.

UV-Vis absorption spectra were recorded at each purification step to evaluate the effectiveness of the purification procedure (Figure 2.4a).
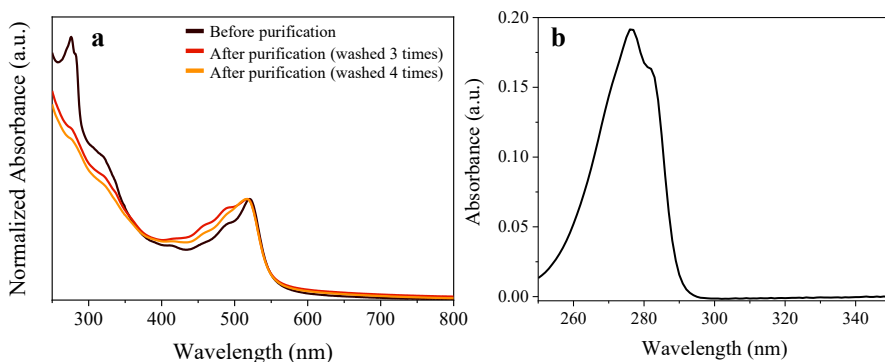
Figure 2.4: (a) UV absorption spectrum of resorcinol in an ethanol solution; (b) UV-Vis absorption spectra of n-RCDs recorded before the purification (black line) and after purification consisting in washing 3 times (red line) and 4 times (blue line) with a ~10⁻⁴ M aqueous solution of HCl.

Figure 2.4a clearly shows that a component in the UV is markedly eliminated after repeated purification cycles. This component is ascribable to the characteristic resorcinol absorption band at 276 nm, shown in Figure 2.4b for reference. This proves that the purification protocol is successfully able to remove unreacted precursor from the purified nanoparticle precipitate.

2.1.7. Synthesis and purification of Neutral Red derived CDs (NR-CDs)

0.8 g of NR were dissolved in 20 mL of EG, keeping the mixture under magnetic stirring at 50°C for 30 min. The solution was then transferred into the glass-lined autoclave and heated at 200 °C for 4 h, under continuous stirring. Then, the heater was removed, and the solution let thermalize at room temperature, before open the reactor.

Purification was performed by multiple washing and centrifugation cycles (10krpm, 10 min), aimed at removing the unreacted precursor. Specifically, acetone was added to a certain quantity of crude product in a volume ratio of 3:1. This cycle was repeated 2 times in total, adding acetone to recollect the precipitate. Then, the precipitate was washed using the same procedure but with a solution of 5% ethanol in hexane, followed by a centrifugation at 10krpm and finally recovering and drying the resulting pellet under vacuum.

2.1.8. Synthesis and surface functionalization of gold nanoparticles (AuNPs)

AuNPs employed in the study of plasmonic resonance energy transfer for CD red emission enhancement (Sec. 3.2) were synthesized via a method based on reduction of $HAuCl_4$ by sodium citrate [7]. Specifically, a sodium citrate aqueous

solution was quickly added to a HAuCl$_4$ aqueous solution previously heated up to 100°C. The system was allowed to react for 10 min and then the reaction was stopped by allowing the system to cool down to room temperature.

To promote the coupling with the negatively charged carboxyl groups of CDs, the surface charge of the AuNPs was modified by a post-synthetic treatment with a cationic ligand. This was accomplished by adding a carefully controlled amount of CTAB to the pristine AuNPs aqueous dispersion under vigorous magnetic stirring. As also reported in [8], this results in the formation of a compact bilayer of interdigitated CTAB molecules at the surface of the AuNPs.

2.2. Spectroscopic analysis

2.2.1. Fourier-Transform Infrared (FT-IR) spectroscopy

The surface chemical composition of synthesized CDs was characterized by FT-IR spectroscopy through a PerkinElmer Spectrum One Fourier Transform Infrared spectrophotometer (PerkinElmer, Inc., Waltham, MA, USA) with the attenuated total reflection technique was employed, using a 4-mm-diameter diamond microprism as an internal reflection element.

Approximately 5 µL of CD dispersions in a suitable solvent (water or ethanol) were drop-casted onto the surface of the microprism and the solvent was allowed to evaporate. Spectra were then acquired on as-formed dried CDs.

2.2.2. Dynamic Light Scattering (DLS) and ζ-potential

Hydrodynamic size of CDs and their surface ζ-potential was evaluated using a Zetasizer Nano ZS, Malvern Instruments Ltd., Worcestershire, UK (DTS 5.00). To ensure reproducibility of measurements, hydrodynamic size analysis and ζ-potential were repeated on three replicates. The mean hydrodynamic diameter and ζ-potential are then reported as mean values with the corresponding standard deviation.

2.2.3. UV-Vis absorption spectroscopy

UV-Vis spectroscopy was extensively used for the characterization of the absorption optical properties of all prepared materials. All UV–Vis absorption spectra reported in this thesis were recorded with a Cary 5000 spectrophotometer (Agilent Technologies, Inc., Santa Clara, CA, USA). This instrument is a double beam spectrophotometer equipped with a tungsten halogen visible lamp and deuterium arc UV lamp and allows detection of light absorbed by a sample in the ranges of UV, visible and near-infrared. Liquid solutions and nanoparticle dispersions were analyzed using quartz cuvettes with an optical path of 1 cm. Solid state nanocomposite films deposited on quartz substrate were examined in the spectrophotometer using an opportune sample holder allowing vertical mounting the sample with its surface perpendicular to the incident light beam.

2.2.4. Steady-state fluorescence measurements

Steady-state PL spectroscopy had a key role to characterize emission properties of synthesized CDs and to evaluate their performances in the solid-state polymeric nanocomposites. PL spectra were recorded using a Fluorolog 3 spectrofluorometer (HORIBA Jobin-Yvon). A schematic representation of the instrumental apparatus used for the PL analyses is shown in Figure 2.5.
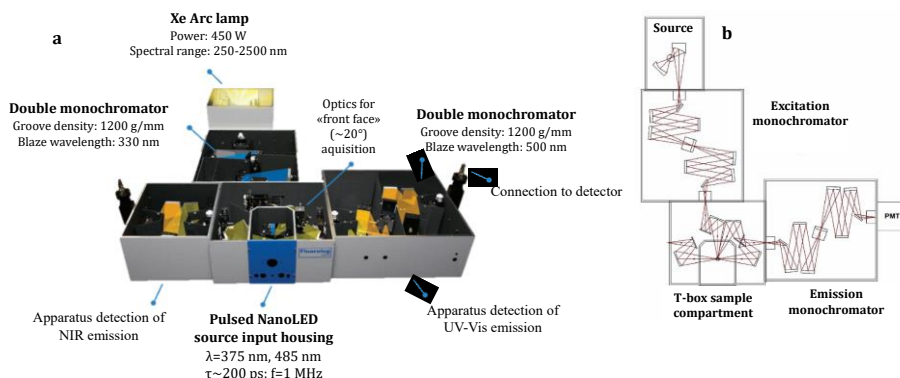
Figure 2.5: *(a) schematic overview of the Fluorolog 3 spectrofluorometer used for PL characterizations in this work, (b) schematic representation of the instrument components used for recording UV-Vis PL emission and excitation spectra. Adapted from [9].*

The instrument is equipped with a 450 W Xe lamp as excitation light source. The excitation monochromator is a double-grating monochromator with a groove density of 1200 g/mm, blazed at 330 nm. The sample is placed in a "T-box" sample compartment. The emitted radiation can be investigated with a NIR or UV/Vis module. In this work, all the spectra were recorded using the UV/Vis module consisting of a double-grating emission monochromator blazed at 500 nm (groove density of 1200 g/mm). The emitted intensity was detected by a picosecond photon counter (TBX ps Photon Detection Module, HORIBA Jobin-Yvon) for both steady state and time-resolved PL measurements (see Sec. 2.2.6), working in the spectral range from 350 nm to 760 nm. Monochromators and detector are controlled by a personal computer, interfaced with the manufacturer software FluorEssence™. To record the emission spectra, the wavelength selected by the excitation monochromator was fixed, and the wavelengths selected by the emission monochromator were scanned, vice versa, for the excitation spectra, the emission wavelength was fixed, and the excitation wavelengths were scanned. Emission and excitation spectra were recorded with variable bandpass (spectral interval that is isolated by the monochromator at each grating scan step) and an integration time (time interval over which photons are registered and averaged by the detector for each data point), adjusted according to specific needs of sample measurements, while the increment (spectral spacing between two consecutive investigated data point) was kept fixed at 1 nm.

2.2.5. Absolute photoluminescence quantum yield (PLQY) measurements

PLQY was measured using a "Quanta-phi" integration sphere (10 cm in diameter) coated with Spectralon® (reflectance ≥ 95% in the range 250-2500 nm). The accessory was mounted in the sample compartment of the spectrofluorometer.

The absolute PLQY was then measured using a protocol outlined by the manufacturer within the FluorEssence™ software.

2.2.6. Time-resolved photoluminescence (TR-PL) analysis

TR-PL measurements were performed by the time correlated single photon counting (TCSPC) technique. The main principles of this technique are schematically represented in Figure 2.6.
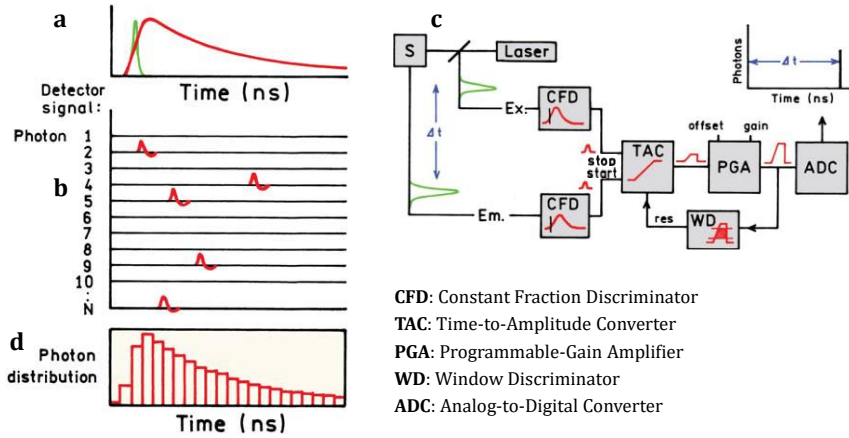
Figure 2.6: general principles of the data acquisition in the TCSPC technique, (a) laser source pulse signal (green line) and sample TR-PL decay signal (red line) as a function of time, (b) schematic representation of photons emitted by the sample for each excitation pulse, (c) schematic of electronics measuring the time delay between excitation pulse and emitted photons, (d) final output as histogram of detected photons as a function of the time delay. Adapted from [10].

The sample is excited by a pulsed laser source (NanoLED, λ =375 nm or λ = 485 nm, typical nominal pulse with ~200 ps at a maximum repetition rate (f) of 1 MHz), represented as the green curve in Figure 2.6a. This result in the formation of an initial population (n_0) of fluorophores in an excited energy state. After the source pulse, in the absence of further excitation, spontaneous decay occurs, i.e. the number of excited fluorophores spontaneously decreases as a function of time. In particular, the decay can be radiative (i.e. involving the emission of photons) or non-radiative (i.e. no photons are emitted in the decay). Considering a single population of fluorophores emitting by a simple fluorescence decay, the rate at which the number of fluorophores decreases can be considered proportional to the fluorophore number [10]:

$$\frac{dn(t)}{dt} = (k_r + k_{nr})\, n(t) \qquad (2.1)$$

Where $n(t)$ is the number of fluorophores at the time t after the excitation pulse, k_r is the emissive rate, and k_{nr} is the non-radiative decay rate. Integrating the equation yields:

$$n\,(t) = n_0 \exp(-\,t/\tau) \qquad\qquad (2.2)$$

Which is a mono-exponential decay function with:

$$\tau = (k_r + k_{nr})^{-1} \qquad\qquad (2.3)$$

τ represents the characteristic time of the exponential decay. As can be observed for (2.3), it depends on both the rates of radiative and non-radiative processes.

The PL instrument will detect photons with a certain energy defined by the emission monochromator. The number of detected photons at a certain delay time t is proportional to $n\,(t)$ and constitutes the detector signal intensity ($I(t)$). Hence: (2.2) can be rewritten as:

$$I(t) = I_0 \exp(-\,t/\tau) \qquad\qquad (2.4)$$

Where I_0 represents the number of photons detected at the time zero.

This registered decay function is represented by the red curve in Figure2.5a. The TCSPC measurements reconstructs this curve describing the spontaneous decay of initially excited fluorophores. This is achieved measuring the time delay between excitation and emission signals, accomplished by the specialized electronics shown in Figure 2.6c. In the final output, the overall investigated time window for the PL decay is divided in a certain number of channels, corresponding to increasing time delays between source pulse and detected photon. Thus, a histogram is constructed, reporting the detected number of photons as a function of each considered channel, representing the delay time (Figure 2.6d).

A TBX Photon Detection Module (HORIBA Jobin-Yvon) was used for emitted light revelation, with time resolution of 200ps, and electronic measurements performed using a FluoroHub (HORIBA Jobin-Yvon) station. Source, photon counter and monochromators were controlled by means of the manufacturer's software DAS6.

2.2.7. Fitting of TR-PL decays

From the output histogram (e.g. Figure 2.6d) of a TCSPC measurement, a decay function can be determined by fitting the experimental data. This allows examining quantitatively the decay dynamics of the sample fluorescence. Thus, this procedure requires assuming a decay model. In some simple cases, TR-PL

decays can be fitted using mono-exponential signal decay, such as that described in (2.4). However, in several system, the overall decay is more complex and cannot be interpreted with a single-exponential law.

In this thesis, complex decay TR-PL decays of CD emission bands were fitted using either multi-exponential models (DCDs, Sec. 3.1.2 and NR-CDs, Sec. 3.3.1), or a combination of a single-exponential and stretched exponential model (RCDs, Sec. 3.2.3). In general, the fitting function was considered to have a form of the type:

$$y(t) = f(t) \, IRF(t) \tag{2.5}$$

where $IRF(t)$ is the instrument response function (decay trace of the excitation laser passing through a scattering solution).

$f(t)$ was decided after trial-and-errors based on the analysis of the deviations between original data and obtained best-fitting model function, and thus varied according to the selected fitting model. For multi-exponential models, $f(t)$ was of the type:

$$f(t) = \sum_{i=0}^{n} A_i \exp\left(-\frac{t - t_0}{\tau_i}\right) \tag{2.2.6}$$

Where A_i are the amplitudes of the n exponential components, t_0 is the time at which the sample is excited and τ_i are the lifetimes of the two decay components.

In the case of combination of a single-exponential and stretched exponential model, $f(t)$ assumed a form of the type:

$$f(t) = A_1 \exp\left(-\frac{t - t_0}{\tau_1}\right) + B_1 \exp\left(-\frac{t - t_0}{\tau_2}\right)^{\beta} \tag{2.2.7}$$

where A_1 and B_1 are the amplitudes of respectively the mono-exponential and the stretched exponential decay and β is a stretching factor.

2.3. Photobleaching experiments

Characterizing the resistance of CDs to photodegradation is a key aspect to clarify their practical potential in several application fields [11,12]. Herein, particular effort was devoted to examining CDs photobleaching (PB), by studying variations of their optical responses after irradiation with powerful UV sources. This issue was addressed using two types of experimental configurations, using either a setup in which CDs were subjected to continuous UV irradiation or specific PB experiments that used pulsed laser sources.

2.3.1. Photobleaching experiments with continuous UV irradiation lamp

Within this experimental configuration, schematically depicted in Figure 2.7, dispersions of CDs in water or ethanol were placed in quartz cuvettes and exposed to a medium pressure Hg lamp (200 W, λ > 250 nm, irradiance 0.07 W/cm^2). The dispersions were kept under continuous magnetic stirring for the whole irradiation time. The irradiation light beam was perpendicular to the cuvette face with a section able to cover the entire volume of CD dispersion. Periodically, the cuvettes were transferred to the UV–Vis spectrophotometer or spectrofluorometer for spectroscopic monitoring of optical property alterations.

UV lamp
(200 W, λ > 250 nm, 0.07 W/cm²)

Dispersion of CDs
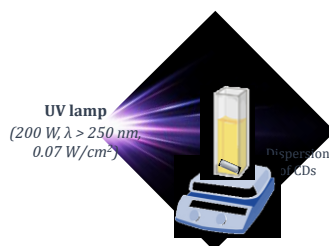
Figure 2.7: *schematic description of the PB experimental setup using continuous irradiation UV lamp.*

2.3.2. Photobleaching with pulsed laser sources

PB resistance of CDs was examined using specific spectroscopic techniques, based on the use of pulsed laser sources to simultaneously cause the bleaching of the samples and probing the changes of their optical properties. These studies were carried out in the laboratories of Prof. F. Messina at University of Palermo. Figure 2.8 schematically described the various employed techniques.
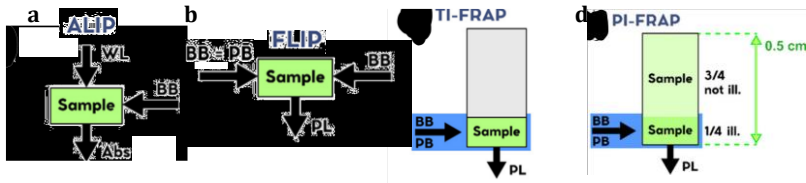
Figure 2.8: *schematic description of laser-induced PB experiments.*

The working principles of the techniques can be described as follows:

Absorption Loss in Photobleaching (ALIP): a pulsed laser beam is used to bleach the nanoparticle dispersion sample, while a continuous white light beam (WL) is used to probe absorbance (Abs).

Fluorescence Loss in Photobleaching (FLIP): the experiment can be performed using either distinct or coincident bleach laser beam (BB) and probe laser beam (PB); the PL is measured as observable variable after each BB for excitation with the PB.

Fluorescence Recovery After Photobleaching (FRAP): the experiments can be carried out in total illumination (TI) or partial illumination (PI), the geometry is similar to FLIP, but the FRAP experiments are conducted by first administering a bleaching stage in the same conditions for all the samples, and then monitoring the PL as a function of recovery time.

For all the experiments, the bleaching pulse energy was always fixed to 1.0 mJ, with a beam diameter of 1 mm, corresponding to about 130 mJ/cm^2 fluence per pulse. BB and PB wavelengths, as well as recorded spectral intervals of absorption and emission spectra were regulated according to the investigated sample and specific experimental aims. A complete list of all employed wavelengths, as well as further technical details regarding laser sources and other equipment used for these experiments are provided in [13].

2.4. Electron microscopy examinations

2.4.1. Transmission electron microscopy (TEM)

TEM was employed to study the size, the size dispersion and the morphology of the synthesized nanoparticles. This technique was selected since it allows direct imaging of the nanoparticles with sub-nanometer resolution [14,15]. The main components of a TEM microscope are depicted in Figure 2.9a and can be divided in (i) electron source, (ii) electrostatic lenses, and (iii) detection system.
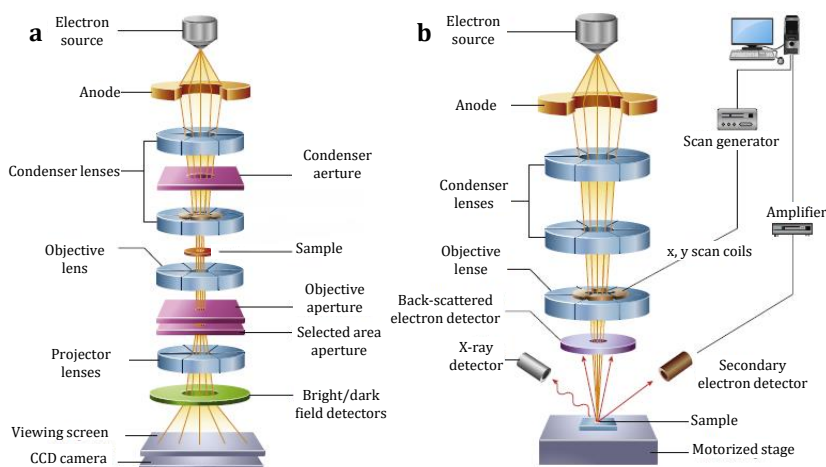
Figure 2.9: *schematic diagram of main components of a (a) TEM and (b) SEM microscope. Adapted from [14].*

The electron gun typically accelerates electrons at an accelerating voltage ranging between 80 and 300 kV [14]. As it is well-known from de Broglie relationship, the electron energy is inversely proportional to its wavelength [15]. Therefore, higher energies are able to provide better image resolution [16]. However, for carbonaceous materials, such as CDs, it is often preferable not to operate at very high voltages, in order to prevent material damaging during electron beam irradiation [16].

In this work, TEM analysis of DCDs (Sec. 3.1.2) and AuNPs (Sec. 4.2) was carried out using a JEOL JEM-1011 microscope (JEOL, Akishima, Tokyo, Japan), equipped with a W filament operating at 100 kV, at the Electron Microscopy Lab of CNR-IPCF Bari. Higher resolution TEM investigation of RCDs (Sec. 3.2.3) and NR-CDs (Sec. 3.3.2) were performed at Centro Servizi d'Ateneo per la Ricerca (CeSAR) of University of Cagliari, using a JEOL JEM-1400 microscope. This microscope was equipped with a W filament operating at 120 kV. In both microscopes, micrographs

were acquired using an Olympus Quemesa high resolution charged coupled device (CCD) camera.

The samples were prepared by dipping carbon coated copper grids in opportunely diluted ethanol solutions of CDs and then leaving the grids to dry in air. The concentration of nanoparticles in the solution was suitably controlled to provide a sufficient number of nanoparticles in the analyzed sample, while concurrently avoiding nanoparticle aggregation, possibly occurring during solvent evaporation if the nanoparticle concentration is too high. This is crucial to attain an accurate statistical analysis of nanoparticle size dispersion [17–19]. After preparation, the TEM samples were mounted in the microscope holder, that allows translation in the (x, y, z) directions and tilting (by typically ±20° to 40°). These movements are necessary for control the beam focusing and exploring different specimen areas with different magnifications [15]. Finally, the transmitted beam can be examined either on a phosphor screen, or using the CCD camera (Figure 2.9a) [14].

The statistical analysis on CD size was performed by using ImageJ (v.1.52a) free image analysis software. Mean size (μ) and standard deviation (s) were calculated assuming a Gaussian sizes distribution. Percent standard deviation (σ) was calculated as:

$$\sigma = \frac{s}{\mu} \times 100 \qquad (2.8)$$

2.4.2. Scanning electron microscopy (SEM)

SEM was employed for the characterization of the surface of polymeric CD nanocomposite films and for the measurement of their thickness (Sec. 5.1.2). A scheme of a SEM microscope is reported in Figure 2.9b. In SEM, as opposed to TEM, the sample is placed at the base of the electron column, and a specific arrangement of coils is employed to scan the electron beam in a raster-like pattern, to examine the sample surface [14,15]. Detectors are located in the region above the sample and collect secondary and/or backscattered electrons [14,15].

In this work, SEM micrographs were acquired using a Zeiss Sigma microscope (Carl Zeiss Co., Oberkochen, Germany) at the Electron Microscopy Lab of CNR-IPCF Bari, operating in the range 0.5–20 kV and equipped with an in lens secondary electron detector.

The sample was mounted using double-sided carbon tape onto suitable Al stubs (for surface examination) or appropriate sample holders allowing vertical mounting (for cross-section analysis). Secondary electrons were detected using the specific microscope electron detector.

References

[1] M. Moniruzzaman, J. Kim, Nanoscale 15 (2023) 13858–13885.

[2] Y. Huo, S. Xiu, L.-Y. Meng, B. Quan, Chemical Engineering Journal 451 (2023) 138572.

[3] Y. Cheng, G. Yu, Molecules 28 (2023) 7473.

[4] M. Otten, M. Hildebrandt, R. Kühnemuth, M. Karg, Langmuir 38 (2022) 6148–6157.

[5] J.B. Essner, J.A. Kist, L. Polo-Parada, G.A. Baker, Chem. Mater. 30 (2018) 1878–1887.

[6] B. Bartolomei, A. Bogo, F. Amato, G. Ragazzon, M. Prato, Angewandte Chemie International Edition 61 (2022) e202200038.

[7] M. Wuithschick, A. Birnbaum, S. Witte, M. Sztucki, U. Vainio, N. Pinna, K. Rademann, F. Emmerling, R. Kraehnert, J. Polte, ACS Nano 9 (2015) 7052–7071.

[8] J. Lim, N.-E. Lee, E. Lee, S. Yoon, Bulletin of the Korean Chemical Society 35 (2014) 2567–2569.

[9] HORIBA Jobin-Yvon, Fluorolog-3 Operation Manual rev. G (2 May 2014), (n.d.).

[10] J.R. Lakowicz, Principles of Fluorescence Spectroscopy, 3rd ed., Springer US, 2006.

[11] Y.-Y. Liu, N.-Y. Yu, W.-D. Fang, Q.-G. Tan, R. Ji, L.-Y. Yang, S. Wei, X.-W. Zhang, A.-J. Miao, Nature Communications 12 (2021) 1–12.

[12] A. Sciortino, A. Cannizzo, F. Messina, C 4 (2018) 67.

[13] A. Terracina, A. Armano, M. Meloni, A. Panniello, G. Minervini, A. Madonia, M. Cannas, M. Striccoli, L. Malfatti, F. Messina, ACS Appl. Mater. Interfaces 14 (2022) 36038–36051.

[14] B.J. Inkson, in: Materials Characterization Using Nondestructive Evaluation (NDE) Methods, Elsevier, 2016, pp. 17–43.

[15] D.B. Williams, C.B. Carter, Transmission Electron Microscopy: A Textbook for Materials Science, 2. ed, Springer, New York, 2009.

[16] Z. l. Wang, Advanced Materials 15 (2003) 1497–1514.

[17] J. Ayache, L. Beaunier, J. Boumendil, G. Ehret, D. Laub, C.-U. Villejuif, (n.d.).

[18] W.K. Haller, (2009).

[19] M.M. Błaszczyk, Ł. Przybysz, Appl Nanosci 12 (2022) 119–128.

3

Synthesis and Characterization of Carbon Dots

"The best scientists and explorers have the attributes of kids. They ask question and have a sense of wonder. They have curiosity. 'Who, what, where, why, when, and how!' They never stop asking questions, and I never stop asking questions, just like a five year old."

Sylvia Earle

Abstract

Current research on CD preparation shows promise in producing luminescent nanoparticles with disparate optical properties, across the whole visible range. However, challenges still exist, particularly in controlling CD optical features through precise selection of carbonaceous precursors and synthetic protocols. Herein, various synthetic strategies are explored, ranging from solvothermal synthesis to controlled multi-step condensation of an aromatic precursor, to obtain *a priori* designed fluorescence features. Specific emphasis is placed on addressing gaps in reported methods for CDs with red emission. The chapter also explores the advanced characterization of CDs, the photobleaching resistance (pivotal feature for CD applicative use) and the enhanced red emission through interaction with plasmonic nanoparticles. Overall, these studies outline novel mechanistic insights, advancements of CD synthetic protocols and achievement of CDs with efficient, stable, and customizable optical properties. This chapter references published works: G. Minervini et al., Nanomaterials (2023) [1]; G. Minervini et al., Carbon (2022) [2]; G. Minervini et al., ACS Nano (2023) [3].

3.1. CDs by solvothermal carbonization of citric acid and urea with in-situ surface passivation (DCDs)

Bottom-up solution synthesis of CDs consists in controlled carbonization of carbonaceous precursors. During the reaction, photoluminescent carbon nanoparticles arise thanks to chemical reactions of thermal degradation, dehydration and polycondensations of the precursor organic molecules [4–6]. This process leads to the formation of compact spheroidal carbonaceous nanoparticles, eventually containing aromatic structures or molecular fluorophores with optical emission in the visible range.

In sealed autoclave reactors, solvothermal conditions facilitates the attainment of reaction temperatures and pressures necessary for the carbonization of the organic molecules employed as precursors. Moreover, in most cases carbonization is obtained regardless of the exact chemical structure and composition of such organic molecules. Therefore, solvothermal routes open the possibility of synthesizing CDs from a broad variety of small organic precursors. Additionally, these methods generally offer higher throughput syntheses, lower costs, and great environmental friendliness, especially compared to *top-down* approaches. As a consequence, solvothermal techniques are presently among the most widely adopted *bottom-up* strategies for CD synthesis [7–9].

Particularly interesting for the scopes of this work is that, within such solvothermal strategies, adjustment of reaction variables (e.g. temperature, pressure, solvent type, mixture of carbonaceous precursors [7,10–12]) may be used to alter the mechanisms of formation of aromatic structures or molecular fluorophores responsible for the optical properties of the obtained nanoparticles [10,13,14,14]. Ultimately, this could lead to deliberately design the optical emission of the CDs with intentional control.

Besides the control of reaction variables, an additional extensively documented approach to optimize the emission characteristics of solvothermally synthesized CDs is introducing a polymer passivating agent to modify their surface [15,16]. This surface passivation can be generally attained either *in-situ* (i.e. adding the polymer to the mixture of carbonaceous precursors) or *ex-situ* (i.e. in a post-synthetic surface modification). The polymer-passivating layer surrounding CD surface has been shown to confer a dual advantage: (i) enhancing emission efficiency, especially in the longer wavelength region of the visible, and (ii) improving the chemical and colloidal stability of the nanoparticles in different environments and/or solid matrices [17–19]. Nonetheless, most of reported polymer-passivated CDs still have an intense emission only in the blue-green

region, while PL components at longer wavelengths (i.e. orange-red region) often still exhibit low intensity, and PLQY frequently below 10% [20–25].

In the next section, a solvothermal synthesis of CDs is reported employing a branched PEI as surface passivating agent. The synthesis uses CA and urea as primary carbonaceous precursors and DMF as solvent. The obtained DCDs exhibit a highly enhanced red component thanks to the surface polymer passivation, reaching a PLQY of around 20% in the red spectral region. Overall, the DCDs are characterized by a double emission component, in the green and in the red, with nearly equal intensity. This spectroscopic characteristic, combined with the stability and resistance to aggregation-induced quenching (both attained thanks to the successful polymer passivation), will be leveraged for the fabrication of white color-converting nanocomposites (Sec. 5.1).

3.1.1. Synthesis and purification of DCDs

The synthesis of DCDs was based on an already reported solvothermal CD synthesis, involving the carbonization of CA and urea dissolved in DMF [26,27]. To enable the polymer passivation, PEI (branched, $M_w \sim 2000$ Da) was added in 0.02 mM concentration to the precursor reaction solution, then subjected to the solvothermal carbonization within an autoclave reactor (experimental details are provided in Sec. 2.1.2 and Sec. 2.1.5).

After the synthesis, residual unreacted precursors as well as any fluorescent byproduct were removed by a devised centrifugation procedure. This procedure takes advantage of the tunability of the charge of the surface groups of the DCDs as a function of surrounding medium pH. In fact, similarly to other solvothermally synthesized CDs, the surface composition of the DCDs encompasses a variety of chemical groups, including carboxylic and amino functionalities (see Figure 3.1c for reference). The charge states of these groups are susceptible to alterations according to the environmental pH conditions, possibly giving rise to nanoparticle surface charge neutrality, or conferring to the CDs a neat negative or positive surface charge [28,29].

Hence, pH serves as a convenient tool for modifying the surface charge of the CDs, thereby modulating the electrostatic repulsion between the nanoparticles and thus, their colloidal stability. In this specific case, the DCDs remain stably dispersed in basic environments. On the other hand, addition of a diluted aqueous acidic solution of HCl (HCl$_{aq}$) to DCDs dispersion, provides a colloidal destabilization. Therefore, in a purification procedure consisting of multiple centrifugation steps, HCl$_{aq}$ was used as nonsolvent to precipitate the nanoparticles upon centrifugation (see Sec. 2.1.5 for experimental details). At each step, residual molecular components (e.g., unreacted precursors and eventually other

byproducts) were dissolved in the supernatant and thus eliminated from the purified carbon nanoparticles forming the solid precipitate.

This undesired component removal was easily monitored by recording UV-Vis absorption spectra of the supernatants to follow the washing/centrifugation cycles necessary to the complete purification of DCDs (Figure 2.3, Sec. 2.1.5). The recorded spectra display a progressive dampening of the absorption band centered at around 350 nm, ascribed to molecular byproducts that are not bound to the nanoparticles. Thus, the spectroscopic monitoring allows to confirm the effectiveness of the purification strategy that succeed to both dissolve molecular byproducts and eliminate these undesired molecules from the purified DCDs.

3.1.2. Characterization of DCDs and investigation of red emission enhancement

After purification, the obtained DCDs were characterized in terms of size, shape, chemical composition, and optical properties (Figure 3.1).
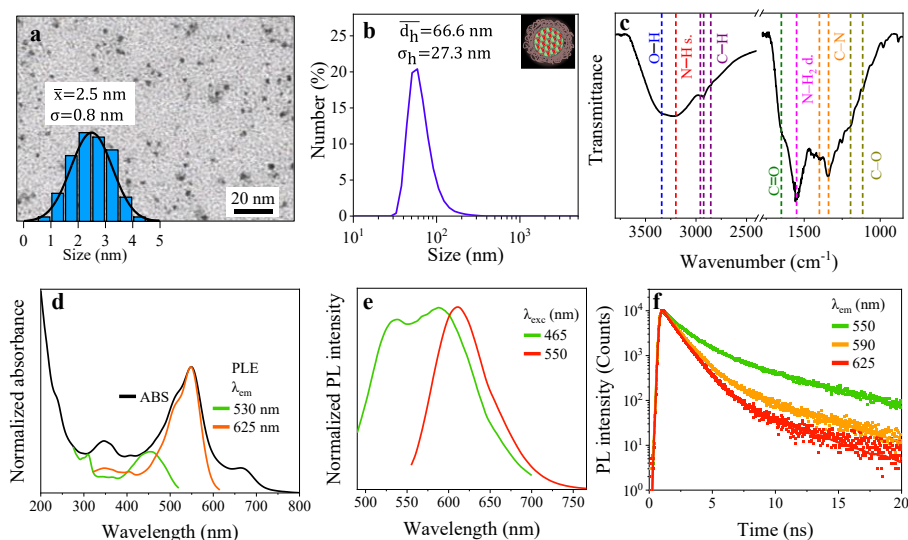
Figure 3.1: *(a) TEM micrograph of DCDs and relative size distribution (inset) indicating the nanoparticle average size ($\bar{x}$) and standard deviation (σ); (b) DLS size distributions of DCDs, with obtained average hydrodynamic diameter ($\bar{d}_h$) and standard deviation (σ_h); (c) FT-IR spectra of DCDs, where the identified main peaks are labelled; (d) UV-Vis absorption and PLE spectra (λ_{em} = 530 nm, 625 nm); (e) normalized PL spectra (λ_{exc} = 465 nm, 550 nm); (f) TR-PL decay profile (λ_{exc} = 485 nm, λ_{em} = 550 nm, 590 nm and 625 nm) [1].*

TEM analysis (Figure 3.1a) shows spheroidal nanoparticles with mean size of 2.5 ±0.8 nm. Interestingly, DLS analysis of the DCDs dispersed in water (Figure 3.1b) reveals a mean hydrodynamic diameter of 66.6 nm (σ =27.3 nm). It

is worth noticing that the evaluated DLS mean size refers to hydrodynamic diameter of nanoparticles in solution, which is larger than the average dimensions measured by TEM. Moreover, due to PEI passivating polymer layer presence on the DCD surface, more CDs can be grouped together by the same polymer layer. Then, the steric hindrance of these PEI structures are expected to produce a high increase of the hydrodynamic size probed by DLS.

To gain more information on the chemical composition of the DCD surface, a FT-IR analysis was performed. The recorded FT-IR spectrum of the DCDs (Figure 3.1c) displays a very feature-rich surface; specifically, O–H stretching (broad band at 3340 cm^{-1}), N–H stretching (band at 3200 cm^{-1}), C–H stretching (triplet at 2960, 2925 and 2850 cm^{-1}), C=O stretching (peak at 1650 cm^{-1}), N–H$_2$ deformation (band at 1550 cm^{-1}), C–N stretching (peaks at 1400 and 1340 cm^{-1}) and a region densely populated of peaks below 1300 cm^{-1} can be observed. This indicates that the DCD surface is composed of a variety of chemical groups, including hydroxyl, carboxylic, amino, and amidic groups, where the amino groups are reasonably belonging, at least partly, to the surface PEI chains.

UV-Vis absorption spectrum of the DCDs displays an intense band in the visible, peaked at 550 nm, with a secondary shoulder at 520 nm; while another absorption band is observable peaked at longer wavelengths (around 650 nm). The absorption spectrum at λ<500 nm exhibits a more complex profile, likely attributable to multiple spectral overlapping components. In fact, an optically active excitation band, peaked at around 450 nm, is revealed by the PLE spectrum at λ$_{em}$=530 nm. Moreover, another absorption peak is found at around 350 nm. According to several previous reports, this is ascribable to n–π* transitions occurring in surface chemical groups of the DCDs. On the other hand, the extended absorption band at λ<300 nm can be attributed to π-π* transitions of conjugated carbonaceous features within the carbogenic core of the DCDs [6,30,31].

Overall, the PL spectrum of the DCDs excited at 465 nm, consists of a green PL band at 530 nm and of a red emission band centered at 610 nm, correspondent to the PLE band at 450, and to absorption and excitation band at 550 nm, respectively. Excitation of both green and red PL bands is expected to occur in a range of λ$_{exc}$ in the blue (e.g. around 450-500 nm). The excitation wavelength was purposely selected at 465 nm because it coincides with the peak wavelength of the LED chip used in color-conversion experiments (Sec. 5.1). The presence of the two spectrally overlapping green and red PL bands is also reflected in the TR-PL decays, recorded at increasing λ$_{em}$ of 550, 590 and 652 nm (Figure 3.1f). All these decays were best-fitted by a bi-exponential model function (Sec. 2.2.6). and exhibit a progressive decrease of the lifetimes with increasing λ$_{em}$. Both such features commonly describe the TR-PL behavior of numerous solvothermally synthesized

CDs with multiple emission bands in the visible range and are attributed to the heterogeneous nature of spectral emissive components [4,5,11].

On the other hand, exciting with a green radiation (e.g. at 550 nm), allows for selectively revealing only the red emission. The overall spectroscopic properties obtained for both λ_{exc} in the blue and in the green region can be schematically summarized as reported in Figure 3.2.
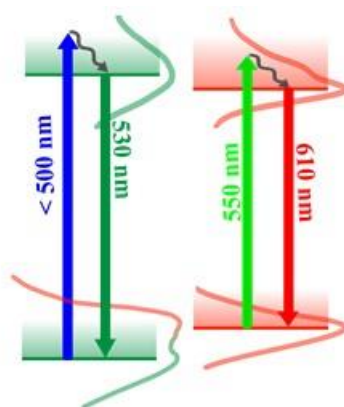
Figure 3.2: diagram of the hypothesized optical transitions responsible for the observed PL emission bands of DCDs; the colored curves represent the PL (bottom) and PLE (top) spectra correspondent to the reported λ_{exc} and λ_{em} [1].

The high intensity of the red PL band is a remarkable characteristic of the DCDs. In fact, most of CDs synthesized through solvothermal carbonization of CA and amines only displays a weak emissive component in the red region [32–34]. For this reason, a control experiment was performed exactly in the same experimental synthetic conditions except for the absence of PEI in the reaction solution. Compared to the DCDs, the resulting non-passivated DCDs (np-DCDs) show a markedly less intense emission in the red region (Figure 3.3). Consequently, also the PLQY of np-DCDs (at λ_{exc} of both 465 nm and of 550 nm) is markedly reduced compared to that of DCDs, which reaches a maximum value of 18±2%. (Table 3.1).
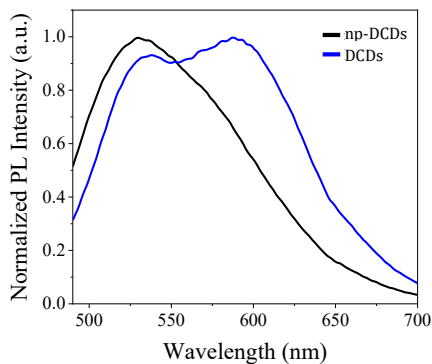
Figure 3.3: *normalized PL spectra (λ$_{exc}$ = 465 nm) of np-DCDs and DCDs.*

The control experiment indicates that the observed red band enhancement is clearly correlated with the introduction of PEI in the reaction mixture. Therefore, we can conclude that the introduction of PEI as *in-situ* passivating agent can be a valuable strategy to enhance the intensity and PLQY of CD emission in the red spectral region, especially in solvothermal syntheses of CDs that use CA and urea as precursors.

Table 3.1: *PLQY at λ$_{exc}$ of 465 and 550 nm measured for the DCDs and np-DCDs in the control experiment.*

Sample	PLQY %(λ$_{exc}$ = 465nm)	PLQY %(λ$_{exc}$ = 550nm)
DCDs	9±4	18±2
np-DCDs (control)	4±2	8.4±1.1

3.2. CDs from glycothermal treatment of resorcinol (RCDs)

As discussed in Sec. 3.1, solvothermal routes offer some notable advantages as *bottom-up* synthetic approaches for CDs. One of the primary goals of ongoing studies on these synthetic strategies consists in achieving the production of CDs with deliberately controlled optical properties, designed through the adjustment of reaction conditions. However, this task is remarkably hindered by difficulties in understanding how the reaction parameters influence the complex carbonization processes governing nanoparticle formation [7,9,28]. In fact, this lack of knowledge implies that relationships between synthetic parameters and CD properties have to be mostly examined empirically, case-by-case, with a trial-and-error approach [11,12,34–36]. On the other hand, for a real rational control of the CD optical response it is crucial to (i) identify the actual origin of the CD fluorescence, including any molecular fluorophores participating in the emission mechanism, (ii) understand their role in the overall CD fluorescence and PL mechanisms [5,7,9,11].

The challenges in achieving such profound insights may also be partly attributed to the organic molecules employed as carbonaceous precursors and to the complex chemical reactions involved in their carbonization [7,9–11,28]. It is widely accepted that in CDs, optical absorption and emission in the visible range arise from the formation of polyconjugate aromatic structures or aromatic molecular dyes (Sec. 1.2) [4,5,11]. However, most frequently used organic molecules do not originally contain aromatic rings in their chemical structure. On the contrary, fluorescent aromatic compounds or large polyconjugate structures have to form during the carbonization process, upon supplying thermal energy. Yet, detailed chemical mechanism underlying these processes may be sometimes challenging to elucidate completely, [37,38] making also the experimental control more difficult.

Moreover, existing challenges in such *bottom-up* CD syntheses also include difficulties in reproducibility and standardization of synthetic protocols. In fact, it is often reported that various batches of CDs prepared in different laboratories exhibit differences in size, surface functional groups, and optical properties, despite using similar precursor ratios, synthetic setups, and reaction conditions (temperature, time). In the first instance, also this inconsistency can be clearly related to the sensitivity of complex carbonization processes to these variables. Nonetheless, additional challenges are also provided by the fact that most reactors used in CD synthesis lack the capability to monitor internal conditions, such as the reaction temperature or eventual increments of pressure due to formation of volatile compounds. Addressing these issues requires the development of

protocols allowing a careful control of synthetic conditions and a deeper understanding of the synthesis process to enhance the reliability and consistency in CD preparations.

Here, the synthesis of CDs from a hydroxyl-substituted phenol was explored, with the explicit purpose of monitoring the formation of fluorescent polycyclic aromatic structures in a controlled reaction environment. According on the theoretical finding of Yang et al. [39], resorcinol was selected as carbon precursor, being characterized by a lower activation energy barrier for multiple concomitant condensations, with respect to other similar precursors, such as phloroglucinol.

The resorcinol polycondensation mechanisms were investigated, also supported by Density Functional Theory (DFT) calculations, together with the possibility of altering the reaction kinetics by adding either a basic (NaOH) or an acidic (H_2SO_4) catalyst. The obtained CDs were then deeply characterized, especially from the perspective of interesting properties, such as PB resistance and pH-dependency of fluorescence.

Examination of pH-induced alterations of CD emission spectral features allowed for a detailed individuation of the acid-base equilibria involving the molecular fluorophores responsible for CD optical properties. This further opened the possibility of applying titrimetric techniques to estimate the CD concentration in an aqueous dispersion, a measurement that holds pivotal importance across several various applications. Finally, the in-depth investigation further inspired the application of these RCDs in nitrocellulose-based sensing devices, as described in Chapter 5.

3.2.1. Synthesis of RCDs without catalysts and formation of fluorescent PAHs

RCDs were firstly synthesized *via* direct thermal polycondensation of resorcinol, without using any added catalysts, and for this reason the produced nanoparticles are denoted as "n-RCDs" in the following. The reaction was conducted in EG as reaction solvent, in an open round bottom flask (see Sec. 2.1.3 and Sec. 2.1.6 for further experimental details). Thanks to the easy accessibility of the open reactor with respect to sealed autoclave vessels, the formation of fluorescent polycyclic aromatic molecules from multi-step condensations of resorcinol was studied by real-time monitoring spectroscopic properties of the reaction batch during the reaction proceedings. In the first instance, the formation of such OH-substituted polycyclic aromatic hydrocarbons (OH-PAHs) with optical transitions in the visible can be deduced from a visual inspection of the reaction solution color over time (Figure 3.4a). The reaction solution is in fact observed to gradually shift from colorless to orange/red. Since resorcinol exhibits absorption only in the UV and not in the visible (Figure 2.4, Sec.2.1.6), the modification in solution color serves

as initial confirmation that species with optical absorption in the visible region are progressively developing.
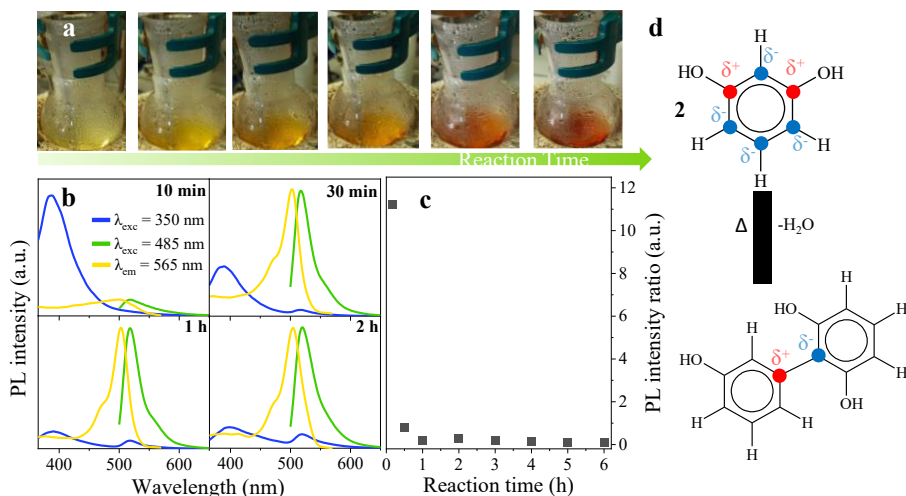
Figure 3.4: *(a) pictures of the reaction vessel during the synthesis of n-RCDs, recorded (from left to right) at reaction times of 10, 30, 45, 60, 180 and 300 min (b) PL spectra (λ_{exc} of 350 nm and 485 nm) and PLE spectra (λ_{em} = 565 nm), recorded during the synthesis at reaction times of 10 min, 30 min, 1 h and 2 h (c) ratio between the intensity of the PL band at 400 nm (λ_{exc} = 350 nm) and at 520 nm (λ_{exc} = 485 nm) as a function of reaction time; (d) schematic description of thermally-activated condensation between resorcinol molecules [2].*

Figure 3.4b shows the PLE and PL spectra of the raw reaction batch, recorded at increasing reaction time from 10 min to 2 h. For λ_{exc} = 350 nm (blue curves), the PL spectra exhibit two bands centered at 400 nm and 520 nm. On the other hand, λ_{exc} = 485 nm allows the exclusive excitation of the PL band at 520 nm, characterized by a narrow and well-defined line shape. The PLE spectra (λ_{em} = 565 nm) reveal narrow band profiles that closely mirror the emission band at 520 nm.

We can very reasonably associate these PL bands to fluorescent OH-PAHs resulting from resorcinol polycondensations in the ongoing reaction. More precisely, we can safely assume that such PAHs arise from thermally activated condensation of resorcinol molecules, as depicted in Figure 3.4d. Furthermore, the PL spectroscopic observations suggest that since the first steps of the reaction, the multi-step condensations lead to various PAHs with different chemical structures, rather than a single type of OH-PAH. In fact, the narrow spectral features of the fluorescence band emitting in the green region recall typical fluorescence of a single emitting species [40] and can be hence attributed to a single polyaromatic

fluorophore. Nonetheless, the presence of the broad and asymmetric blue PL component implies the involvement of multiple emitting species overall contributing to such emission signal.

The ratio of PL intensities of the two emission bands as a function of reaction time (Figure 3.4c) further reveals that the intensity of the blue band, very high within the first hour of the reaction, is strongly reduced at longer reaction times. This can be easily explained considering that some of the blue emitting species formed in the early stages of the reaction are consumed or modified within the first hour.

This can be interpreted as follows: in the first steps of reaction, resorcinol condensations give rise to PAHs with different structures: one OH-PAH is responsible for the observed emission in the green, while other OH-PAHs are responsible for the blue PL component. In particular, the blue luminescent species may be small molecules composed of 3-4 benzene rings; this being corroborated by several previous reports demonstrating the manifestation of blue fluorescence of such small polycyclic compounds [41–45]. The drop of blue PL intensity in the first hour of the reaction can be explained with a part of such small OH-PAHs being progressively consumed to favor the formation of larger OH-PAHs characterized by emission at longer wavelengths.

3.2.2. *Modelling of OH-PAH chemical structure and spectroscopic properties*

The spectroscopic monitoring of the reaction enables to infer the formation of luminescent PAHs from resorcinol condensations, having emission both in the blue and in the green. However, determining the exact chemical structures of these polycyclic molecules is still challenging. This mainly stems from the fact that different benzenoid ring arrangements can give rise to PAHs with relatively similar optical properties [42,45,46]. Thus, to better assess possible chemical formulas of these species, a density functional theory (DFT) theoretical investigation was performed, in collaboration with Prof. Carbonaro at University of Cagliari. This work involved simulating possible OH-PAHs forming during the synthetic process and calculating their optical transitions in the UV-Vis range (details on computational methods are provided in [2]). Then, by comparing the calculated optical transitions with the experimental optical data, more insights into the structural characteristics of the photoactive species were inferred.

Several different OH-PAH chemical structures were considered, varying number and arrangement of aromatic rings and substituting –OH groups and taking in consideration how resorcinol molecules may assemble via condensation (Figure 3.5).
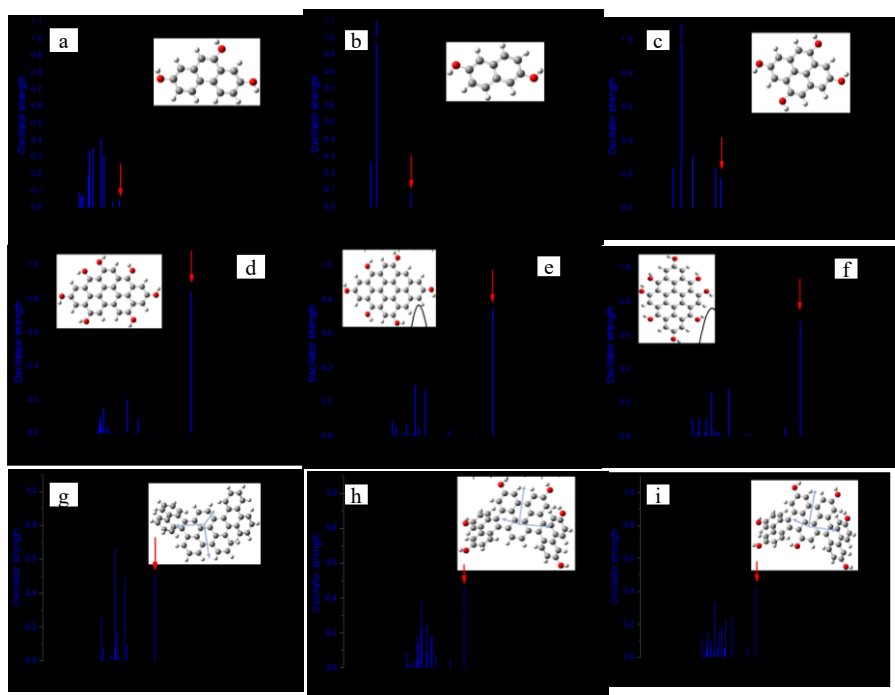
Figure 3.5: representative examples of calculated oscillator strengths and absorption spectra of OH-PAHs with (a-c) 2-4, (d-f) 8-9, (g-i) 9-11 fused benzenoid rings. The insets report the representation of each structure (C atom = grey sphere, H atom = white sphere, O atom = red sphere) [2].

As a general trend, a red shift of the transition at longer wavelengths, corresponding to the gap between highest unoccupied and lowest occupied molecular orbital (HOMO-LUMO gap) was observed for planar structures up to 9 fused rings. This is in agreement with the well-known decrease in energy of the main optical transitions with increasing conjugation in polyaromatic structures [42,46]. When considering a higher number of fused rings, most OH-PAHs exhibit non-planar, distorted tridimensional structures, as shown in Figure 3.5g-i. Such distorted molecules show a blue shifted HOMO-LUMO gap. However, OH-PAHs with comparable number of fused rings display optical transition dependent on the arrangement of benzenoid rings and –OH groups in the structure. Therefore, these molecular parameters exhibit an intimate relationship with the electronic configuration of the molecules.

These results are valuable for the correlation between optical properties and molecular structure of the OH-PAHs. In particular, the red-shift of the HOMO-LUMO gap observed in the simulated structures corroborates the hypothesis that the green emitting fluorophore is formed after condensation of smaller OH-PAHs,

possibly also exhibiting blue emission. On the other hand, according to the DFT simulation, the experimental observation that the HOMO-LUMO gap does not further shift from the green to the red at increasing reaction time can be tentatively explained with the possible interruption of extended conjugation in the OH-PAH (i.e. formation of distorted OH-PAHs) when structures with a higher number of fused rings are formed with increasing reaction time.

3.2.3. Morphological, structural, and optical properties of n-RCDs

After the synthesis, n-RCD nanoparticles can be isolated after a purification process, based on washing and centrifugation steps with a diluted ($\sim 10^{-4}$ M) aqueous HCl solution (further technical details are provided in Sec. 2.1.6). The effectiveness of such purification procedure in separating the RCDs from small molecular species present in the raw reaction batch can be confirmed by a UV-Vis absorption monitoring of the purified nanoparticles at each purification step. As shown in Figure 2.4 (Sec.2.1.6), the absorption spectra show a significative reduction of the resorcinol band at 276 nm after each precipitation and redispersion cycle, testifying its effective removal from the nanoparticle precipitate. Therefore, molecular byproducts that are freely dissolved in solution and not linked to the nanoparticles were quantitatively removed by the multiple steps of purification. The morphological, structural, chemical, and optical characterization of purified n-RCDs led to the results summarized in Figure 3.6.
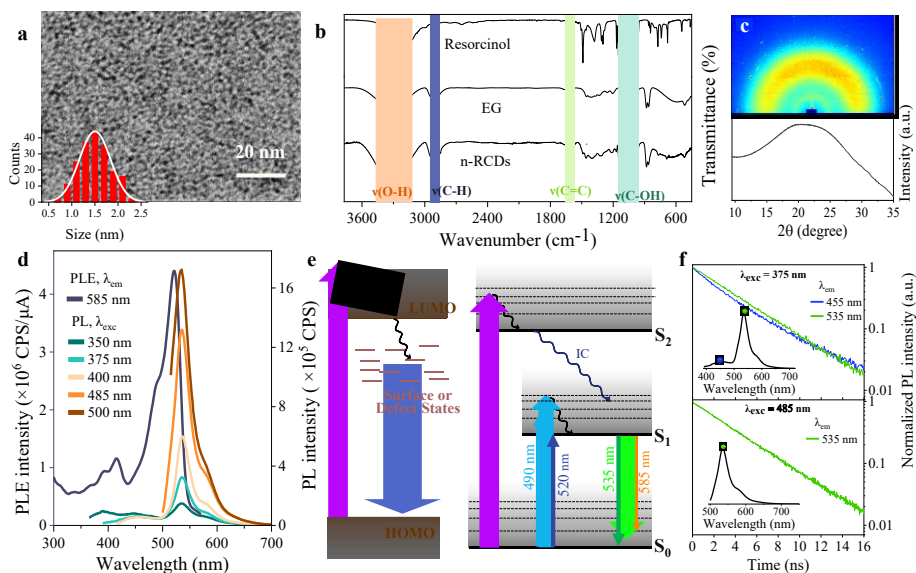
Figure 3.6: (a) TEM micrograph and size distribution histogram (inset) of the purified n-RCDs; (b) FT-IR spectrum of the n-RCDs compared with the spectra of resorcinol and EG; (c) GIWAXS 2D (top) and 1D (bottom) pattern of n-RCDs; (d) PL

excitation (λ_{em} = 585 nm, black line) and emission spectra at different excitation wavelengths of purified n-RCDs dispersed in ethanol; (e) schematic description of the hypothesized fluorescence mechanisms underlying the blue and green PL bands of the n-RCDs (RCD and PAH levels are represented on different arbitrary energy scales); (f) TR-PL decays of CDs excited at 375 nm (top) and 485 nm (bottom). The insets show the steady-state PL spectra at the corresponding λ_{exc}; the PL intensity decays were monitored in correspondence of the emission peaks, i.e. at 455 and 535 nm for λ_{exc} = 375 nm and at 535 for λ_{exc} = 485 nm [2].

TEM micrographs (Figure 3.6a) of n-RCDs shows spheroidal shaped nanoparticles with a mean size of 1.5 ± 0.3 nm (σ = 22%). FT-IR spectrum of the n-RCDs was compared to those of resorcinol and EG, the precursor and reaction solvent, respectively. The principal assignments of the stretching vibrations observed in the spectra are reported in Figure 3.6b. Namely, the spectra show a broad band at 3320 cm^{-1} due to O–H stretching, a doublet at 2950 and 2880 cm^{-1} ascribed to C–H stretching, a peak at 1603 cm^{-1} assigned to C=C vibrations and several overlapping peaks in the region at 960-1150 cm^{-1} assigned to C–O stretching.

Interestingly, the surface of the RCDs results to be characterized by –OH groups, while the spectrum does not show evidence of other functionalities like carbonyl or carboxylic groups. Furthermore, the EG characteristic C–O and C–H vibrations found in the RCD spectrum indicate the presence of residual solvent molecules within the nanoparticles. Due to the chemical affinity of the EG molecules for the surface –OH groups, it is very likely that EG molecules are linked to the surface –OH groups of the RCDs via hydrogen bonds.

The surface of the n-RCDs has a ζ-potential of ~-25 mV (Table 3.2). Such negative surface charge is ascribed to deprotonated –OH (i.e.– C–O^{-}) groups at the n-RCDs surface, and it is essential for the electrostatic colloidal stabilization of these nanoparticles.

The n-RCDs structural characterization was carried out using the Grazing Incidence Wide Angle X-Ray Scattering (GIWAXS) technique, in collaboration with Dr. Giannini and Dr. Sibillano at Institute of Cristallography (IC) – CNR of Bari (detailed instrumental and experimental conditions regarding X-ray data collection can be retrieved from [2]). The very broad peak found in the GIWAXS 1D pattern at around 22° is typically attributed to disordered graphene-like structures within CDs [13,47]. However, compared to other CDs synthesized by bottom-up reactions and similar carbonaceous precursors [39,48], this diffraction band appears very broad for the RCDs. This denotes that the structure of RCDs has a prevalent amorphous character. Nonetheless, it is also likely that the marked broadness of RCD diffraction band is partly due to the presence of distorted polyaromatic structures in these CDs, as also hypothesized by the results of the DFT simulations (Sec. 3.2.2).

The steady state spectroscopic PL properties of the n-RCDs are shown in Figure 3.6d. The PL excitation spectrum exhibits narrow bands centered at 520 nm and 415 nm, together with weaker shoulders at 490 nm and 390 nm. The PL emission spectra display a very narrow band peaked at 535 nm with a full width at half maximum (FWHM) of ~36 nm, with a weaker shoulder at 585 nm. The absolute PLQY of such green band is of ~42%, when excited at 485 nm (Table 3.2). As detailed in Sec. 3.2.1-3.2.2, this emission is ascribed to the larger OH-PAHs formed during the synthesis from resorcinol polycondensations. The small red shift of this band in the purified n-RCD nanoparticles compared to the same band observed during spectroscopic monitoring of the raw reaction batch (Figure 3.6b) can be attributed to a solvatochromic effect. More specifically, removal of EG with the purification decreases the polarity of the nanoparticle dispersing medium, producing a red shift of the emission, in agreement with T. Yoshinaga et al. [49].

Furthermore, it is worth noting that similar narrow and excitation independent PL bands were attributed in previous studies to HOMO-LUMO transitions of graphenic layers constituting the CDs [12,39,48,50–53]. Here, XRD characterization showed that n-RCDs have an amorphous carbogenic structure. Moreover, the spectroscopic monitoring of reaction proceeding, corroborated by computational results (Sec. 3.2.1-3.2.2) suggests the formation of several different OH-PAHs to which the narrow intense green emission band can be attributed (Sec. 3.2.2). Such green emitting fluorophores is found in the purified nanoparticles despite the multiple performed purification involving centrifugation and redispersion cycles. Therefore, such green emitting OH-PAH could be in principle either incorporated within the mostly amorphous carbogenic matrix of the n-RCDs or bound externally onto their surface. Nonetheless, it is worth noting that further details on where these fluorophores are positioned within the RCDs were provided by the photobleaching experiments performed on the RCDs, discussed in Sec. 3.2.5.

Alongside the prominent green PL band, the RCDs also show a weaker blue emission further reduced in intensity after the purification process (Figure 3.6b). This band exhibits excitation dependent characteristics. This can be explained considering that most of the PL intensity observed in the raw reaction batch is due to the small PAHs formed as intermediates of resorcinol polycondensations, that are removed after the purification process (Sec. 2.1.6). Therefore, in the purified nanoparticles, this blue excitation dependent band can be tentatively attributed to radiative recombination from surface or defect states of n-RCDs, in agreement with several other works on bottom-up synthesized CDs [10,31,54–57].

Therefore, to summarize, two distinct radiative recombination pathways can be individuated that contribute to the overall optical properties of the n-RCDs in the visible range. Namely, (i) a green emission from OH-PAH molecules, and (ii) blue

emission from surface or defect states. These two pathways are outlined in Figure 3.6e. Scrutinizing accurately the optical spectroscopic features of the n-RCDs we can articulate such mechanisms with more precision. In fact, specifically, the PAH emission originates from the radiative decay of two electronically excited states (S_2 and S_1) towards the ground state (S_0), giving rise to the PL excitation bands at 390-415 nm ($S_0 \rightarrow S_2$) and at 490-520 nm ($S0 \rightarrow S1$). Upon excitation with UV light (at 350–375 nm), photons can lead either to blue emission, with the mechanism depicted in Figure 3.6e (left), or to green emission, after $S_0 \rightarrow S_2$ absorption transition of the molecular PAH.

To further corroborate these attributions, the TR-PL decays of n-RCDs were investigated in correspondence of the two emission bands (Figure 3.6f), exciting by UV (375 nm) and blue (485 nm) radiation. The TR-PL decays at the green emission band (535 nm) show the same slope, independently from the λ_{exc}. However, the decay of the blue band (455 nm) exhibits a difference. More specifically, the decay of the green band can be fitted with a mono-exponential function, yielding a lifetime of (3.9±0.3) ns, which is in agreement with a mechanism of fluorescence from a molecular dye [58,59]. On the other hand, the fitting of the blue band decay requires an additional stretched component with a lifetime of (1.8±0.5) ns. This result, also in line with the excitation-dependent behavior of the blue-band observed in steady-state spectra (Figure 3.6d), confirms that this blue band arises due to more complex radiative recombination dynamics.

3.2.4. Base- and acid-catalyzed synthesis of RCDs

The direct glycothermal treatment of resorcinol without any other added chemical species to the reaction solution, proves very useful to examine the PAH formation and hence to correlate the chemical composition of the RCDs to their PL optical properties. Nonetheless, the reaction proceeds slowly under these conditions, leading to a low yield of product after the post-synthesis purification protocols. More specifically, after a reaction time of 6 h, the final mass yield of purified n-RCDs is <0.7% than the initial resorcinol mass. This is a practical limitation of this synthetic approach, as it would involve either low yields of RCDs obtained from each reaction batch or very long reaction times to obtain considerable quantities of nanoparticles. To overcome this issue, the effect of introducing two types of catalysts in the reaction solution was investigated. In particular, a base (NaOH) and an acid (H_2SO_4) were tested as catalysts, with the aim of increasing the kinetics associated with resorcinol polycondensations and carbonization reactions. This was operationally achieved introducing the catalysts in the solution subjected to the carbonization, with a minor modification of the synthetic procedure (Sec. 2.1.6).

The reaction rate in the presence of the two catalysts was analyzed monitoring the progressive dampening of the resorcinol absorption band at 276 nm (Figure 3.7a-

b). To assess the resorcinol consumption rate quantitatively, the decreasing trend of absorbance as a function of reaction time was fitted with a mono-exponential decay function (details of this fitting procedure are provided in [2]). For RCDs synthesized using NaOH base catalyst (b-RCDs), the decay has a characteristic time of ~2 h and reaches a plateau in about ~6 h, indicating that resorcinol is almost completely reacted at that reaction time. On the other hand, for RCDs obtained by H_2SO_4 acid catalysis (a-RCDs) the decay reaches a plateau in only 30 min, pointing out an even faster precursor consumption. The faster reaction kinetics for resorcinol polycondensations are attributed to the catalytic effects of OH^- and H^+ ions on these processes, potentially following mechanisms akin to those illustrated in Figure 3.7a-b.
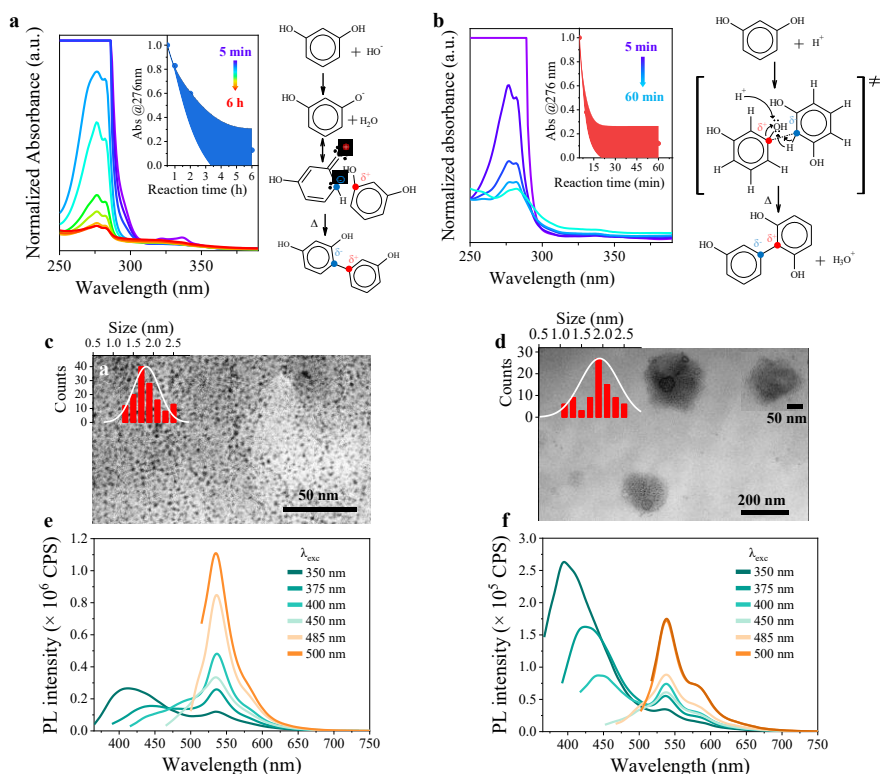
Figure 3.7: *Resorcinol UV absorption band at increasing reaction times for (a) b-CDs and (b) a-CDs; the insets show the absorbance at the band peak (276 nm) as a function of reaction time, alongside the mono-exponential decreasing fitting (solid lines) and 95% confidence interval (shaded area), the hypothesized mechanisms for base- and acid-catalyzed resorcinol polycondensations are reported; TEM micrograph and size distribution histogram (inset) of purified (c) b-RCDs and (d) a-RCDs; PL spectra at different excitation wavelengths of purified (e) b-RCDs and (f) a-RCDs [2].*

After purification, TEM micrographs reveal b-CDs as spheroidal nanoparticles with a mean size of 1.8±0.3 nm (σ = 17%, Figure 3.7c). Thus, b-RCDs exhibit similar size and shape to n-RCDs. Conversely, micrographs of a-RCDs display the presence agglomerates (∼100–200 nm sized, Figure 3.7d), containing CDs with a mean size of 1.9±0.4 nm (σ = 23%). The presence of such CDs aggregates can be explained considering the low colloidal stability of RCDs in acidic environment. FT-IR spectroscopic investigation of purified b-RCDs and a-RCDs indicates that the use of catalysts in the RCD synthesis does not lead to the introduction of new functional groups on the nanoparticles surface (Figure 3.8). However, the ζ-potential of a-RCDs results of ∼+0.5 mV, in contrast to the negative surface potential measured for n-RCDs and b-RCDs (Table 3.2). The whole experimental findings reveal that the surface of both a-RCDs, b-RCDs and n-RCDs is qualitatively composed by –O⁻ and –OH groups. Nevertheless, the relative abundance of protonated and deprotonated hydroxyl groups exhibits variability according to the reaction conditions. Notably, in the presence of acidic catalyst, protonation of surface groups leads to neutralization of the negative surface charge, weakening the a-RCDs colloidal stability and causing the nanoparticle aggregation.
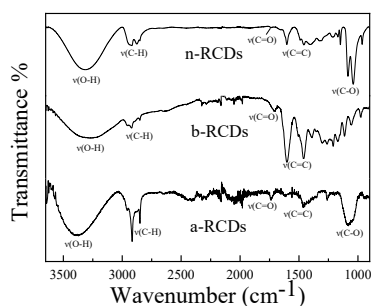
Figure 3.8: comparison of the FT-IR spectra of n-RCDs, b-RCDs and a-RCDs [2].

The formation of these agglomerates for a-RCDs is also reflected in the PL properties of the resulting purified nanoparticles (Figure 3.7e-f). Both a-RCDs and b-RCDs display PL spectra characterized by the same spectral features as n-RCDs; namely, a broad and excitation dependent blue PL band, and a narrow excitation independent green PL band. However, the bands exhibit different relative intensities and different PLQY (λ_{exc} = 485 nm). More specifically, purified b-RCDs show a blue emission band that is relatively more intense compared to the n-RCDs, while the PLQY of their green band is not changed (differences in the measured values are within the experimental error, Table 3.2). Conversely, a-RCDs display a markedly increased blue PL band compared to both n-RCDs and b-RCDs, and a green band with significantly lower PLQY (Table 3.2). Between b-RCDs and n-RCDs, the different intensity of blue band may be explained based on the different relative concentration of deprotonated –O⁻ and protonated –OH groups, altered as

a consequence of the introduction of the base catalyst. On the other hand, in a-RCDs, low PLQY of the green band may be ascribed to nanoparticle aggregation, stemming from surface negative charge neutralization resulting due to the introduction of the acid catalyst.

Table 3.2: ζ-potential and PLQY (λ_{exc} = 485nm) of n-RCDs, b-RCDs and a-RCDs.

Sample	ζ-potential (mV)	PLQY %
n-RCDs	-24.7	42±5
b-RCDs	-27.8	35±4
a-RCDs	+0.5	8±1

Considering that conducting the synthesis in the presence of an acidic catalyst produced formation of aggregates as shortcoming, basic catalysis can represent a viable solution to improve the low reaction yield of n-RCDs. In fact, b-RCDs exhibit very similar PL properties to n-RCDs (slight differences in the blue band intensity), but a significantly superior reaction yield. Specifically, after reacting for 6 h, the mass reaction yield of purified b-RCDs resulted of 17%, i.e. 250 mg of purified b-RCDs were obtained from 1.5 g of initial precursor.

3.2.5. RCD photobleaching resistance

In the perspective of implementing CDs in operational devices, it is pivotal to ascertain their resistance to degradation phenomena [5,60]. In fact, poor photochemical stability of these fluorophores could undermine the long-term efficiency of devices in which they are implemented. Herein, the resistance of RCDs to photochemical degradation was evaluated dispersing b-RCDs in ethanol and monitoring spectroscopic changes while the nanoparticles were exposed to continuous UV irradiation (further details on the experimental procedure are provided in Sec. 2.2.1). In agreement with previous works on photobleaching (PB) of CDs and molecular fluorophores [61], we can safely consider that UV irradiation induces the formation of ROSs in solution, especially from O_2 molecules dissolved in the solvent. The ROSs are expected to promote photochemical degradation reactions.
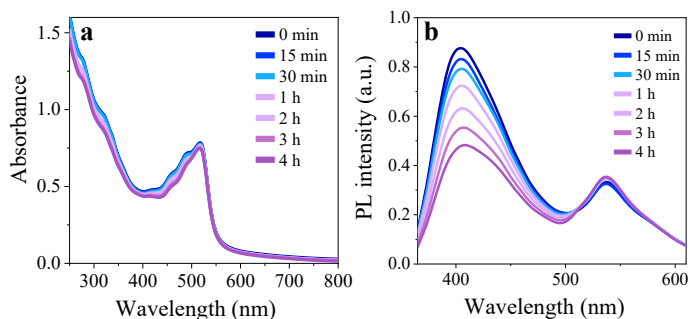
Figure 3.9*: (a) UV–Vis absorption and (b) PL spectra (λ_{exc} = 350 nm) of b-RCDs recorded at progressive UV irradiation times [2].*

After 4h of UV irradiation, the absorption spectra (Figure 3.9a) of b-RCDs exhibit only minimal variations. On the other hand, in the PL spectra, the blue emission band decreases progressively with increasing irradiation time, while the green band remains mainly unaltered.

The absence of significant dampening in both absorption and emission spectra in the green region denotes that the OH-PAH responsible for such spectroscopic features do not undergo photochemical degradation during the experiment. The observed strong quenching of the blue PL emission, accompanied by no relevant decrease in absorption in the UV portion of the spectrum (e.g. λ<400 nm) confirms the attribution of such feature to surface or defect state recombination. In fact, in surface/defect-state recombination mechanisms in CDs, absorption occurs between internal core state levels, while only radiative recombination is localized at the surface groups or defects [31,56,57]. Consequently, degradation of radiative recombination sites should be reflected only into emission quenching, without alterations of the absorption spectrum. Thus, we can safely assume that the ROSs created by UV irradiation in solution, induce degradation of b-RCD surface chemical groups, leading to observable deterioration of radiative recombinations taking place locally at those regions [60,62–64]. Vice versa, the experimental observation that the green OH-PAHs are not affected by ROS degradative action, strongly suggests that these fluorophores are not exposed to the solution, but rather located within the carbonaceous matrix of the RCDs, beyond the diffusion length of singlet molecular O_2 or other ROSs [61].

3.2.6. Characterization of RCD reversible pH sensitivity

As discussed in Sec. 3.2.3-3.2.4, the colloidal stability of RCD dispersions is tightly correlated to their negative surface charge, due to deprotonated –O⁻ groups. Protonation of surface negative groups is responsible for the formation of nanoparticle aggregates in the synthesis of a-RCDs and can be also suitably employed to induce precipitation of the RCDs in the purification protocol

(Sec.2.1.6). Therefore, it becomes pertinent to better explore the effect of introducing an acidic or basic environment on the optical properties of the RCDs.

At this aim, a stable dispersion of b-RCDs in ethanol was added with HCl and NaOH acqueous solutions in alternating steps and the variations of the RCD optical properties were monitored (further experimental details are provided in Sec. 2.1.6). In such experiment, also very small concentrations of HCl could quench the PL of the b-RCDs (Figure 3.10a). On the other hand, adding an equimolar amount of NaOH lead to restoration of PL. More specifically, PL quenching and restoration can be cyclically repeated for a certain number of times. However, after every restoration with NaOH a small loss in emission intensity is observed.
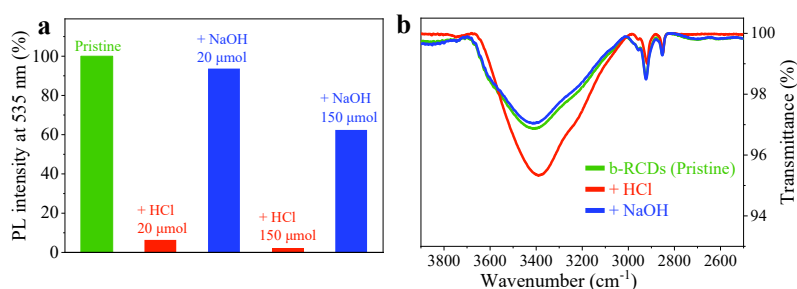
Figure 3.10: (a) PL intensity at 535 nm for pristine b-CDs and after cyclic addition of HCl_{aq} and $NaOH_{aq}$, expressed as a percentage of the initial intensity; (b) O–H stretching band observed in the FT-IR spectra of b-CDs before and after subsequent addition of HCl and NaOH [2].

In the FT-IR spectra of b-RCDs added with HCl, an increase of the strength of the O–H stretching band is observed, which is explainable with an increase of protonation of –O⁻ surface groups (Figure 3.10b). On the other hand, subsequent addition of NaOH brings back the O–H stretching band to that of the pristine b-CDs, suggesting that the protonation condition of the surface –O⁻ in the pristine dispersion is at least partially restored. These observations also align with the ζ-potential value of b-CDs after HCl and NaOH additions. In fact, ζ-potential shows no change in its average value upon NaOH addition, while it becomes very close to zero for HCl-added b-CDs (going from -27.8 mV to +0.5 mV).

3.2.7. Mechanisms underlying pH dependence of PL

The reversible modulation of the green b-RCD fluorescence (Sec. 3.2.6) can be reasonably explained taking into account the pH equilibrium reactions involving the OH-PAH fluorophore from which the emission originates. In fact, upon addition of H⁺ or OH⁻, the emitting OH-PAH undergoes protonation or deprotonation chemical reactions, leading to different acid/base conjugated forms and modifying the optical properties.

To further expand this investigation and substantiate the proposed hypothesis, an experiment was conducted in which 5 µL of a 1 M HCl aqueous solution (HCl$_{aq}$) were progressively added to a dispersion of RCDs, at the fixed concentration of 5µg/mL in a phosphate buffer at pH = 7. Spectroscopic changes in UV-Vis absorption and PL spectra (λ_{exc} = 485 nm) were monitored (Figure 3.11).
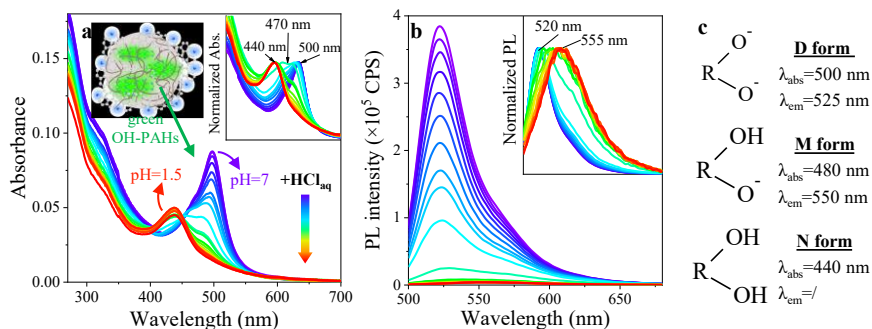
Figure 3.11: (a) UV-Vis absorption and (b) PL (λ_{exc} = 485 nm) spectra of a b-RCD dispersion at increasing HCl$_{aq}$ added volume. The top-right insets of (a) and (b) show the normalized spectra with indications of the band maxima positions. In (a) a schematic illustration of the b-RCDs with inner green OH-PAHs. Additionally, the initial and final pH values of the experiment are reported for reference. (c) schematic description of hypothesized dianion (D), monoanion (M) and neutral (N) forms of the green OH-PAHs. The respective absorption and emission (when present) maxima positions of the involved forms are also reported.

Upon the incremental addition of HCl$_{aq}$, the absorption band at 500 nm of the pristine b-RCDs dispersion exhibits a gradual bleaching and a wide blue shift. Indeed, the inset of Figure 3.11a) clearly shows that the pristine absorption band at 500 nm undergoes a transition to a band at 470 nm and finally to a band peaked at 440 nm. In parallel, a substantial quenching of the green PL peak (Figure 3.11b), with a progressive red shift of the pristine band (inset of Figure 3.11b) is noted.

Such spectroscopic variations can be explained considering that, in the pristine solution (at pH=7), the green emitting OH-PAHs have basic –CO$^-$ groups that can quantitatively react with H$^+$. Upon H$^+$ addition, these groups are progressively protonated, leading to the observed spectroscopic modifications. Conversely, after reaching a pH of 1.5, the absence of additional changes upon further HCl$_{aq}$ addition suggests that, under these pH conditions, PAHs lack –CO$^-$ groups that can quantitatively react with H$^+$.

Thus, the observed absorption and PL spectral band modifications can be collectively explained considering three distinct acid/base conjugated forms for the green emitting OH-PAHs (Figure 3.11c), namely: (i) a dianion (D) form

responsible for the pristine absorption at 500 nm and emission at 520 nm, (ii) a monoanion (M) form absorbing at around 470 nm and weakly emitting at 555 nm and (iii) a neutral (N) form, that has the absorption band peaked at 440 nm and no emission within the investigated spectral range.

To complete the exploration of the reversible acid-base reactions between the D, M and N forms, it might be also instructive to test the spectroscopic variations obtained after reactions with OH⁻ rather than with H⁺. At this scope, the acidified dispersion of b-RCDs (pH = 1.5) was added with an equimolar amount of NaOH aqueous solution (NaOH$_{aq}$). The resulting spectroscopic data of this experiment are reported and discussed in Sec. A3.1. Briefly, the spectroscopic variations lead to a fluorescence restoration retracing precisely the spectroscopic changes of the HCl quenching. However, a fluorescence intensity loss is observed, that is ascribed to irreversible phenomena occurring during such experiments, such as nanoparticle aggregation or irreversible chemical modifications of the emitting units within the RCDs, which hinder the complete restoration of the original fluorescence intensity.

In the perspective of achieving an even more comprehensive overview of the pH dependence of the RCD fluorescence, a further question to address is how the fluorescence band in the blue range responds to pH variations. At this aim, we examined the PL spectra obtained exciting at 350 nm in the UV range, thus to concomitantly observe both the blue and green fluorescence bands (Sec. 3.2.3). The resulting PL spectra are depicted in Figure 3.12a.
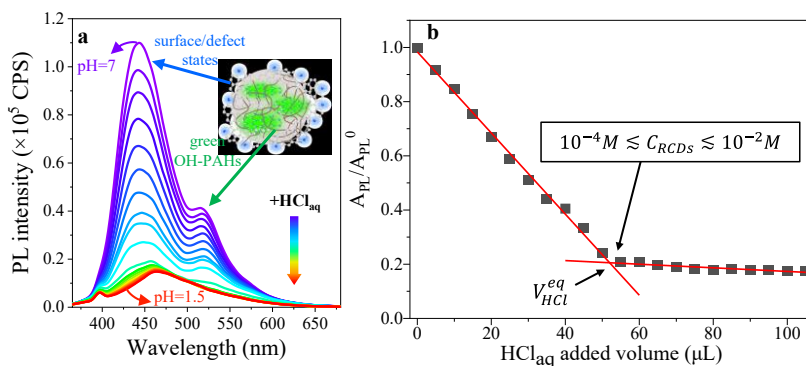
Figure 3.12: *PL spectra (λ_{exc} = 350 nm) of b-RCD dispersion at increasing HCl$_{aq}$ added volume. A schematic representation of the RCDs delineates the assignments of the blue and green bands respectively to surface/defect states and to inner planar PAHs; furthermore, the initial and final pH of the experiment are reported; (b) fluorescence titration curve reporting the ratio between the area of the PL spectra at λ_{exc} = 350 nm (A$_{PL}$) and the area of the pristine solution spectrum (A$_{PL}{}^0$) as a function of the volume of added titrant (HCl$_{aq}$). The volume of titrant at the*

equivalence point is labelled $\boldsymbol{V_{HCl}^{eq}}$; its measurement allows for calculating a range of orders of magnitude of the concentration of RCDs in the pristine solution (C_{RCDs}), as elucidated in Sec. A3.1.

With the progressive increase of HCl$_{aq}$, a gradual decrease in the intensity of both the blue and green PL bands is observed. Furthermore, as described in Sec. A3.1, the addition of NaOH$_{aq}$ to the quenched solution, leads to a restoration of the overall blue and green bands, with a fluorescence loss.

In Sec. 3.2.3-3.2.4, we attributed the blue emission band to radiative recombination occurring at surface or defect states. Reversible pH sensitivity of this band reveals that also these groups, responsible for the blue fluorescence, are subjected to reversible chemical protonation reactions, analogously to the green OH-PAHs. Considering that the surface chemistry of these CDs is characterized by variably protonated hydroxyl functionalities (Sec. 3.2.3-3.2.4), it is very likely that these reversibly protonable blue-emitting surface are also –CO$^-$ groups.

Thus, considered collectively, the results of the previous experiments evidence that the titrant (HCl) reacts quantitatively with both (i) green OH-PAHs and (ii) a fraction of the surface groups (possibly –CO$^-$) that can undergo protonation reactions. Notably, this makes possible to consider the quenching experiment also as a fluorometric titration of these species (Figure 3.12b). Consequently, with appropriate considerations on the reaction stoichiometry and on the density of emitting units present in each nanoparticle (Sec. A3.2), we can roughly evaluate the concentration of nanoparticles in the pristine dispersion. In particular, it is possible to correlate the volume of titrant at the equivalence point (V_{HCl}^{eq}) to the molar concentration of nanoparticles in the dispersion (C_{RCDs}), with the equation:

$$C_{RCDs} = \frac{C_{HCl}V_{HCl}^{eq}}{s_m d_{EM} V_{in}} \tag{3.1}$$

where C_{HCl} is the concentration of the titrant stock solution, V_{in} is the initial volume of the pristine dispersion of b-RCDs, s_m is the average stoichiometry of reactions of H$^+$ and d_{EM} is density of emitting units per RCD (Sec. A3.2).

It is evident that (3.1) allows estimating the concentration of CDs in a dispersion by means of a titration method, measuring the volume of titrant at the equivalence point, once s_m and d_{EM} are defined. However, the thorough determination of these quantities would require dedicated experimental procedures and/or theoretical modelling even more comprehensive than those described in Sec. 3.2.2. If these quantities are known, the presented approach may be exhaustively used to estimate the molar concentration of different kinds of CDs. This could be a significant step towards compensating for the lack of available procedures in the current literature allowing to estimate the number of CDs in a solution – a pivotal parameter for diverse application areas [65].

Moreover, albeit measuring experimentally s_m and d_{EM} can be challenging without appropriate experimental protocols, the orders of magnitudes of these quantities can be a priori reasonably individuated. As an example, in Sec. A3.2, a detailed discussion is provided, in which the approximate orders of magnitude for the upper and lower bounds of s_m and d_{EM} are rationally examined. By setting such rough bounds for s_m and d_{EM} and substituting the measured V_{HCl}^{eq} in (3.1), a reasonable range of order of magnitude for C_{RCDs} can be evaluated, which is 10^{-4}–10^{-2} M.

3.3. CDs from red-emitting dye "neutral red" (NR-CDs)

Many recent studies have demonstrated the exact origin and nature of fluorescence of CDs. For example, whether small nonaromatic molecules or aromatic synthetic precursors are used, the final fluorescence of CDs can be ascribed to polyaromatic or polyheterocyclic aromatic structures, that have HOMO-LUMO transitions in the visible range (Sec. 1.2) [27,66]. Such aromatic structures can arise from large sp^2 conjugated domains present in the crystalline CD core, or in the case of amorphous CDs, from organic fluorophores that are either incorporated within the nanoparticles or adsorbed to their surface. Two different examples of CDs containing such molecular fluorophores were discussed in the previous Sec. 3.1 and 3.2.

However, methods enabling a precise control of the reactions leading to the formation of such aromatic fluorophores are still actively under investigation. Thus, designing CDs with specific and well-defined optical features is an ongoing challenge. Overall, the design of synthetic protocols is particularly lacking when targeting emission in the red spectral region.

A synthetic strategy was developed as a possible alternative, where the CD optical properties are inherently defined by the carbonaceous precursor rather than resulting from fluorophores or sp^2 conjugated domains forming during polycondensation and subsequent carbonization reactions. Then, the reaction process was devised in a way that the precursor fluorescence can be retained in the CDs also after the carbonization reaction. In this way, the nanoparticle PL is not reaction-dependent, but determined *a priori*, by the selection of the organic fluorescent molecule used as precursor.

In this section, this approach of CD emission by-molecular-precursor design is demonstrated, particularly showing its feasibility in producing CDs with red emission. This points out the possible capability of this strategy to overcome the challenges encountered with other *bottom-up* strategies in obtaining CDs with tunable fluorescence in the red. At this scope, the NR dye was employed as the starting CD precursor. The selection of this carbonaceous source primarily stems from its emission in the red region. Moreover, NR is also a molecule with a relatively low cost and low toxicity, as it has been often used in contact with biological systems, as staining agent [67], probe [68], and redox mediator [69], both in *in-vitro* [70] and *in-vivo* [71] studies.

Experimental results demonstrates that the developed synthetic protocol is effectively capable of producing CDs in which NR is chemically interconnected within an amorphous carbogenic matrix. Therefore, not only its fluorescence

properties are retained in the nanoparticles, but the presence of the carbogenic matrix offers further advantages in terms of improved resistance to PB. Moreover, as will be demonstrated in Sec. 5.2, incorporation of NR in a carbogenic matrix dramatically prevents the aggregation-induced quenching of the molecular dye, allowing to observe fluorescence emission from the solid-state nanoparticles in powder and opening the way for their use in photonic and lasing applications.

3.3.1. Synthesis and characterization of NR-CDs

NR-CDs were synthesized using a reaction solution consisting of NR dissolved in EG and heated in autoclave (for synthetic details, see Sec. 2.1.7). Purified NRCDs are observed in TEM micrographs as dark dots with mean size of 5.1±1.5 nm (Figure 3.13).
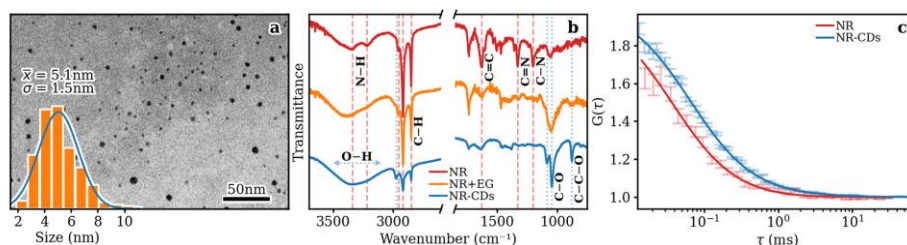
Figure 3. 13: (a) TEM micrograph of NR-CDs with the size distribution (inset); (b) FT-IR spectra of NR-CDs, NR, and NR+EG. The assignments of the identified peaks are highlighted by dashed lines; (c) FCS experimental data and fittings (continuous curves) of NR and NR-CDs [3].

To verify the formation of bonds between NR and a carbogenic matrix, a FT-IR investigation was carried out (Figure 3.13b). Specifically, the FT-IR spectrum of the nanoparticles was compared to the spectrum of NR alone, containing the IR vibrational features of the molecule, and to that of the reaction solution consisting of NR and EG non subjected to the solvothermal process. The FT-IR spectrum of NR results in the following features: N–H stretching (peaks at 3340 cm-1 and 3220 cm-1), C–H stretching (triplet at 2955 cm-1, 2920 cm-1, and 2850 cm-1), C=C aromatic stretching (1630 cm-1), C=N stretching (1330 cm-1), C–N stretching (1200 cm-1). When NR is mixed with EG in the reaction solution, a broad band appears in the spectrum between 3600 cm-1 and 3000 cm-1 (ascribable to O–H stretching), a peak at 1085 cm-1 (assigned to C–O stretching) and a peak at 880 cm-1 (a characteristic signal of alcohols arising from the stretch of the C–C–O chain). The FT-IR spectrum of the NR-CDs exhibits the characteristic C–H and C=C features of the NR, but the vibrations of C=N, C–N and C–O bonds appear modified. In particular, the C–O stretching is shifted at 1045 cm-1, while also the O–H stretching band (at 3600-3000 cm-1) is broader for the NR-CDs, compared to that registered for NR + EG. Both these alterations in the NR-CD spectrum can be explained with the formation of hydrogen bonds between NR and EG molecules in the NR-CDs. This in turn, aligns with the formation of nanoparticles during the

synthetic process, in which NR molecules and the other carbonaceous features, possibly also originating from EG, are linked together via hydrogen bonds.

Therefore, following this analysis, the NR-CDs can be envisioned as containing NR molecules bound to a carbogenic matrix. To further confirm this hypothesis, a nanoparticle dispersion in ethanol was investigated by Fluorescence Correlation Spectroscopy (FCS), in collaboration with Dr. Martorana (Institute of Biophysics Palermo Division, CNR). This technique analyzes the correlation between fluctuations of the fluorescence of a species freely diffusing in a solvent, enabling, through appropriate mathematical equations, to calculate the hydrodynamic radius (R_H) of the emitting species [72]. Similarly to DLS, this spectroscopic technique provides a calculation of hydrodynamic average size R_H. Nonetheless, FCS is specifically addressed to probing fluorescent objects, allowing to separate them from other eventual non-emissive diffusing objects in solution [73,74]. In this work, FCS autocorrelations were recorded for both NR and NRCDs, to unveil potential alterations in diffusion coefficients and hydrodynamic size. Such autocorrelations, shown in Figure 3.13c, confirm that fluorophores in NR-CDs are diffusing more slowly with respect to the NR dissolved in the solvent. This is evident from the autocorrelator ($G(\tau)$) decaying more rapidly for NR, compared to NR-CDs. To address these differences quantitatively, the autocorrelations can be fitted, allowing to obtain the diffusion times (τ) and R_H reported in Table 3.3 (further details on FCS data collection and analysis are provided in [3]).

Table 3.3: *Diffusion Time (τ) and average hydrodynamic radius (R_H) of NR-CDs and NR obtained by fitting the FCS experimental autocorrelation curves*

Sample	τ (µs)	R_H (nm)
NR-CDs	84±5	1.4±0.1
NR	37±5	0.8±0.1

The fitting results unequivocally demonstrate that the fluorophores within NR-CDs have a R_H that is twice that of the bare NR molecule. This observation supports the hypothesis that within NR-CDs, NR molecules form bonds with a carbonaceous matrix.

Spectroscopic characterization of the optical properties of NR-CDs is shown in Figure 3.14.
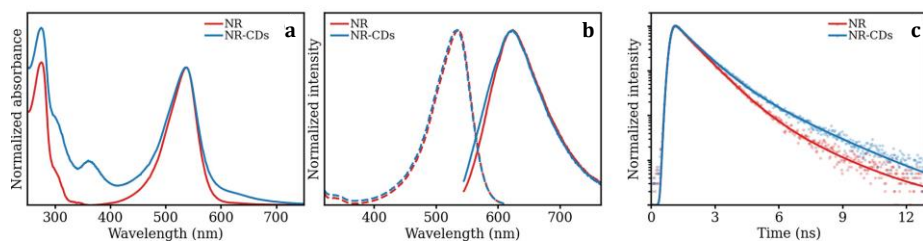
Figure 3.14: *normalized (a) UV-Vis absorption, (b) PL (λ_{exc} = 535, continuous lines) and PLE (λ_{em} = 620 nm, dashed lines) spectra and (c) TR-PL decays (λ_{exc} = 485 nm, λ_{em} = 620 nm) of NR-CDs and NR [3].*

It is very evident that the NR-CDs optical properties share several similarities with the spectroscopic properties of NR molecules, namely, the absorption and emission characteristics of NR-CDs are predominantly characterized by the molecular absorption and emission band of the dye, peaked at 535 nm (absorption) and 620 nm (emission). This is ascribed to the presence of NR molecules within the nanoparticles, in good agreement with the results of FT-IR and FCS characterization discussed above. Nonetheless, some small but informative differences can also be noted in the spectra of NR-CDs. For example, the UV-Vis absorption spectrum of NR-CDs exhibits an additional band at 360 nm. Similar bands in CDs in this spectral region have been frequently associated to n−π* transitions of CD surface groups [57,75,76]. Furthermore, the normalized absorption spectrum of NR-CDs seemingly displays a background that increases with decreasing wavelengths, that is associable to a minor scattering component, more pronounced in the nanoparticles and absent in NR molecules.

The emission peak at 620 nm has a similar line shape and also comparable QYs for NR and NR-CDs, namely, (9.3±0.3)% and (7.0±0.2)% respectively. However, a minor additional inhomogeneous broadening in the shorter wavelength region is observed for such peak only for the NR-CDs. This is ascribable to variations of the chemical surroundings of the NR molecules in the nanoparticles, as a consequence of their bonds to the carbogenic matrix. Interestingly, since this broadening is observed only in the emission spectrum but not in the excitation spectrum, we may infer that the processes leading to the inhomogeneous broadening involve the excited state of the fluorophores, while their ground state is mostly unaltered [40]. Therefore, to better explore optical feature modifications or NR when bonded to the carbonaceous matrix, the emission decay dynamics of the emission band were studied through a TR-PL investigation (Figure 3.14c). A first comparison of the decays of NR and NR-CDs evidences that the decay rate of NR-CDs is reduced with respect to the pristine precursor molecules. More specifically, fitting of TR-PL decays was performed using a bi-exponential decay as best-fitting model function (Sec. 2.2.6), in agreement with previous works [77], pointing out that NR often exhibit a bi-exponential decay, associated with the coexistence of two protonation

states of the molecule in solution. The resulting lifetimes and relative amplitudes obtained from the fitting procedure are listed in Table 3.4.

Table 3.4: lifetimes and relative pre-exponential amplitudes obtained from the fitting of TR-PL decays of NR-CDs and NR; for both fittings, the obtained chi-squared (χ^2) parameter was <1.2

Sample	A_1(%)	τ_1 (ns)	A_2 (%)	τ_2 (ns)
NR-CDs	78±3	0.9±0.1	22±3	2.1±0.1
NR	92±2	0.8±0.2	8±2	2.1±0.2

A careful comparison of these fitting parameters provides further interesting insights about the alteration of excited state dynamics of NR molecules within NR-CDs. In fact, it can be observed that the lifetimes of NR ad NR-CD display no significant variations within their experimental errors. Therefore, both NR and NR-CD decays are characterized by a faster component with lifetime of around 0.8 ns and of a relatively slower component with a lifetime of around 2.1 ns. The overall decrease in recombination rate of NR-CDs is ascribable only to a change in the relative amplitudes of the bi-exponential decay; specifically, to the increase of relative amplitude of the slower component (A_2) in NR-CDs.

This can have two possible explanations. First, the variation in relative amplitudes may reflect a difference in the relative concentrations of protonation forms of NR. This would imply that incorporation in the carbogenic matrix, involving the formation of hydrogen or other types of weak bonds between NR and other functionalities in the carbonaceous nanoparticles, alters the protonation equilibrium of NR. Second, the results can be also interpreted as a modification of the excited state of NR when embedded within the NR-CDs, i.e., the fluorophore excited states interact differently with the modified chemical surroundings when embedded in the NR-CDs. This second explanation, may also justify the observed broadening of the PL spectrum in the NR-CDs and its small variation of PLQY, taking into account the altered dipolar interactions of excited state molecules. Nonetheless, irrespective of the considered explanation, the experimentally found differences between NR and NR-CDs emission features further substantiate that NR molecules experience a different chemical environment in the cases of (i) freely dissolved in solution (as in NR sample), and (ii) bound within carbonaceous nanoparticles (as in the NR-CDs sample). Thus, this can be taken as a further prove that in NR-CDs the dye molecules are not freely diffusing in the solvent but are rather linked to the nano-objects.

3.3.2. Photobleaching resistance characterization of NR-CDs

From the characterization of NR-CDs described in the previous section, we demonstrated that these nanoparticles contain NR dye molecules bonded to a carbogenic matrix scaffold. This leads to question about the photochemical stability of these nano-objects. In fact, NR molecule, similarly to other molecular fluorophores typically display low resistance to photodegradation, which is very detrimental for numerous applications [78,79]. On the other hand, we might expect that in NR-CDs, the carbonaceous matrix has a role in protecting the NR dyes from photochemically induced degradation phenomena. As a consequence, the nanoparticles should be expected to exhibit a higher PB resistance than the bare dye. To better investigate the NR-CDs photodegradation resistance, a PB experiment was performed irradiating samples in solution under continuous UV light (Sec. 2.3.1). The PB resistance activity of NR-CDs was compared to that of the bare NR molecule and was evaluated by monitoring UV-Vis absorption spectra recorded at increasing irradiation time for both nanoparticles and dye (Figure 3.15a).
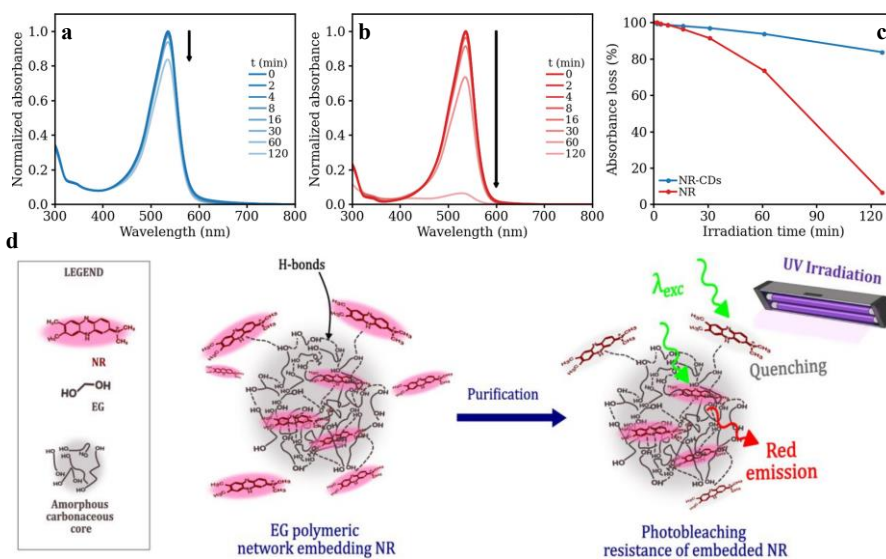
Figure 3.15: *absorption spectra of (a) NR-CDs and (b) NR recorded at increasing UV irradiation times; (c) absorbance loss over time of NR-CDs and NR upon UV irradiation; (d) schematic description of formation, structure, and PB behavior of NR-CDs [3].*

The results highlight that NR-CDs display a substantially enhanced resistance to PB compared to the bare NR. In fact, after an irradiation time of 2 h, the free molecular dye results almost completely degraded. On the contrary, at the same irradiation time the absorption in NR-CDs is only minimally altered.

Very interestingly, this points out that the carbonaceous matrix has an important role in determining an increased PB resistance for the nanoparticles. Moreover, the remarkable capability of NR-CDs to protect the fluorophores suggests that the dye molecules may be mostly enclosed within their carbonaceous matrix rather than simply adsorbed at the nanoparticle surface. In fact, only the presence of a matrix in the surroundings of the NR molecules could account for a protective effect from the oxidation action of photochemical reactions.

In the first instance, based on results of NR-CDs characterizations and the observed enhanced PB resistance, it can be hypothesizes that nanoparticles are formed after thermally induced cross-linking and condensation of EG molecules (constituting the reaction medium), assisted from the NR dye molecules (Figure 3.15d). To further support this hypothesis, computational chemistry simulations were performed in collaboration with the group of Prof. Carbonaro at University of Cagliari. Detailed computational methods are described in [3]. The simulations consisted in comparing the bare NR molecule with composites, made of a NR molecule interacting with a carbonaceous structure that models the carbogenic matrix of the CDs [80]. More specifically, accounting for the formation of polymeric amorphous structures form EG molecules, the carbogenic matrix model consisted in a polymeric chain composed of four monomer units of EG (PEG). In general, linking of NR to PEG via different bonds was considered. As representative example, Figure 3.16a shows the comparison between vibronic transitions of NR and composite of NR interacting with PEG via hydrogen bonding on NR primary amino group (NR&PEG).
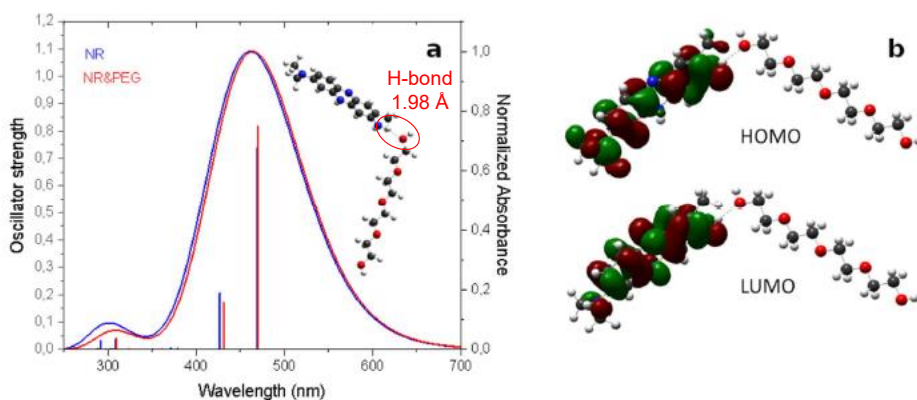
Figure 3.16*: (a) computed oscillator strengths (vertical lines) and reconstructed UV-Vis spectra of NR and NR&PEG models, the inset shows the representation of NR&PEG having a hydrogen bond (length of 1.98 Å) between NR and PEG; (b) molecular orbitals of HOMO and LUMO states for the NR&PEG system. White sphere = H atom, gray sphere = C atom, red sphere = O atom, and blue sphere = N atom; isocontour value 0.02 a.u. [3].*

First, the optimized ground state structure displays a hydrogen bond of 1.98 Å between a terminal O atom of PEG and a H atom of the primary amine group of NR (inset of Figure 3.16). The computed HOMO−LUMO transition of both NR and NR&PEG is not coincident with that observed experimentally in UV-Vis absorption spectra of NR and NR-CDs dissolved in solution (Figure 3.14a). This is due to the fact that the correct HOMO-LUMO gap position can be retrieved only after applying the proper vibronic correction [81,82]. However, we are interested in the comparison between simulated NR and NR&PEG. The simulation results, as expected, show optical features of the composite very similar to those of the bare NR molecule. Specifically, the HOMO-LUMO gap positions are at 469 and 470 nm for NR and NR&PEG respectively, thus displaying a spectral distance of only 1 nm. The molecular orbitals of HOMO and LUMO (Figure 3.16b) further indicate that the transition is accomplished without the involvement of the PEG system.

Thus, the computational simulation results further support the proposed NR-CD model, depicted in Figure 3.15d. As a result, the NR-CDs can be represented schematically as very small nano-objects consisting of NR molecules and other carbonaceous structures deriving from EG carbonization that are bonded together via hydrogen bonds. In purified nanoparticles, only NR molecules that are exposed to the outer solution undergo photochemical degradation, while other NR molecules, that are situated in the inner carbogenic network, can be effectively protected from PB.

Appendix

A3.1 Reversibility of RCD fluorescence quenching by addition of NaOH

To examine the spectroscopic details underlying the reversibility of the quenching of fluorescence, the HCl-quenched dispersion of b-RCDs obtained in the experiment described in Sec. 3.2.7 (Figure 3.11-3.12) was added with NaOH, tracing back the number of moles of previously added H^+. In particular, a 1 M $NaOH_{aq}$ ($NaOH_{aq}$) solution was added up to reach a final volume of 150 μL, equal to the total volume of previously added HCl_{aq}. In Figure A3.1, the resulting absorption and PL (λ_{exc} = 485 nm, λ_{exc} = 350 nm) spectra are depicted, and the spectra of the pristine solution are also included for reference.
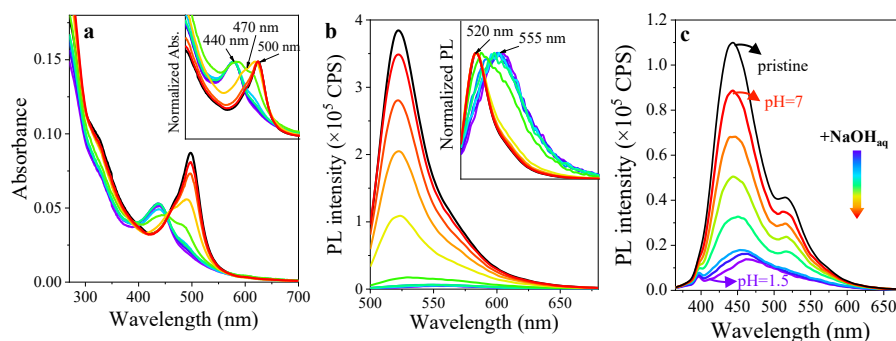
***Figure A3.1**: (a) UV-Vis absorption, (b) PL (λ_{exc} = 485 nm) and (c) PL (λ_{exc} = 350 nm) spectra of the quenched RCD dispersion at increasing $NaOH_{aq}$ added volume; the spectra of the pristine solution (black lines) are also reported for reference. The top-right insets of (a) and (b) show the normalized UV-Vis and PL (λ_{exc} = 485 nm) spectra with indications of the band maxima positions. (c) also reports the initial and final pH of the experiment as a guide for the reader.*

It is possible to observe that both the absorption and PL (λ_{exc} = 485 nm, λ_{exc} = 350 nm) features mirror the spectroscopic changes observed in the experiment of quenching by HCl_{aq} (Sec. 3.2.7). Specifically, the absorption band at 440 nm in the quenched solution is shifted to 470 nm and then to 500 nm upon the increase of $NaOH_{aq}$ quantity. Correspondingly, the quenched PL peak is progressively restored in intensity and blue shifted until reaching the same line shape of the pristine solution. However, a loss of fluorescence is observed after the addition of the equivalent volume of base. Such behavior is due to irreversible processes occurring to the b-RCDs during the quenching and restoration processes, such as aggregation or possible other types of nanoparticle damaging caused by the HCl addition (Sec. 3.2.6).

As final remark, upon excitation at 350 nm, not only a reversible quenching and restoration of the overall spectral intensity is obtained, but also a change in the relative intensity of the blue and green PL bands. This can be easily shown by plotting the ratio of the intensities of the two bands recorded at their maxima (i.e. 445 nm and 520 nm), as a function of volume of added titrant, namely HCl and NaOH respectively for the experiments of quenching and restoration (Figure A3.2).
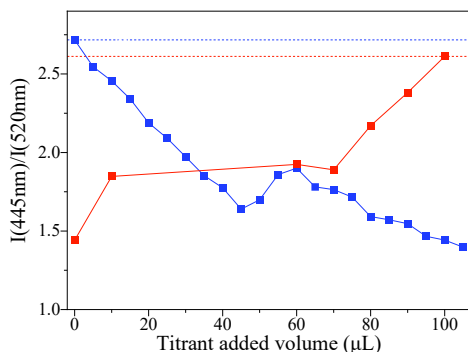
Figure A3.2: ratio of intensities recorded at the maxima of the blue (at 445 nm) and green (at 520nm) PL bands of RCDs in the experiments of quenching via HCl$_{aq}$ addition (blue squares and line) and restoration via NaOH$_{aq}$ addition (red squares and line). The ratios of blue and green PL bands of the pristine solution (horizontal blue dashed line) and of the solution after PL restoration (horizontal red dashed line) are also highlighted.

For the quenching experiment (blue squares and line), the 445 nm-to-520 nm PL intensity ratio shows two uniform progressive decrease trends in the range of added titrant volume from 0 to 45 µL and from 60 to 105 µL, interspaced by a small increasing trend from 45 to 60 µL. On the other hand, in the restoration experiment (red squares and line) the ratio between blue and green PL band intensities undergoes an increase upon addition of the first 10 µL of titrant (NaOH$_{aq}$), then it remains constant up to a volume of 70µL, after which it progressively increases up to reach around the value of the pristine solution at the added NaOH$_{aq}$ volume of 105µL. The results collectively show that the blue and green PL bands not only individually can be reversibly quenched and restored, but also their ratio undergoes some reversible variations as an effect of quantitative reactions with HCl and NaOH. Notably, these spectral changes constitute the foundation for the application of the fluorescence colorimetry revelation approach, described in Chapter 5.

A3.2 Derivation of molar concentration of nanoparticles in the dispersion (C_{RCDs}), and calculation of order of magnitude range

Upon addition of the titrant (HCl), H^+ ions react quantitatively with any molecule in the CDs having $-CO^-$ groups that can be protonated. In general, a fraction ($f \geq 1$) of such protonable molecules (PM) will be emissive upon excitation at 350 nm (contributing to either the blue or the green PL band). In the following, the emitting species containing anionic $-CO^-$ groups will be named "protonable emitting molecules" (PEM). Therefore, we have:

$$n_{PEM} = \frac{n_{PM}}{f} \qquad \qquad \text{(A3.1)}$$

where n_{PM} and n_{PEM} are the moles of PM and PEM. If each PEM contains a single $-CO^-$ group, then at the equivalence point, the moles of titrant (n_{HCl}^{eq}) will equal the moles of PEM (n_{PEM}). This is equivalent to assuming a 1:1 stoichiometry for the titration [83,84]. However, it can be recognized that in the present case the stoichiometry is not equal to 1:1. In fact, as shown in Sec. 3.2.7, the green emitting OH-PAHs have two acid/base conjugated forms forming a double protonation equilibrium, so that 2 moles of H^+ are needed to transform the D form into the completely protonated N form. Likewise, it is possible that also the protonable entities responsible for the blue emission have a higher-than-one stoichiometry.

Therefore, we have to consider that in general, each PEM contains more than one $-CO^-$ group. Consequently, each mole of PEM will react with more than one mole of titrant, so that at the equivalence point:

$$n_{PEM} < n_{HCl}^{eq} \qquad \qquad \text{(A3.2)}$$

A well-established approach to circumvent this problem is the use of an average stoichiometry for the titration reaction [83,84]. Employing this method thus leads to the following equation at equivalence point:

$$n_{PEM} = \frac{n_{HCl}^{eq}}{s_m} \qquad \qquad \text{(A3.3)}$$

where the average stoichiometry coefficient s_m represent the average number of H^+ needed to fully protonate a PEM.

Substituting (A3.3) into (A3.1) we have:

$$n_{PM} = \frac{f \, n_{HCl}^{eq}}{s_m} \qquad \qquad \text{(A3.4)}$$

n_{HCl}^{eq} can be calculated as:

$$n_{HCl}^{eq} = C_{HCl} \, V_{HCl}^{eq} \qquad (A3.5)$$

Where C_{HCl} is the concentration of titrant solution and V_{HCl}^{eq} is the measured titrant volume at the equivalence point.

Substituting (A3.5) into (A3.4) we have:

$$n_{PM} = \frac{f \, C_{HCl} V_{HCl}^{eq}}{s_m} \qquad (A3.6)$$

We can now define the average number of PM contained in a RCD, called d_{PM}:

$$d_{PM} = \frac{n_{PM}}{n_{RCDs}} \qquad (A3.7)$$

where n_{RCDs} is the number of moles of RCDs.

Substituting (A3.7) into (A3.6) we obtain:

$$n_{RCDs} = \frac{C_{HCl}V_{HCl}^{eq}}{s_m} \left(\frac{f}{d_{PM}} \right) \qquad (A3.8)$$

From (A3.1) and (A3.7) it can be easily seen that:

$$\left(\frac{f}{d_{PM}} \right)^{-1} = \frac{n_{PEM}}{n_{CDs}} \qquad (A3.9)$$

In other words, $\left(\frac{f}{d_{PM}} \right)^{-1}$ is the density of PEM per RCD, that we can call d_{PEM}. In general, quenching experiments in Sec. 3.2.7 (Figure 3.11-3.12) have shown that emission (both in the blue and in the green band) and the presence of protonable –O$^-$ groups in the corresponding molecular species are strictly correlated. Consequently, most emitting units in the RCDs is protonable and can safely derive that:

$$d_{EM} \approx d_{PEM} \qquad (A3.10)$$

where d_{EM} is the number of emitting units per RCD. Substituting (A3.10) into (A3.8) we obtain:

$$n_{CDs} = \frac{C_{HCl}V_{HCl}^{eq}}{s_m d_{EM}} \qquad (A3.11)$$

Lastly, dividing each member of (A3.11) for the initial volume of the CD solution (V_{in}) leads to (3.1).

To set the maximum order of magnitudes for C_{RCDs} we can start by considering the lower and upper bounds for the parameters for s_m and d_{EM}.

To find a lower bound for s_m we note that all PMs in the RCDs have at least one protonable –CO$^-$ group. For example, as demonstrated in Sec. 3.2.7 the green emitting OH-PAH in D form has two protonable –CO$^-$ groups, while the species responsible for the blue emission has also at least one protonable group. Therefore, it can be easily inferred that:

$$s_m \geq 1 \qquad (A3.12)$$

Analogously, a lower bound for d_{EM} can be easily found simply noting that each RCD contains at least one emitting unit. This is in fact very reasonable based on our previous characterization of the size, structure, and chemical composition of these nanoparticles (Sec. 3.2.3-3.2.4). Consequently, we have:

$$d_{EM} \geq 1 \qquad (A3.13)$$

At this point, we note that both s_m and d_{EM} are at the denominator of (3.1) and that both these terms ≥ 1. Therefore, an increase of either s_m or d_{EM} will cause a decrease in the obtained C_{RCDs}. We can therefore assert that the maximum order of magnitude of C_{RCDs} is obtained by substituting in (3.1) the lowest possible values for both s_m and d_{EM} (i.e. 1). Consequently, we find that:

$$C_{RCDs} \leq \frac{C_{HCl} V_{HCl}^{eq}}{V_{in}} \qquad (A3.14)$$

and substituting in (A3.14) the appropriate values for C_{HCl} (i.e. 1 M), V_{HCl}^{eq} (i.e. ~50 μL) and V_{in} (i.e. 1 mL), we obtain:

$$C_{RCDs} \lesssim 10^{-2} M \qquad (A3.15)$$

To set the lower bound for C_{RCDs}, we can analogously consider the maximum values that s_m and d_{EM} can assume.

To define an upper bound for s_m., we have to consider what is the maximum number of –CO$^-$ groups per PM. In this regard, we can safely affirm that the number of –CO$^-$ groups per PM is lower than the total number of –OH groups in the molecule. As a consequence, we consider as a very trustworthy upper bound for s_m:

$$s_m \lesssim 10 \qquad (A3.16)$$

in fact, even the largest OH-PAHs simulated in Sec. 3.2.2 have less than 10 substituting –OH groups and in general, it is very unlikely that a single PM has 10 functional groups and that all of them can be concomitantly deprotonated.

To establish an upper bond for d_{EM}, we have to consider what is the maximum number of emitting molecules for each RCD. We consider as a very reliable limit:

$$d_{EM} \lesssim 50 \qquad (A3.17)$$

in fact, since the average size of the RCDs is 1.5 nm it is very unlikely that more than several tens of emitting units are found in a single nanoparticle.

With these considerations, the upper bound for C_{RCDs} results:

$$C_{RCDs} \geq \frac{C_{HCl}V_{HCl}^{eq}}{500\ V_{in}} \qquad (A3.18)$$

and substituting C_{HCl}, V_{HCl}^{eq} and V_{in} with their respective values, we obtain:

$$C_{RCDs} \gtrsim 10^{-4}M \qquad (A3.19)$$

References

[1] G. Minervini, A. Madonia, A. Panniello, E. Fanizza, M.L. Curri, M. Striccoli, Nanomaterials 13 (2023) 374.

[2] G. Minervini, A. Panniello, A. Madonia, C.M. Carbonaro, F. Mocci, T. Sibillano, C. Giannini, R. Comparelli, C. Ingrosso, N. Depalo, E. Fanizza, M.L. Curri, M. Striccoli, Carbon 198 (2022) 230–243.

[3] A. Madonia, G. Minervini, A. Terracina, A. Pramanik, V. Martorana, A. Sciortino, C.M. Carbonaro, C. Olla, T. Sibillano, C. Giannini, E. Fanizza, M.L. Curri, A. Panniello, F. Messina, M. Striccoli, ACS Nano 17 (2023) 21274–21286.

[4] M.G. Giordano, G. Seganti, M. Bartoli, A. Tagliaferro, Molecules 28 (2023) 2772.

[5] A. Sciortino, A. Cannizzo, F. Messina, C 4 (2018) 67.

[6] S. Zhu, Y. Song, X. Zhao, J. Shao, J. Zhang, B. Yang, Nano Res. 8 (2015) 355–381.

[7] L. Đorđević, F. Arcudi, M. Cacioppo, M. Prato, Nat. Nanotechnol. 17 (2022) 112–130.

[8] Y. Huo, S. Xiu, L.-Y. Meng, B. Quan, Chemical Engineering Journal 451 (2023) 138572.

[9] B. Wang, G.I.N. Waterhouse, S. Lu, Trends in Chemistry 5 (2023) 76–87.

[10] A. Sharma, J. Das, Journal of Nanobiotechnology 17 (2019) 92.

[11] Y. Liu, F. Liang, J. Sun, R. Sun, C. Liu, C. Deng, F. Seidi, Nanomaterials 13 (2023) 2869.

[12] M. Moniruzzaman, B. Anantha Lakshmi, S. Kim, J. Kim, Nanoscale 12 (2020) 11947–11959.

[13] Y. Song, S. Zhu, S. Zhang, Y. Fu, L. Wang, X. Zhao, B. Yang, J. Mater. Chem. C 3 (2015) 5976–5984.

[14] A. Cappai, C. Melis, L. Stagi, P.C. Ricci, F. Mocci, C.M. Carbonaro, J. Phys. Chem. C 125 (2021) 4836–4845.

[15] K. Dimos, Polymers 10 (2018) 1312.

[16] P. Kumar, S. Dua, R. Kaur, M. Kumar, G. Bhatt, RSC Advances 12 (2022) 4714–4759.

[17] Y.-P. Sun, B. Zhou, Y. Lin, W. Wang, K.A.S. Fernando, P. Pathak, M.J. Meziani, B.A. Harruff, X. Wang, H. Wang, P.G. Luo, H. Yang, M.E. Kose, B. Chen, L.M. Veca, S.-Y. Xie, J. Am. Chem. Soc. 128 (2006) 7756–7757.

[18] E. Liu, D. Li, X. Zhou, G. Zhou, H. Xiao, D. Zhou, P. Tian, R. Guo, S. Qu, ACS Sustainable Chem. Eng. 7 (2019) 9301–9308.

[19] Y. Qu, X. Bai, D. Li, X. Zhang, C. Liang, W. Zheng, S. Qu, Journal of Colloid and Interface Science 613 (2022) 547–553.

[20] Y. Hailing, L. Xiufang, W. Lili, L. Baoqiang, H. Kaichen, H. Yongquan, Z. Qianqian, M. Chaoming, R. Xiaoshuai, Z. Rui, L. Hui, P. Pengfei, S. Hong, Nanoscale 12 (2020) 17222–17237.

[21] M. Zhang, X. Zhao, Z. Fang, Y. Niu, J. Lou, Y. Wu, S. Zou, S. Xia, M. Sun, F. Du, RSC Advances 7 (2017) 3369–3375.

[22] P. Sarkar, S. Ghosh, K. Sarkar, Colloids and Surfaces B: Biointerfaces 197 (2021) 111382.

[23] A. Sachdev, I. Matai, P. Gopinath, RSC Advances 4 (2014) 20915–20921.

[24] C. Liu, P. Zhang, X. Zhai, F. Tian, W. Li, J. Yang, Y. Liu, H. Wang, W. Wang, W. Liu, Biomaterials 33 (2012) 3604–3613.

[25] B. Han, W. Wang, H. Wu, F. Fang, N. Wang, X. Zhang, S. Xu, Colloids and Surfaces B: Biointerfaces 100 (2012) 209–214.

[26] D. Li, P. Jing, L. Sun, Y. An, X. Shan, X. Lu, D. Zhou, D. Han, D. Shen, Y. Zhai, S. Qu, R. Zbořil, A.L. Rogach, Advanced Materials 30 (2018) 1705913.

[27] S. Qu, D. Zhou, D. Li, W. Ji, P. Jing, D. Han, L. Liu, H. Zeng, D. Shen, Advanced Materials 28 (2016) 3516–3521.

[28] H. Ehtesabi, Z. Hallaji, S. Najafi Nobar, Z. Bagheri, Microchim Acta 187 (2020) 150.

[29] A. Madonia, M. Martin-Sabi, A. Sadaoui, L. Ruhlmann, S. Ammar, D. Schaming, Materials Research Bulletin 149 (2022) 111721.

[30] C.M. Carbonaro, R. Corpino, M. Salis, F. Mocci, S.V. Thakkar, C. Olla, P.C. Ricci, C 5 (2019) 60.

[31] V. Nguyen, J. Si, L. Yan, X. Hou, Carbon 95 (2015) 659–663.

[32] Y. Cheng, G. Yu, Molecules 28 (2023) 7473.

[33] M.M. Hussain, W.U. Khan, F. Ahmed, Y. Wei, H. Xiong, Chemical Engineering Journal 465 (2023) 143010.

[34] D. Benner, P. Yadav, D. Bhatia, Nanoscale Adv. 5 (2023) 4337–4353.

[35] Z. He, Y. Sun, C. Zhang, J. Zhang, S. Liu, K. Zhang, M. Lan, Carbon 204 (2023) 76–93.

[36] K. Jiang, S. Sun, L. Zhang, Y. Lu, A. Wu, C. Cai, H. Lin, Angewandte Chemie International Edition 54 (2015) 5360–5363.

[37] S. Xue, P. Li, L. Sun, L. An, D. Qu, X. Wang, Z. Sun, Small 19 (2023) 2206180.

[38] J. Han, J. Hong, H. Lee, S. Choi, K. Shin, M. Gu, S.-H. Kim, European Polymer Journal 197 (2023) 112354.

[39] F. Yuan, P. He, Z. Xi, X. Li, Y. Li, H. Zhong, L. Fan, S. Yang, Nano Res. 12 (2019) 1669–1674.

[40] J.R. Lakowicz, Principles of Fluorescence Spectroscopy, 3rd ed., Springer US, 2006.

[41] M. Fu, F. Ehrat, Y. Wang, K.Z. Milowska, C. Reckmeier, A.L. Rogach, J.K. Stolarczyk, A.S. Urban, J. Feldmann, Nano Lett. 15 (2015) 6030–6035.

[42] B. Shi, D. Nachtigallová, A.J.A. Aquino, F.B.C. Machado, H. Lischka, J. Phys. Chem. Lett. 10 (2019) 5592–5597.

[43] M.A. Sk, A. Ananthanarayanan, L. Huang, K.H. Lim, P. Chen, J. Mater. Chem. C 2 (2014) 6954–6960.

[44] J. Prakash, A.K. Mishra, Sci Rep 10 (2020) 8921.

[45] H.V. Hayes, W.B. Wilson, L.C. Sander, S.A. Wise, A.D. Campiglia, Anal. Methods 10 (2018) 2668–2675.

[46] B.M. Sahoo, R. B.V.V., B. Banik, D.P. Borah, Current Organic Synthesis 17 (2020).

[47] B.D. Mansuriya, Z. Altintas, Nanomaterials 11 (2021) 2525.

[48] F. Yuan, T. Yuan, L. Sui, Z. Wang, Z. Xi, Y. Li, X. Li, L. Fan, Z. Tan, A. Chen, M. Jin, S. Yang, Nat Commun 9 (2018) 2249.

[49] T. Yoshinaga, M. Shinoda, Y. Iso, T. Isobe, A. Ogura, K. Takao, ACS Omega 6 (2021) 1741–1750.

[50] F. Yan, H. Zhang, N. Yu, Z. Sun, L. Chen, Sensors and Actuators B: Chemical 329 (2021) 129263.

[51] P.D. Khavlyuk, E.A. Stepanidenko, D.P. Bondarenko, D.V. Danilov, A.V. Koroleva, A.V. Baranov, V.G. Maslov, P. Kasak, A.V. Fedorov, E.V. Ushakova, A.L. Rogach, Nanoscale 13 (2021) 3070–3078.

[52] M. Sun, C. Liang, Z. Tian, E.V. Ushakova, D. Li, G. Xing, S. Qu, A.L. Rogach, J. Phys. Chem. Lett. 10 (2019) 3094–3100.

[53] J. Wang, C. Cheng, Y. Huang, B. Zheng, H. Yuan, L. Bo, M.-W. Zheng, S.-Y. Yang, Y. Guo, D. Xiao, J. Mater. Chem. C 2 (2014) 5028–5035.

[54] Z. Gan, H. Xu, Y. Hao, Nanoscale 8 (2016) 7794–7807.

[55] N. Dhenadhayalan, K.-C. Lin, R. Suresh, P. Ramamurthy, J. Phys. Chem. C 120 (2016) 1252–1261.

[56] A. Sciortino, E. Marino, B. van Dam, P. Schall, M. Cannas, F. Messina, J. Phys. Chem. Lett. 7 (2016) 3419–3423.

[57] A. Demchenko, C 5 (2019) 71.

[58] J.A. Snyder, P. Grüninger, H.F. Bettinger, A.E. Bragg, J. Phys. Chem. A 121 (2017) 5136–5146.

[59] J.M. Alvarez-Pez, L. Ballesteros, E. Talavera, J. Yguerabide, J. Phys. Chem. A 105 (2001) 6320–6332.

[60] A.V. Longo, A. Sciortino, M. Cannas, F. Messina, Phys. Chem. Chem. Phys. 22 (2020) 13398–13407.

[61] A.P. Demchenko, Methods Appl. Fluoresc. 8 (2020) 022001.

[62] N. Javed, D.M. O'Carroll, Part. Part. Syst. Charact. 38 (2021) 2000271.

[63] W. Wang, B. Wang, H. Embrechts, C. Damm, A. Cadranel, V. Strauss, M. Distaso, V. Hinterberger, D.M. Guldi, W. Peukert, RSC Adv. 7 (2017) 24771–24780.

[64] W. Wang, C. Damm, J. Walter, T.J. Nacken, W. Peukert, Phys. Chem. Chem. Phys. 18 (2016) 466–475.

[65] J. Shang, X. Gao, Chem. Soc. Rev. 43 (2014) 7267–7278.

[66] X. Yang, L. Ai, J. Yu, G.I.N. Waterhouse, L. Sui, J. Ding, B. Zhang, X. Yong, S. Lu, Science Bulletin 67 (2022) 1450–1457.

[67] W.M. Clark, M.E. Perkins, J. Am. Chem. Soc. 54 (1932) 1228–1248.

[68] L. Xu, J. Wang, N. Sun, M. Liu, Y. Cao, Z. Wang, R. Pei, Chem. Commun. 52 (2016) 14330–14333.

[69] L.S. Pierson, E.A. Pierson, Appl Microbiol Biotechnol 86 (2010) 1659–1670.

[70] K.W. Woodburn, N.J. Vardaxis, J.S. Hill, A.H. Kaye, D.R. Phillips, Photochemistry and Photobiology 54 (1991) 725–732.

[71] J.C. LaManna, K.A. McCracken, Analytical Biochemistry 142 (1984) 117–125.

[72] J.R. Lakowicz, ed., in: Principles of Fluorescence Spectroscopy, Springer US, Boston, MA, 2006, pp. 797–840.

[73] L. Yu, Y. Lei, Y. Ma, M. Liu, J. Zheng, D. Dan, P. Gao, Frontiers in Physics 9 (2021).

[74] R. Rigler, E. Elson, Fluorescence Correlation Spectroscopy: Theory and Applications, Springer, Berlin ; New York, 2001.

[75] A. Sharma, T. Gadly, S. Neogy, S.K. Ghosh, M. Kumbhakar, J. Phys. Chem. Lett. 8 (2017) 1044–1052.

[76] J.-R. Macairan, T.V. de Medeiros, M. Gazzetto, F. Yarur Villanueva, A. Cannizzo, R. Naccache, Journal of Colloid and Interface Science 606 (2022) 67–76.

[77] M.K. Singh, H. Pal, A.C. Bhasikuttan, A.V. Sapre, Photochemistry and Photobiology 68 (1998) 32–38.

[78] B.P. Pathrose, A. Prakash, V.P.N. Nampoori, P. Radhakrishnan, H. Sahira, A. Mujeeb, Optik 156 (2018) 988–993.

[79] S. Sinha, A.K. Ray, S. Kundu, S. Sasikumar, S.K.S. Nair, K. Dasgupta, Appl Phys B 72 (2001) 617–621.

[80] F. Mocci, L. de Villiers Engelbrecht, C. Olla, A. Cappai, M.F. Casula, C. Melis, L. Stagi, A. Laaksonen, C.M. Carbonaro, Chem. Rev. 122 (2022) 13709–13799.

[81] A. Baiardi, J. Bloino, V. Barone, J. Chem. Theory Comput. 9 (2013) 4097–4115.

[82] V.V. Kostjukov, J Mol Model 28 (2022) 103.

[83] Z.-X. Wang, N. Ravi Kumar, D.K. Srivastava, Analytical Biochemistry 206 (1992) 376–381.

[84] N.P. Kazmierczak, J.A. Chew, D.A. Vander Griend, Journal of Chemometrics 36 (2022) e3409.

4

Photobleaching of CDs and Enhancement of Red Emission

"Spectroscopy has unveiled the exquisite beauty of the molecular world. It is the key to understanding the dance of atoms and unraveling the secrets of nature."

Ahmed Zewail

Abstract

The chapter explores advanced characterizations of CDs aimed at examining their photochemical resistance and the enhanced red emission through interaction with plasmonic nanoparticles. The first section focuses on a study carried out in the frame of PRIN 2017 CANDL[2] project, consisting in the use various pulsed laser techniques for a comparative assessment of different types of CDs. Oil-dispersible CDs (OCDs) were synthesized *via* a colloidal approach and relationships between chemical composition and their PB resistance features were discussed. The study also unveiled important details on the nature of molecular fluorophores present as emitting species in the CDs. The second section describes a work aimed at enhancing red PL of CDs through plasmonic resonance energy transfer (PRET) interactions. Colloidal chemistry methods were applied to synthesize gold nanoparticles (AuNPs) and modify their surface to promote effective coupling with CDs. After surface chemistry optimizations and combining the use of ultrafast spectroscopic techniques it was possible to obtain a significant red PL enhancement and unveil the detailed photophysical dynamics underlying this process. This chapter references published works: ACS Appl. Mater. Interfaces, 2022 [1], Materials Research Bulletin 149 (2022) 111746 [2].

4.1. Oil-dispersible CDs (OCDs) for evaluation of photobleaching resistance

As elucidated in Sec. 3.1, and evidenced by recent literature [3–11], many CDs feature large sp^2 aromatic domains or molecular fluorophores as primary sources of nanoparticle fluorescence. These fluorophores may be either embedded within the carbogenic matrix or adsorbed onto the nanoparticle surface. Notoriously, low resistance to photochemical degradation is a well-known shortcoming of molecular fluorophores, as unfortunately observed in many applications [12–14].

As commonly recognized, the susceptibility of molecular dyes to ageing or PB is strongly correlated to their chemical structures having aromatic or heteroaromatic cycles, that are particularly predisposed to chemical oxidation. Therefore, attribution of CD fluorescence to polyaromatic structures or molecules, leads to question whether incorporation or in general, bonding of these species to a carbogenic matrix holds some advantage in terms of improvement of photochemical degradation resistance.

In Sec. 3.2 and 3.3 it was found that the nano-carbogenic matrix has a remarkable protective effect on the optically active fluorophores, as demonstrated for both luminescent OH-PAHs in RCDs and NR dye in NR-CDs. This led to further address the same question in relation to CDs synthesized by solvothermal methods, or in general, with different *bottom-up* preparation techniques. Therefore, in the work presented in this section, the photochemical resistance of a broad variety of CDs, synthesized with different preparative approaches and with PL spanning across the whole visible range was deeply studied in a comparative fashion.

The work was carried out in collaboration with other partners in the frame of the project PRIN 2017 CANDL[2] (Prot. 2017W75RAE), specifically with University of Sassari (Prof. L. Malfatti), University of Cagliari (Prof. C. M. Carbonaro), CNR-IPCF of Bari (Dr. Marinella Striccoli) and University of Palermo (Prof. F. Messina). Each partner was in charge of providing CD samples for PB analysis, obtained by different synthetic approaches and grouped as a function of their emission wavelength. My contribution entailed providing a sample of CDs for investigation, namely oil-dispersible CDs (OCDs) obtained by a colloidal approach [15], and actively participating in the analysis of experimental outcomes. PB experiments employing pulsed laser-induced techniques were carried out under the responsibility of the group of Prof. Messina at University of Palermo.

The effort focused on delineating distinctions in the photobleaching mechanism of the tested CDs, correlating these differences to the surface chemistry and to the preparation protocol specific to my sample. Thanks to the employed characterizations and comparisons it was possible to elucidate very interesting

details regarding the nature of the emissive centers in the CDs and the factors determining their photochemical stability also in relation to their surface chemistry and preparation method.

4.1.1. OCDs synthesis and analysis of PB characteristics

The OCDs were synthesized using a procedure outlined in a previous study conducted by the CNR-IPCF Bari group [15]. The method of CD synthesis consisted in the thermal decomposition of citric acid carried out in a high-boiling nonpolar solvent (1-octadecene, ODE) and in the presence of an amino-functionalized surface ligand (1-hexadecylamine, HDA). As highlighted in [15], by tuning reaction conditions such as temperature and time, it is possible to obtain stable carbonaceous CDs with bright and tunable fluorescence in the visible range. With this method, during thermal decomposition of the carbonaceous precursors, covalent amidic bonds are formed by thermally activated reaction between the aminic head groups of HDA and carboxylic functionalities of citric acid. This results in the formation of CDs whose surface contains nonpolar alkyl chains and that are hence dispersible in weakly polar organic solvents, such as chloroform or tetrahydrofuran (THF).

Following the procedures reported in [15], adjusting the temperature to 200°C and regulating the amount of HDA in the reaction solution to the appropriate quantity, it was possible to reproduce the synthesis of OCDs exhibiting a double emission band in the visible. More specifically, the absorption and emission optical features of the obtained OCDs are shown in Figure 4.1a.
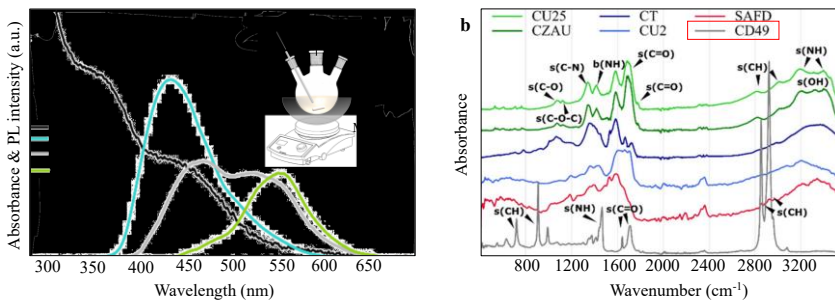
Figure 4.1: (a) UV-Vis absorption and PL spectra (λ_{exc} of 350, 410, 450 nm) of OCDs, the inset shows a schematic representation of the experimental apparatus employed for the synthesis of OCDs; (b) FT-IR absorption spectra of CDs examined in [1] (OCDs are labeled as CD49 sample).

The absorption spectrum of the OCDs consists in an intense signal that extends in the UV range up to λ<300 nm, while in the visible range, two bands are observable, peaked at 360 and 450 nm. On the other hand, the emission spectrum of the OCDs overall consists of two PL bands centered at 435 and at 575 nm. The relative

intensities of these two bands change considerably upon variation of λ_{exc}. In particular, the blue band at 435 nm results more intense for excitation <400 nm, while the yellow band at 575 nm is more prominent for longer excitation wavelengths. Moreover, the spectral position of the maximum of the blue band results excitation-dependent, exhibiting a small progressive redshift with increasing λ_{exc}. For proper excitation wavelength in the blue, a white emission can be obtained for both OCD in solution and incorporated in PMMA as free-standing films [15].

Absorption and emission features such as (i) strong absorption below 300 nm, (ii) absorption band around 360 nm and (iii) excitation-dependent blue emission band are very common optical features of CDs synthesized using citric acid and eventually amines as carbonaceous precursors [3,16–18]. Such spectroscopic characteristics are associated with radiative mechanism occurring at the surface state levels of the nanoparticles, or to the fluorescence of molecular fluorophores that form after thermal decomposition of CA and eventually reaction with amines. More specifically, noteworthy fluorophores that have been identified to form in these reactions are citrazinic acid and IPCA. On the other hand, the yellow band, considered its excitation-independent behavior and its instability for higher reaction temperatures [15], is attributed to different molecular fluorophores, or possibly to aggregates of these fluorophores, that cannot withstand higher temperatures (>200°C).

The optical features of the OCDs thus appear fundamentally sharing the same origin to those of hydrophilic CDs synthesized from similar precursors. However, it is worth remarking that the OCDs have a notably different surface chemistry. This is particularly evident in the FT-IR spectra shown in Figure 4.1b. In these spectra, the OCDs (labeled with the code CD49), compared to all other hydrophilic CDs investigated in the work, exhibit highly intense and sharp peaks in the regions at 600-1000 cm^{-1} and at 2800-3000 cm^{-1}. These peaks correspond to stretching vibrations of aliphatic C-H bonds and can be attributed to the hydrophobic surface shell of the OCDs. In particular, the lipophilic surface should be composed by long alkyl chains deriving from the ligand molecule (HDA) employed during the synthesis, or eventually also to residual ODE molecules that remain entangled within such surface nonpolar chains [15].

Whitin the scope of the work, the photobleaching resistance of OCDs as well as that of other hydrophilic CDs was assessed in solution employing pulsed-laser techniques. These techniques are described in detail in Sec. 2.3.2.

As a representative example of the spectroscopic data obtained from one of such PB experiments, Figure 4.2 shows results of FLIP performed on the yellow band of OCDs.
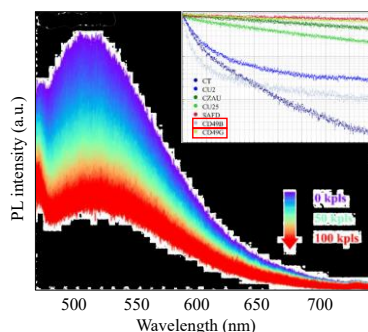
Figure 4.2: *PL spectra obtained as result of the FLIP experiment performed on OCDs yellow band (λ_{exc} = 450 nm, the same wavelength was used for the bleaching beam), from 0 (violet) to 10^5 (red) bleaching pulses; the inset shows a comparison of FLIP decay curves obtained for several CD samples in different spectral regions, where color line is representative of the emission color (the blue and yellow bands of OCDs, marked with red rectangles, are denoted respectively as CD49B and CD49G).*

In FLIP, a pulsed laser beam is used to bleach the nanoparticle dispersion sample, while PL is measured as observable variable after each bleach pulse. As shown in Figure 4.2, fluorescence is observed to be progressively dampened with increasing number of bleach pulses received by the sample. This clearly indicates the sensitivity of the emission properties of the nanoparticles to the destructive effect induced by the intense laser pulses. As testified by the trends of fluorescence intensity as a function of received bleaching pulses (inset of Figure 4.2), the degradation of optical properties in different kind of CDs was someway related to the emission colors, and the red emitting CDs resulted more stable with respect to green and blue emitting carbonaceous particles.

In particular, the FLIP decays could be fitted using, in general, multi-exponential decay model functions [1]. Specifically, the OCDs displayed a three-exponential function for the blue PL band (λ_{exc} =355 nm) and a bi-exponential function for the yellow PL band (λ_{exc} =450 nm). This reflects the complexity of the photochemical processes responsible for the observed deterioration of the optical properties. After fitting, the number of bleaching pulses needed to halve the initial PL intensity, named $N_{1/2}$, can be calculated. This parameter was used to estimate quantitatively and compare the resistance to photochemical degradation of the various CDs and their emission bands.

Interestingly, for OCDs, $N_{1/2}$ resulted of $(0.40\pm0.02) \times 10^3$ for the blue band, and $(80\pm5) \times 10^3$ for the yellow band, thus indicating a higher resistance of the yellow band compared to the blue emission. Moreover, upon comparing more carefully the FLIP decays of various CDs recorded across the overall emission spectra (inset of Figure 4.2), it becomes evident that the OCDs exhibit markedly distinct PB dynamics compared to the other analyzed CDs. This was ascribed either to the

existence of multiple fluorophores or emissive centers in OCDs, responsible for the double emission band of the OCDs, in contrast to the other CDs that display only one PL emission band (being either in the blue or in the green or in the red region according to the considered sample). Furthermore, these variations could be related to modifications in the prevalent nanoparticle PB mechanisms due to alterations in the solvent where the nanoparticles are dispersed (water for hydrophilic CDs and chloroform for OCDs).

Even more remarkably, as shown in Figure 4.3, for hydrophilic CDs, a common trend was found that related the PB resistance (quantified by $N_{1/2}$) with the average excited-state lifetime (τ, measured via TR-PL analysis at nanosecond time scale) and the non-radiative decay coefficient (k_{nr}); where k_{nr} is calculated as inverse of τ divided for $(1-\Phi_f)$, Φ_f being the experimentally measured PLQY of the considered emission. Namely, $N_{1/2}$ as a function of τ could be best fitted with a function of the type A/x^α ($\alpha \approx 2.35$), while the trend of $N_{1/2}$ as a function of k_{nr} was best fitted with a function of the type Ax^α ($\alpha \approx 1.65$). Notably, both the blue and the yellow emission of OCDs deviated from these trends. The origin of these PL bands in OCDs were attributed in part, to molecular fluorophore emission, similarly to the hydrophilic CDs. Therefore, the deviation from the empirical common trends was attributed to the different surface chemistry of the OCDs. In fact, the distinctive hydrophobic surface of the OCDs can dictate distinct pathways for the photochemical degradation. Additionally, the difference in the nanoparticle dispersing medium can also play a crucial role in the formation of ROSs, possibly working as intermediates regulating the photochemical reactions [14,19–21].
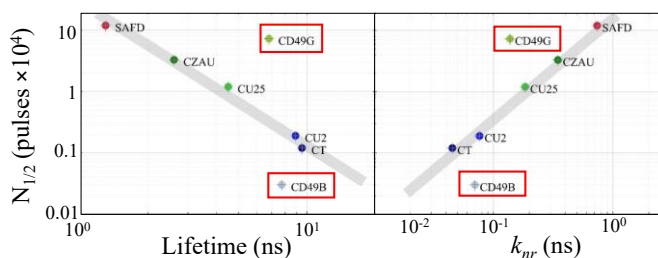
Figure 4.3: plots of $N_{1/2}$ (number of bleaching pulses needed to halve the initial fluorescence of a CD spectrum) as a function of average lifetime τ and the non-radiative decay coefficient k_{nr}, the grey lines represent the fittings of the common trends found for hydrophilic CDs, using an equation of the type A/x^α with $\alpha \approx 2.35$ (left panel) and Ax^α with $\alpha \approx 1.65$(right panel). For OCDs, FLIP decays, τ, k_{nr} and $N_{1/2}$ were examined separately for the blue (CD49B) and for the yellow (CD49G) bands tuning opportunely the excitation and emission wavelengths for their separate analysis. The sample codes referred to the OCDs are highlighted with red rectangles as a guide to the eye.

Lastly, FRAP experiments enabled achieving further very interesting information about the nature of the emission sources in the OCDs and on their photochemical degradation features. A FRAP experiment involves two distinct stages: (i) a photobleaching stage and (ii) a recovery stage. During stage (i), the nanoparticles within the solution undergo a series of bleach pulses, where the total number of the pulses is at least of the order of magnitude of $N_{1/2}$ (in the present case, 2×10^4 bleaching pulses were used for all FRAP experiments). Subsequently, in stage (ii), the bleach laser is deactivated, while the fluorescence intensity is monitored continuously over a period of time (Sec. 2.2.2).

In general, the trend of PL intensity over time observed during stage (ii) depends on the selected geometry of the experiment, namely, it changes according to if total illumination (TI) to partial illumination (PI) is selected (see Figure 2.8c-d). TI setup records the recovery over the sample volume, thus allowing to analyze if the photochemical processes induced by the bleaching stage (i) exhibit some intrinsic characteristic of reversibility [22–24]. On the other hand, in the PI setup, only a fraction of the nanoparticle dispersion is subjected to photobleaching. Therefore, in this configuration recovery of fluorescence can occur also due to diffusion of non-bleached fluorophores in the illuminated sample volume [22–24]. The combination of these two setups in the FRAP experiments proves to be very useful to the scopes of this work.

In TI configuration, none of the examined CDs displayed a PL recovery, as the PL intensity photobleached at stage (i), remained constant over time at stage (ii) [1]. This indicates that the photobleaching is irreversible and no intrinsic process (such as inverse chemical reactions possibly occurring in the employed experimental conditions) can restore their emission. On the contrary, in PI configuration, a progressive recovery of PL is revealed for all examined CDs. In absence of intrinsic recovery phenomena (excluded by the TI experiments), the PL recovery in PI configuration can be entirely attributed to the diffusion of non-photobleached fluorophores coming from the nonilluminated volume of the sample. Notably, this makes the results of FRAP experiments very interesting, since they enable us to investigate the mobile fraction of fluorophores present in the dispersion (analogously to several previously reported fluorescence spectroscopy and microscopy experiments [13,25]), thus delving into its diffusion dynamics.

Quantitative assessment of trends at stage (ii) of PI-FRAP experiments were performed after fitting the recovery trends. Details regarding such fitting procedure are provided in Sec. A4.1. After each fitting, recovery trends were evaluated from the fitted parameters M_f, representing the fraction of mobile fluorophores producing the PL recovery, and τ_d, a diffusion time that sets the timescale of the recovery.

All the investigated samples result having a M_f lower than 100% (spanning, roughly speaking, from around 15 to 40%). This indicates that CD dispersions are composed of at least two kinds of fluorophores, having the same spectroscopic characteristics but different diffusivity. In fact, in each CD sample, $1 - M_f$ of fluorophores did not contribute to the PL recovery within the timescale set by τ_d, while this fraction is expected to participate to the recovery at longer timescales.

Interestingly, the OCDs display distinct recovery responses according to whether the blue or the yellow band is examined. This result supports the attribution of the blue and yellow bands to distinct types of fluorophores. Notably, both emissions exhibit a mobile fraction of 20-30% in the investigated conditions, further testifying that at least a fraction of the emission in both bands is not produced by freely diffusing molecular fluorophores; on the contrary, larger nano-objects must be invoked to explain the diffusivity and PL recovery results.

4.2. Plasmonic resonance enhancement of CDs fluorescence by AuNPs

As evidenced in Sec. 3.1, there exists substantial promise in obtaining CDs with rationally controlled optical properties in the whole visible spectral range, through opportune choice of carbonaceous precursors and reaction parameters. Nevertheless, challenges persist in obtaining CDs with desired and highly efficient emission just operating on synthetic conditions. This is especially evident for CDs emitting within the red, as currently reported methods often result in low-efficiency emission of CDs [26–28].

In addition to optimizing reaction conditions, achieving highly efficient emission of CDs in the red region can be accomplished through post-synthetic modulation of their optical properties. Plasmonic resonance energy transfer (PRET) is a renowned photophysical phenomenon that can be harnessed to enhance or modify the emission of fluorophores [29,30]. PRET can be defined as a particular form of energy transfer, involving a plasmonic nanoparticle acting as an energy donor towards an acceptor that can be a molecule, or eventually another nanoparticle, that is situated at a right distance [31–33]. To obtain an efficient energy transfer, the plasmonic donor and the acceptor must have suitable arrangement of electronic energy levels, generally envisaged by a strong spectral overlap between the donor and acceptor absorption spectra. Moreover, to attain an effective PRET a fine tuning of the distance between the donor and acceptor pair is needed [34–37].

In the work presented in this section, the possibility of using PRET to enhance the low-efficiency red component of CD solvothermally synthesized by citric acid and urea was explored. This was achieved coupling the CDs with colloidal AuNPs, to obtain a post-synthetic modulation of CD fluorescence in solution. The work was conducted in partnership with Prof. Messina's group at the University of Palermo, in charge of the advanced spectroscopic characterization necessary to highlight the PRET interactions between AuNPs and luminescent nanoparticles. The solvothermal synthesis and post-synthetic functionalization of the CDs utilized in this work was under the responsibility of Dr. N. Mauro at Department of Biological, Chemical and Pharmaceutical Sciences and Technologies (STEBICEF) at University of Palermo. Detailed synthetic experimental procedures are reported in [2] and [38]; spectroscopic characterization data of these CDs that are of interest for this work are provided in Sec. 4.2.2. My contribution consisted in suitably synthesize AuNPs with uniform size, displaying a surface plasmon resonance (SPR) peak whose position well overlaps the CD lower-energy optical transition. A post-synthesis ligand-exchange procedure was carried out, modifying the metallic nanoparticle surface in order to induce a positive surface charge. This was in fact

a necessary requirement to electrostatically coupling the metal NPs to the negative charged CD surface, thus to avoid an electrostatic repulsion between the as synthesized AuNPs and CDs in solution. This prevents the nanoparticle from approaching at sufficient proximity, thus hindering their PRET coupling. I also contributed actively to discussions regarding the effectiveness of the nano-hybrid coupling, and the exact mechanisms underlying the interactions between the two nanoparticles, unveiling the most efficient ways to elicit an improvement of the PLQY of the CD emission in the red region.

4.2.1. Synthesis of AuNPs and post-synthetic surface modification

AuNPs were synthesized *via* a method based on reduction of $HAuCl_4$ by sodium citrate, as described in Sec. 2.1.8. The relative concentrations of sodium citrate and $HAuCl_4$ and the reaction time were opportunely chosen so that the final AuNPs had a SPR peaking at a desired spectral position (overlapping with the CDs longest-wavelength absorption band). TEM characterization of the as-prepared AuNPs is shown in Figure 4.4a.
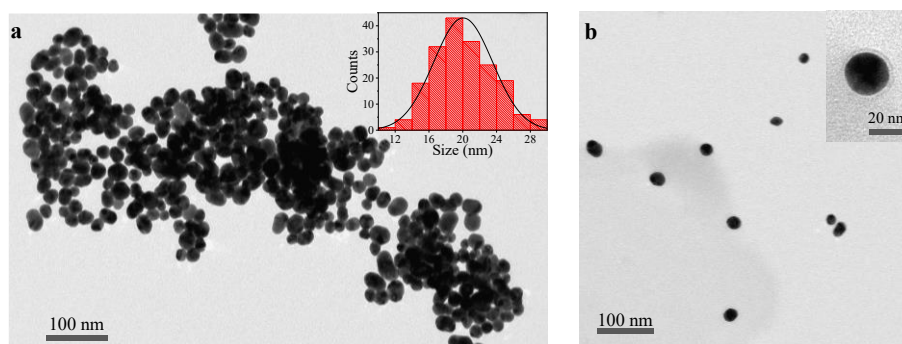
Figure 4.4: (a) TEM micrograph and size distribution (inset) of AuNPs as-obtained from the colloidal synthesis; (b) TEM micrograph of the AuNPs after functionalization with CTAB bilayer and magnification of a single nanoparticle (inset)

The as-prepared AuNPs have a mean diameter of 20±4 nm. Moreover, the ζ potential of such as-synthesized AuNPs results of -26 mV, which is ascribable to the native citrate capping layer [39].

After the synthesis, the native organic surface layer of the metal nanoparticles was modified with a post-synthetic ligand-exchange procedure [40]. This consisted in substituting the citrate capping layer with CTAB (Sec.2.1.8). Interestingly, TEM micrographs of CTAB-modified AuNPs (Figure 4.4b) displayed a shell with a low contrast surrounding the metal nanoparticles. The thickness of this surrounding layer, of approximately 2-3 nm, is consistent with theoretical predictions for a CTAB bilayer on AuNPs [41]. Therefore, also in agreement with [40], this was attributed to the formation of a compact bilayer of interdigitated CTAB molecules

at the surface of the AuNPs. Successful surface modification with CTAB chains was finally confirmed also by the ζ potential of CTAB-modified AuNPs, that results of +23 mV.

4.2.2. PRET interactions between AuNPs and CDs

The CD were solvothermally synthesized by citric acid and urea using DMF as solvent [2,38], and denoted as "SCDs" in the following. As shown in Figure 4.5a, when excited with green light at 520 nm, the SCDs exhibit a PL band at around 600 nm. However, the PLQY of this band has a low value, of around 4%.
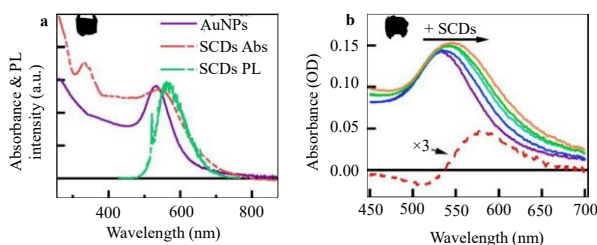
Figure 4.5: (a) absorption spectra of AuNPs, SCDs and PL spectrum (λ_{exc} = 520 nm) of SCDs; (b) absorption spectra of AuNPs (2 nM) after the addition of increasing amounts of CDs (24-130 μg/mL); the difference between pristine AuNPs spectrum and the spectrum after addition of 24 μg/mL SCDs is shown as the dotted red curve.

As can be further observed from Figure 4.5a, the SPR peak of AuNPs is centered at 528 nm and overlaps with both absorption and PL band of the SCDs. At a fundamental level, this spectroscopic overlap implies that photons involved in the plasmonic oscillations are, in a certain interval, of the same energy of the photons absorbed and emitted by the SCDs. Therefore, such overlap satisfies an essential condition for PRET interactions between AuNPs and CDs [42].

The next step was verifying if the plasmonic oscillations are subjected to the influence of the luminescent nanoparticles in their surroundings and if this can be tracked spectroscopically. Therefore, the modification in the AuNP absorption spectrum upon progressive addition of SCDs was examined (Figure 4.5b). The SPR peak is observed to undergo a measurable progressive redshift with increasing SCD added quantity. The derivative-like shape of the difference spectrum between bare AuNPs and AuNPs after first SCDs addition, unequivocally points out that the observed shift is not trivially ascribable to the sum of a spectral contribution due to the SCDs in the overall absorption spectrum. In fact, at λ<550 nm a decrease of the pristine AuNP absorbance is recorded, as testified by the negative absorbance difference. This clearly indicates that the plasmonic oscillations are influenced by a short range dipolar or electrostatic interaction with SCDs. This result is also in agreement with several previous reports indicating that plasmonic resonances of metallic NPs are very sensitive to environmental variations, such as the dielectric

constant of the media or the presence of molecules interacting at very close range [43].

After having established that the plasmonic oscillations are able to interact with SCDs, and that this interaction produces spectroscopically observable alterations, the study proceeded with exploring how this interaction impacts the optical properties of the SCDs. The distance between AuNPs and SCDs was modulated introducing a polymeric spacer (namely, a PEG2000) surrounding the surface of the luminescent nanoparticles. This procedure, also carried out by Dr. N. Mauro, was accomplished through a post-synthetic covalent bonding of the polymer to the CD surface groups, following the protocol reported in [38]. Modification of PL spectra of SCDs and polymer-functionalized SCDs (P-SCDs) in response to addition of AuNPs at increasing concentration are shown in Figure 4.6a.
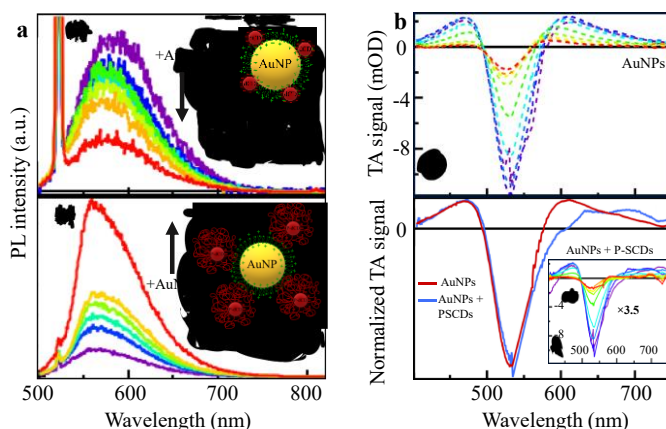
Figure 4.6: *(a) PL spectra (λ_{exc} = 520 nm) of SCDs (top) and P-SCDs (bottom) recorded upon addition of AuNPs (starting from the violet lines and progressing towards the red lines, the AuNP concentrations were 0, 10, 19.8, 39.2, 76.9, and 181.8 pM); the insets show schematic representation of interactions between SCDs and AuNP (top) and between P-SCDs and AuNPs (bottom); (b) Transient Absorption (TA) spectra of 2 nM AuNPs (top) and normalized TA spectra of 2 nM AuNPs and of 2 nM AuNPs added 0.2 µg/mL P-SCDs (bottom); the inset of (b) shows the TA spectra of the AuNPs added with P-SCDs; for both AuNPs and AuNPs + P-SCDs, the TA spectra were recorded at different delays from the pump pulse (20 nJ, 70 fs, λ = 540 nm), in particular, going from violet to red lines, the investigated delays were: 0.12, 0.3, 1, 3, 6, 10, 30, 60, 100 ps, the comparison of normalized TA spectra is shown for the 0.3 ps delay.*

For SCDs non functionalized with the surface polymer layer, the PL spectrum undergoes a progressive dampening with increasing AuNP addition. Vice versa, for P-SCDs, the addition of AuNPs produces a progressive enhancement of the PL intensity. Notably, this corresponds to an increase of the PLQY (λ_{exc} = 520 nm) from

the initial 4% to 25% for the AuNP-added P-SCDs. Remarking that, when mixed in solution, an intimate coupling by electrostatic attraction is induced between positively charged AuNPs and negatively charged SCDs, the quenching observed for the SCDs upon AuNP addition is ascribed to an electron transfer from the SCDs to the AuNPs [18,44,45]. In fact, in electron transfer, photoexcited electrons in SCDs are transferred to the metal and hence cannot participate to the emission. Moreover, electron transfer is renown to be a very short-range interaction, effective in the range of a few angstroms distance [46]. Therefore, an electron transfer mechanism is in agreement with the expected very close proximity between the nanoparticles, realized thanks to the electrostatic attraction between the opposite surface charges of AuNPs and SCDs. Conversely, as demonstrated in [2], the introduction of a polymeric spacer on the surface of the SCDs, produces a ≈2 nm thick layer around the luminescent nanoparticles. Thus, the polymer surface layer increases the distance between AuNPs and P-SCDs, thereby preventing the electron transfer to occur. Very interestingly, as highlighted by the experiment shown in Figure 4.6a, in these conditions, the nanoparticle interactions are such that an enhancement of the PL is obtained.

Therefore, the photophysical mechanisms underlying the PL enhancement observed when combining AuNPs with P-SCDs were investigated further in a femtosecond pump-probe transient absorption (TA) analysis (Figure 4.6b). The TA spectral signal of AuNPs displays a strong negative component in the region of the plasmonic peak, and positive wings at both sides of the negative peak. With increasing delay time, both negative peak and positive wings display a gradual dampening, leading the spectrum return towards its initial, non-photoexcited form.

Such signal profile and its relaxation dynamics are widely observed in metal NPs. Typically, these TA trends are elucidated envisioning that the irradiation pulse induces photoexcitation of free electrons in the metal NP, thereby generating a hot free electron gas [30,47–49]. Subsequently, rapid thermal relaxations occur, involving electron-electron scattering, electron-phonon scattering, and energy dissipation to the solvent. These relaxations are responsible for lattice temperature increase (and hence plasmonic nanoparticle local heating), as well as energy transfers to other acceptors (being molecules, nanoparticles, …) that are at sufficient close proximity to the plasmonic NP [29,30,44,45]. More specifically, the negative TA peak in correspondence of the plasmonic peak is ascribed to a "bleaching" of the LSPR excited state, while the positive wing at lower energies is sometimes ascribed to a plasmon band of "hot" electrons generated in the transient. Finally, the higher energy positive wing is frequently attributed either to higher order multiple oscillations or to interband transitions of the "hot" electrons [30,47].

To highlight possible interactions of the AuNPs with the P-SCDs, the colloidal gold dispersion employed for the TA analysis in Figure 4.6b (top) was added with a very small concentration of P-SCDs (0.2 μg/mL) and the TA measurements were repeated under the exact same experimental conditions. As demonstrated in a control experiment [2], in this concentration, the added P-SCDs are so diluted that their own TA signal is undetectable in the absence of AuNPs. On the other hand, their addition to AuNPs produces a very markedly observable alteration of the TA signal, as shown in Figure 4.6b (bottom).

The most evident modification of the AuNP TA signal occurring upon addition of P-SCDs consists in an overall dampening of the intensity of the whole spectrum at the first examined delay time (70 fs), as shown in the inset of Figure 4.6b (bottom). In particular, P-SCD-added AuNPs exhibit an intensity about 3.5 times lower than that of the bare AuNPs. Furthermore, P-SCD addition produces a modification of the TA spectral profile in the lower energy region (at around 600 nm), as is highlighted from the comparison of the normalized AuNP and AuNP + P-SCD spectra. This difference can be attributed to an extra negative component that is observable only upon introduction of the luminescent nanoparticles. Recalling that P-SCDs alone do not produce any observable TA signal in the employed diluted concentrations, the additional negative component at around 600 nm can be reasonably ascribed to the fluorescence of the P-SCDs: more properly this additional band should be designated as a negative stimulated emission TA band. This emissive contribution is only observable for the P-SCDs in the presence of AuNPs.

The intensity reduction of the plasmonic TA spectrum at 70 fs and the appearance of a negative component in the region of the emission of the P-SCDs are the fingerprints of a PRET interaction between AuNPs to the P-SCDs. In fact, these data demonstrate clearly that, when P-SCDs are added, part of the energy of the plasmonic oscillations is transferred to the P-SCDs within a timescale shorter than 70 fs. This also produces an enhancement of their emission, which is then detectable in their characteristic spectral region (around 600 nm). As found here, PRET is found to occur within an extremely short time scale. This can be considered to make the rapid energy transfer particularly effective, as the characteristic decoherence (or "thermal relaxation") of the plasmonic oscillation occurs over a longer time than the energy transfer to the luminescent CDs.

Appendix

A4.1 Fitting and detailed results of PI-FRAP experiments

Recovery trends of PI-FRAP experiments, such intensity during the recovery stage was fitted using as a model the function [25]

$$I(t) = M_f(1 - \exp(-t/\tau_d)) \, V_{corr} \qquad (A4.1)$$

where $I(t)$ is the PL intensity measured at time t, M_f is the mobile fraction of fluorophores, τ_d is diffusion time, and V_{corr} is given by:

$$V_{corr} = 1 - \frac{V_{PB}}{V} \qquad (A4.2)$$

where V_{PB} is the illuminated sample volume and V is the total sample volume. The fitting parameters M_f and τ_d obtained for OCDs and other examined CDs are reported in Table A4.1.

Table A4.1*: M_f and τ_d obtained as results of PI-FRAP experiments on the different CDs analyzed in [1] and for the PL intensity recovery probed exciting at the indicated wavelengths ($\lambda_{exc,probe}$)*

Sample	$\lambda_{exc,probe}$ (nm)	M_f (%)	τ_D (h)
CT	340	37±2	4.1
CU2	350	37±7	3.4
CZAU	410	38±9	2.8
CU25	410	19±7	2.6
CD49B	370	17±7	0.7
CD49G	450	33±6	1.8

References

[1] A. Terracina, A. Armano, M. Meloni, A. Panniello, G. Minervini, A. Madonia, M. Cannas, M. Striccoli, L. Malfatti, F. Messina, ACS Appl. Mater. Interfaces 14 (2022) 36038–36051.

[2] A. Sciortino, A. Panniello, G. Minervini, N. Mauro, G. Giammona, G. Buscarino, M. Cannas, M. Striccoli, F. Messina, Materials Research Bulletin 149 (2022) 111746.

[3] M.G. Giordano, G. Seganti, M. Bartoli, A. Tagliaferro, Molecules 28 (2023) 2772.

[4] E.A. Stepanidenko, I.A. Arefina, P.D. Khavlyuk, A. Dubavik, K.V. Bogdanov, D.P. Bondarenko, S.A. Cherevkov, E.V. Kundelev, A.V. Fedorov, A.V. Baranov, V.G. Maslov, E.V. Ushakova, A.L. Rogach, Nanoscale 12 (2020) 602–609.

[5] L. Đorđević, F. Arcudi, M. Cacioppo, M. Prato, Nat. Nanotechnol. 17 (2022) 112–130.

[6] C.M. Carbonaro, R. Corpino, M. Salis, F. Mocci, S.V. Thakkar, C. Olla, P.C. Ricci, C 5 (2019) 60.

[7] M. Meloni, L. Stagi, D. Sanna, S. Garroni, L. Calvillo, A. Terracina, M. Cannas, F. Messina, C.M. Carbonaro, P. Innocenzi, L. Malfatti, Nanomaterials 12 (2022) 2351.

[8] A. Cappai, C. Melis, L. Stagi, P.C. Ricci, F. Mocci, C.M. Carbonaro, J. Phys. Chem. C 125 (2021) 4836–4845.

[9] F. Mocci, L. de Villiers Engelbrecht, C. Olla, A. Cappai, M.F. Casula, C. Melis, L. Stagi, A. Laaksonen, C.M. Carbonaro, Chem. Rev. 122 (2022) 13709–13799.

[10] B. Han, X. Hu, X. Zhang, X. Huang, M. An, X. Chen, D. Zhao, J. Li, RSC Adv. 12 (2022) 11640–11648.

[11] F. Ehrat, S. Bhattacharyya, J. Schneider, A. Löf, R. Wyrwich, A.L. Rogach, J.K. Stolarczyk, A.S. Urban, J. Feldmann, Nano Lett. 17 (2017) 7710–7716.

[12] S. Yadav, K. Shakya, A. Gupta, D. Singh, A.R. Chandran, A. Varayil Aanappalli, K. Goyal, N. Rani, K. Saini, Environ Sci Pollut Res 30 (2023) 71912–71932.

[13] A.V. Longo, A. Sciortino, M. Cannas, F. Messina, Phys. Chem. Chem. Phys. 22 (2020) 13398–13407.

[14] A.P. Demchenko, Methods Appl. Fluoresc. 8 (2020) 022001.

[15] A. Panniello, A.E. Di Mauro, E. Fanizza, N. Depalo, A. Agostiano, M.L. Curri, M. Striccoli, J. Phys. Chem. C 122 (2018) 839–849.

[16] A. Sharma, T. Gadly, S. Neogy, S.K. Ghosh, M. Kumbhakar, J. Phys. Chem. Lett. 8 (2017) 1044–1052.

[17] A. Sharma, J. Das, Journal of Nanobiotechnology 17 (2019) 92.

[18] A. Sciortino, A. Cannizzo, F. Messina, C 4 (2018) 67.

[19] A. Ancona, B. Dumontel, N. Garino, B. Demarco, D. Chatzitheodoridou, W. Fazzini, H. Engelke, V. Cauda, Nanomaterials 8 (2018) 143.

[20] T. Mai, J.Z. Hilt, J Nanopart Res 19 (2017) 253.

[21] T. Wen, J. Liu, W. He, A. Yang, in: H. Xu, N. Gu (Eds.), Nanotechnology in Regenerative Medicine and Drug Delivery Therapy, Springer, Singapore, 2020, pp. 361–387.

[22]   N. Lorén, J. Hagman, J.K. Jonasson, H. Deschout, D. Bernin, F. Cella-Zanacchi, A. Diaspro, J.G. McNally, M. Ameloot, N. Smisdom, M. Nydén, A.-M. Hermansson, M. Rudemo, K. Braeckmans, Quarterly Reviews of Biophysics 48 (2015) 323–387.

[23]   K. Hashlamoun, Z. Abusara, A. Ramírez-Torres, A. Grillo, W. Herzog, S. Federico, Biomech Model Mechanobiol 19 (2020) 2397–2412.

[24]   J.C. Dallon, C. Leduc, C.P. Grant, E.J. Evans, S. Etienne-Manneville, S. Portet, PLOS Computational Biology 18 (2022) e1010573.

[25]   H.C. Ishikawa-Ankerhold, R. Ankerhold, G.P.C. Drummen, Molecules 17 (2012) 4047–4132.

[26]   Y. Cheng, G. Yu, Molecules 28 (2023) 7473.

[27]   M.M. Hussain, W.U. Khan, F. Ahmed, Y. Wei, H. Xiong, Chemical Engineering Journal 465 (2023) 143010.

[28]   D. Benner, P. Yadav, D. Bhatia, Nanoscale Adv. 5 (2023) 4337–4353.

[29]   H. Tang, C.-J. Chen, Z. Huang, J. Bright, G. Meng, R.-S. Liu, N. Wu, The Journal of Chemical Physics 152 (2020) 220901.

[30]   X. You, S. Ramakrishna, T. Seideman, The Journal of Chemical Physics 149 (2018) 174304.

[31]   P. Mandal, Plasmonics 17 (2022) 1247–1267.

[32]   S. ping, J Opt (2023).

[33]   D. Chi, S. Lu, R. Xu, K. Liu, D. Cao, L. Wen, Y. Mi, Z. Wang, Y. Lei, S. Qu, Z. Wang, Nanoscale 7 (2015) 15251–15257.

[34]   K. Li, N.J. Hogan, M.J. Kale, N.J. Halas, P. Nordlander, P. Christopher, Nano Lett. 17 (2017) 3710–3717.

[35]   S.P. Eliseev, N.S. Kurochkin, S.S. Vergeles, V.V. Sychev, D.A. Chubich, P. Argyrakis, D.A. Kolymagin, A.G. Vitukhnovskii, Jetp Lett. 105 (2017) 577–581.

[36]   Y. Luo, E.D. Ahmadi, K. Shayan, Y. Ma, K.S. Mistry, C. Zhang, J. Hone, J.L. Blackburn, S. Strauf, Nat Commun 8 (2017) 1413.

[37]   B. Nikoobakht, C. Burda, M. Braun, M. Hun, M.A. El-Sayed, Photochemistry and Photobiology 75 (2002) 591–597.

[38]   C. Scialabba, A. Sciortino, F. Messina, G. Buscarino, M. Cannas, G. Roscigno, G. Condorelli, G. Cavallaro, G. Giammona, N. Mauro, ACS Appl. Mater. Interfaces 11 (2019) 19854–19866.

[39]   M. Wuithschick, A. Birnbaum, S. Witte, M. Sztucki, U. Vainio, N. Pinna, K. Rademann, F. Emmerling, R. Kraehnert, J. Polte, ACS Nano 9 (2015) 7052–7071.

[40]   J. Lim, N.-E. Lee, E. Lee, S. Yoon, Bulletin of the Korean Chemical Society 35 (2014) 2567–2569.

[41]   J. PAN, H.Z. HU, (2017).

[42]   J. Li, S.K. Cushing, F. Meng, T.R. Senty, A.D. Bristow, N. Wu, Nature Photon 9 (2015) 601–607.

[43]   A. Derkachova, K. Kolwas, I. Demchenko, Plasmonics 11 (2016) 941–951.

[44]   A. Madonia, M. Martin-Sabi, A. Sciortino, S. Agnello, M. Cannas, S. Ammar, F. Messina, D. Schaming, J. Phys. Chem. Lett. 11 (2020) 4379–4384.

[45]   N. Pan, P.A. Okonjo, P. Wang, Y. Tang, Y.-P. Sun, L. Yang, Chemical Physics Letters 743 (2020) 137208.

[46]   H.L. Tavernier, M.D. Fayer, J. Phys. Chem. B 104 (2000) 11541–11550.

[47]   T.S. Ahmadi, S.L. Logunov, M.A. El-Sayed, J. Phys. Chem. 100 (1996) 8053–8056.

[48]   M.L. Brongersma, N.J. Halas, P. Nordlander, Nature Nanotech 10 (2015) 25–34.

[49]   Y. Zhang, S. He, W. Guo, Y. Hu, J. Huang, J.R. Mulcahy, W.D. Wei, Chem. Rev. 118 (2018) 2927–2954.

5

Light Emitting Applications

"The advance of technology is based on making it fit in so that you don't really even notice it, so it's part of everyday life."

Bill Gates

Abstract

The use of CDs in lighting devices is of paramount interest, driven by a societal shift towards eco-friendly materials. Despite promising developments since initial experiments in 2010s, challenges persist, including the need for reproducible synthetic strategies of full-visible-spectrum emitting CDs, resistance to aging effects and retaining high PL also in solid-state devices. Chapter 3 provides basic characterization of synthesized CDs, including analysis of their photochemical resistance. Focusing on two most promising types of CDs, namely DCDs and NR-CDs, this chapter demonstrates their potential impact on optoelectronics or photonics, based on key properties such as resistance to aggregation-induce quenching (AIQ) and/or molecular-lasing action. Additionally, the double green/red emission of DCDs is harnessed to fabricate white color-converting polymeric layers with finely modulated colorimetric properties, optimized combining numerical and experimental strategies. Consequently, this chapter also contributes to advance both theoretical and operational knowledge of CD solution-based processing for their implementation in lighting devices. Findings outlined in this chapter have been object of publications in G. Minervini et al., Nanomaterials 2022 [1] and G. Minervini et al., ACS Nano 2023 [2].

5.1. Fabrication of DCD polymeric nanocomposites: numerical and experimental evaluation for implementation in white LEDs

The solvothermally synthesized PEI-passivated DCDs are characterized by a double broad emission band in the visible, namely in the green and in the red spectral region (Sec. 3.1). Such feature, especially the high intensity of the red component of DCD fluorescence compared to that of other solvothermally synthesized CDs [3–8], makes these materials particularly attractive for implementation in white emitting LEDs (WLEDs). As described in Sec. 1.3.1, WLEDs based on a single emitting semiconductor chip necessitate of color-converting component to achieve a final white light spectrum. Thanks to all their outstanding properties, CDs have been recently thoroughly examined to act as optical fluorescent color converters in these application areas, substituting harmful or expensive currently used materials [9–11]. However, solvothermally synthesized CDs most frequently lack of a sufficiently intense red component in emission spectrum, limiting the achievable emission to cool white gamut and resulting in low chromatic rendering index (CRI) [12,13]. Moreover, other issues related to insufficient PLQY and AIQ of PL can be encountered, further hindering the efficient use of CDs in these devices [14–17]. As discussed in Sec. 3.1.1, DCDs have an emission spectrum with green and red components of equal intensity. Moreover, the presence of passivating polymer (i.e. PEI) on their surface may prevent strong AIQ.

In this section, we investigate the fabrication of polymer nanocomposites embedding DCDs and we explore their application as color converting layers. In addition, we devise a numerical calculation method facilitating the evaluation of colorimetric parameters such as CIE 1931 chromaticity coordinates, correlated color temperature (CCT), and CRI starting from experimentally collected or simulated spectral data. This notably advances our capabilities of (i) making previsions of colorimetric characteristics achievable by our nanocomposites and (ii) assessing directly their measured spectral properties in terms of colorimetric variables, that are those genuinely relevant to the final application. This work establishes experimental procedures for nanocomposite fabrication and data-elaboration strategies easily transferable to other CDs or in general, luminescent materials, with different spectroscopic properties. Therefore, the present study result in advances that may facilitate the introduction of innovative and more sustainable materials in these optoelectronic devices.

5.1.1. Preparation of DCD nanocomposite films

DCDs nanocomposites were prepared by embedding the CDs in a transparent polymeric matrix of PVA. The nanocomposite fabrication procedure is described schematically in Figure 5.1 (see Sec. A5.1 for further experimental details): the purified DCD powders were firstly used to obtain solid-state emitting fluorophores, in a matrix of PVP. This procedure was necessary to both ensure high durability of the powder fluorophores and limit problems related to the hygroscopicity of the bare purified DCD powders. The as obtained DCD powder fluorophores were mixed with PVA in an aqueous solution, thereby obtaining liquid "inks" that were filmed on a quartz substrate (1 cm×1 cm). Two distinct deposition techniques, namely spin-coating ad drop casting, were tested to obtain nanocomposite coatings with different thickness
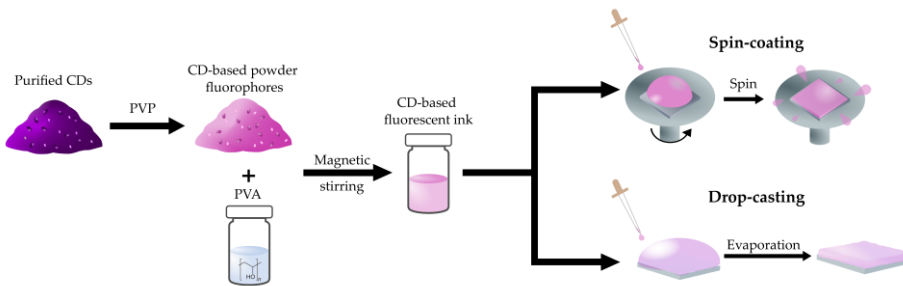
Figure 5.1: *Graphical description of the fabrication steps involved in the preparation of DCD nanocomposite films [1].*

As it will be better described in the following sections, both the concentration of DCDs in the nanocomposites and the film thickness are important parameters in determining the fraction of incident blue light of the InGaN LED (465nm) that is converted into PL, and therefore, the operative behavior of the nanocomposites as color-converters. Overall, within this preparative approach it was possible to modify both final concentration of DCDs in the nanocomposite and film thickness by operating on parameters concerning either the preparation of the ink (e.g. the concentrations of PVA and of DCD powder fluorophores in the ink) or deposition parameters (e.g. spin-coating speeds, deposited volumes, …).

Notoriously, drop casting and spin-coating are two deposition techniques able to produce polymeric films with markedly different thicknesses [18]. Namely, spin-coated polymeric films have thickness of few μm. Conversely, the thickness of drop cast coatings can be varied significantly depending on factors such as concentration of the polymer solution, solvent, and evaporation time, potentially reaching hundreds μm thickness ranges [19,20]. In the present work, we have employed both deposition techniques to enable the modulation of film thickness over a wide interval (Sec. 5.1.2). Both ink formulation conditions (DCD

fluorophore and PVA concentrations) and deposition variables were initially set up to obtain macroscopically homogeneous nanocomposite coatings, that covered entirely the surface of the substrate. Then, such parameters were modulated in order to obtain films with diverse thickness. Moreover, in our preparative approach, the final loading of DCDs in the nanocomposite can be easily modified, varying the initial concentration of powder fluorophores in the ink. In Table 5.1 is reported the list of the prepared solid-state films with the main deposition parameters, where the drop cast samples are indicated by the acronym DC and the spin coated ones by SC. Diverse film thicknesses and CD concentrations in the nanocomposites are expected to have a high modulability in their absorption and fluorescence properties, and hence ultimately in their color-converting capabilities.

Table 5.1: *drop cast (DC-) and spin-coated (SC-) nanocomposites and deposition parameters [1].*

Sample	CD-based fluorophore concentration (mg/mL)	PVA Concentration (g/mL)	Drop cast ink volume (µL)	Spin speed (rpm)
DC-A	100	0.4	100	/
DC-B	50	0.4	100	/
DC-C	50	0.2	50	/
DC-D	2	0.2	50	/
DC-E	1	0.4	50	/
SC-A	100	0.4	/	1000
SC-B1	50	0.4	/	1000
SC-B2	50	0.4	/	800

5.1.2. Characterization of nanocomposite films

An in-plane and cross-section SEM analysis of the films was carried out to investigate microscopic morphological features and measure their thickness (Figure 5.2).
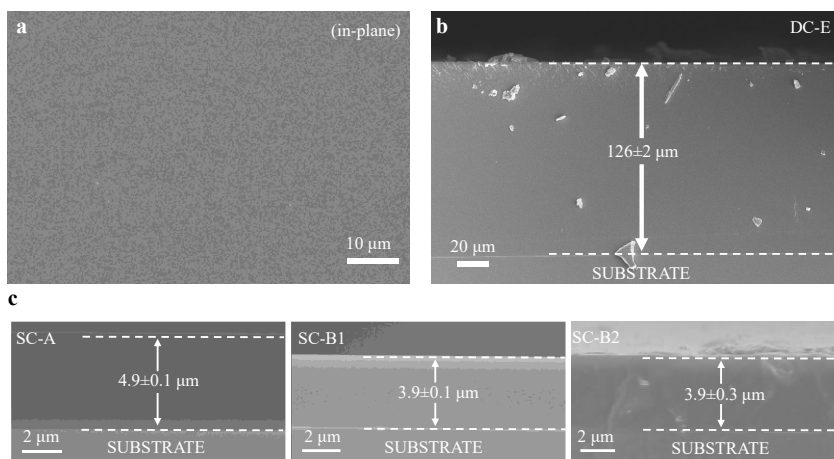
Figure 5.2: (a) representative in-plane SEM micrograph (sample DC-E); cross-section SEM micrographs of nanocomposites (b) DC-E and (c) SC-A (left), SC-B1 (center) and SC-B2 (right) [1].

The in-plane micrographs of the films (Figure 5.2a) show that the coatings have a uniform surface on the microscopic scale. Occasionally, only very small (<<1 μm) agglomerates are observed, likely arising from residues of film deposition steps. Furthermore, the uniformity of the contrast all over the surface suggests the absence of aggregation of DCDs within the nanocomposites.

As shown in Figure 5.2b, cross-section SEM micrographs of drop cast nanocomposites revealed that the thickness of these samples is in the range of hundreds of μm. For such samples, a modulation of the overall film thickness can be easily obtained increasing the volume of deposited ink. For example, the nanocomposite DC-E (shown in Figure 5.2b), deposited with a 50 μL ink drop, had a thickness of (126±2) μm, while DC-B, deposited with a 100 μL ink drop, exhibited a thickness of (350±6) μm (further data provided in [1]). In comparison, spin-coated films display a much lower thickness, of around few μm. Specifically, SC-A (the sample with the higher concentration of DCD powder fluorophore) exhibits a thickness that is around 1 μm greater than that of SC-B1 and SC-B2, having half the DCD fluorophore concentration. This can be attributed to an increase in the ink viscosity due to the more concentrated PVP fluorescent powders in the dispersion [21]. However, adjusting the spin speed proves less effective in inducing significant changes in film thickness, as results from the comparison of SC-B1 (1000 rpm) and SC-B2 (800 rpm). This might appear in contrast with most frequently reported cases, in which tuning the spin speed is a very advantageous strategy to alter the deposited coating thickness. However, the lack of modulability of film thickness observed in the present case can be

attributed to the fact that the used spin speed is too low to induce notable variations of overall thickness [22].

The optical properties of the drop cast and spin-coated nanocomposite films were characterized by UV-Vis absorption, PL and PLQY (Figure 5.3). To characterize PL and PLQY, the samples were excited at 465 nm, peak wavelength of the blue LED chip used in color conversion experiments (Sec. 5.1.4).
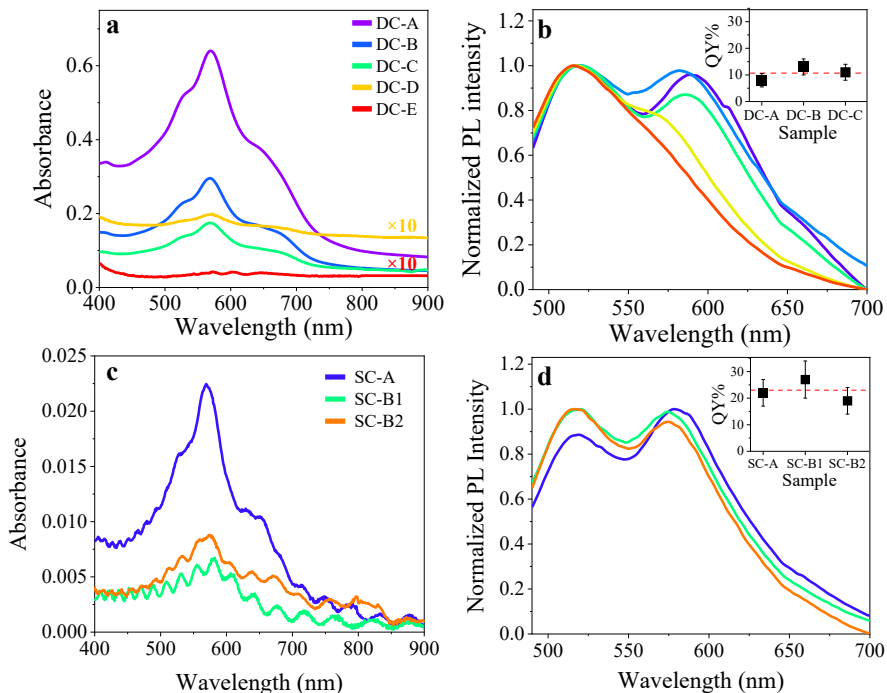
Figure 5.3: *UV-Vis absorption and normalized PL (λ_{exc} = 465 nm) spectra of (a, b) drop casted and (c, d) spin-coated DCD nanocomposites; the inset of (b, d) reports the PLQYs (λ_{exc} = 465 nm) of the nanocomposite samples; the dashed red line is a guide to the eye, and it is traced in correspondence of the weighted average of the PLQYs (where weights are the experimental errors) [1]*

From these spectra it is possible to observe that the DCDs embedded in the PVA nanocomposites have spectral features similar to those observed for the DCDs dispersed in aqueous solution (Figure 3.1d,e). However, the absorption maximum results shifted at 570 nm, while it was observed at 550 nm in the DCD solution; moreover, both absorption and emission features appear broader in the nanocomposites.

These spectral differences can be ascribed to effects of the different local chemical environment of the DCDs, changing from the solution to the polymer matrix.

Specifically, in the nanocomposites, the DCDs are expected to interact with pendant –OH and pyrrolidone moieties of PVP and PVA respectively.

Moreover, a scattering component is noticed in all drop cast samples. This is likely ascribable to surface roughness of the drop cast films, less likely to formation of aggregates of DCDs that however are not observed in microscopic analysis of the nanocomposites by SEM (Figure 5.2a).

From the absorption spectra of the drop cast films (Figure 5.3a) it is possible to observe that changing the preparation parameters allow to obtain nanocomposites with very variable optical extinction of incident radiation. This is particularly true for samples DC-A, DC-B and DC-C, that also exhibit a PL spectrum with green and red components of equal intensity, and a PLQY of around 10% (Figure 5.3b). On the other hand, samples DC-D and DC-E show a very low absorbance, and a lower red emission band. Moreover, a reliable PLQY could not be measured for these samples, since their very low absorbance resulted comparable to the scattering losses.

This leads to the conclusion that the drop casting deposition method is not very suitable to fabricate films with an optical absorbance lower than a certain level, for example lower than ~0.1. However, nanocomposites with this absorbance, still retaining efficient double-band emission can be fabricated with the spin-coating deposition, due to the renowned capability of this technique of obtaining thinner thickness and very flat surfaces, compared to the drop casting method.

The flatness of the spin-coated nanocomposite surface is corroborated by their absorption spectra (Figure 5.3c) that show typical thin film interference fringes. In fact, interference is only possible within a very smooth film and plane surface, while the presence of submicrometric surface features would cause incoherent diffuse scattering rather than coherent light wave superposition [23–25]. As shown in [1], from the spectral positions of the fringes maxima or minima in the transparency region (800-900 nm) and assuming for the nanocomposite the refractive index of PVA (n = 1.48), it becomes possible to independently estimate the thickness of these nanocomposites; the as-estimated thicknesses resulting in agreement with those measured directly by cross-section SEM micrographs (Figure 5.2c).

The PLQY of spin-coated nanocomposites (inset of Figure 5.3d) ranges between 20 and 25% with minor variations among the samples, higher than those of the drop cast films, resulting in efficiencies about twice as high. This may be ascribed to re-absorption of both green and red emitted photons in drop cast samples. In fact, in these samples, the emission bands spectrally overlap with the very intense absorption bands at 570 nm and at around 650 nm respectively. In thinner and less-absorbing spin-coated samples, a decrease of such self-absorption explains

the increase of the measured PLQY. However, a minor self-absorption, especially of green PL band is still observed in sample SC-A. In fact, SC-A exhibits a relatively weaker green than red band. This can be explained with the absorption band at 570 nm being almost 4 times more intense in SC-A than in SC-B1 and SC-B2. However, such potentially harmful self-absorption does not significantly impact the overall PLQY of the spin-coated nanocomposite and hence can be regarded as a minor effect.

5.1.3. Numerical simulations for the design of DCD nanocomposites

We set up a numerical calculation procedure to estimate in advance possible colorimetric properties of DCD-based nanocomposites, considering as input data the spectral information regarding the fluorophores and the excitation light source. In general, the resulting final spectrum can be characterized as the combination of a green/red component (representing the PL spectrum of DCDs) and a blue component (originating from the external LED chip). We can model the final relative spectral density of irradiance ($\phi(\lambda)$) as:

$$\phi(\lambda) = f \cdot \phi^{GR}(\lambda) + (1-f) \cdot \phi^{B}(\lambda) \tag{5.1}$$

where ϕ^{GR} and ϕ^{B} are the relative spectral densities of irradiance of the green/red and blue component respectively, and f is:

$$f = \frac{A^{GR}}{A^{GR} + A^{B}} \tag{5.2}$$

where A^{GR} and A^{B} are the integrated areas associated respectively to PL of DCDs (green/red component), and to the blue LED source in the final spectrum. In such final spectrum, the green/red component represents the color-converted light, while the blue light represents the residual light of the irradiation source. Therefore, f represents the fraction of color-converted light in the overall spectrum. All mathematical steps involved in the obtainment of these equations and more rigorous definitions of these quantities are reported in Sec. A5.2.

In a realistic situation, the fraction f of color-converted light will be dependent on several factors, including: (i) optical properties of the fluorophores (e.g. their absorption coefficient at the LED wavelength, PLQY, ...) (ii) concentration of fluorophores and thickness of color-converting film and (iii) the geometrical conditions of the experiment where the color-converting layer is analyzed (e.g. divergence of incident and emitted light beams, irradiation and collection angles, ...) [26–29].

Considering a hypothetical simplified geometry in which incident light has no divergence (is a perfectly collimated beam), resulting light is collected across a 360° angle, and reflection and scattering at the nanocomposite surface can be

neglected, f will depend only on the nanocomposite material properties. Albeit this case is very simplified, it is instructive to discuss what is the form that f assumes in this case. Such f considered in these conditions is named f_m:

$$f_m = \frac{c}{c+1} \tag{5.3}$$

where c is:

$$c = PLQY(e^{\alpha_B d} - 1) \tag{5.4}$$

expressing the properties of the nanocomposites involved in the color-conversion process, namely its PLQY, its absorption coefficient at the excitation source wavelength (α_B) and the film thickness (d) (see Sec. A5.2 for further mathematical details and derivation of equations). Since α_B is proportional to the concentration of DCDs in the nanocomposites [22], (5.3) and (5.4) clearly show how the color converting properties of the nanocomposite can be changed according to the optical properties of color-converting fluorophores and to parameters determinable with its fabrication strategy (e.g. the film thickness). However, in real cases, f will be also dependent on a factor g, accounting for experimental geometry considerations, and hence it will take a form of the type:

$$f = g \cdot f_m \tag{5.5}$$

In particular, colorimetric properties are known to be dependent on the measuring geometry [26], due to angular dependencies of the spectrum generated from the sample surface (also called color stimulus). However, *a priori* mathematical description of g is very complicated, as it necessitates the exact knowledge of several factors such as irradiation and collection angles, irradiated area, angles of divergence of the blue diffused and PL emitted light, acceptance angle and position of detector [26,27,30–33]. Nonetheless, for a fixed experimental geometry (fixed g), f will be only dependent by f_m, i.e. from the employed fluorophores and by variables employed for the fabrication of the color-converting film, determining its thickness and absorption coefficient.

Therefore, since herein we work at fixed experimental geometry, variations of f can be directly related to the constructive characteristics of the nanocomposite films, namely to PLQY, α_B and d.

For a $\phi(\lambda)$ with a given f, the colorimetric properties, namely: 1931 CIE chromaticity coordinates, CCT and CRI can be calculated following the relevant guidelines of CIE [30]. Therefore, taking f as variable, we can simulate several $\phi(\lambda)$ and then use these results to obtain simulated colorimetric properties of nanocomposites. In particular, letting f vary between 0 and 1, we obtain all possible combinations between the blue spectrum of the excitation LED source

and the green/red spectrum of the DCDs. Among these, we can reasonably expect colorimetric properties corresponding to the white light to be achieved for intermediate values of f. On the contrary, at extremum values of f, either the blue spectrum or the green/red spectrum will be dominant, preventing the achievement of the white light.

To be more quantitative, we can set as goal the achievement by the combined spectrum (simulated $\phi(\lambda)$) with colorimetric properties of a standard illuminant. Then, we can quantitatively assess how distant the simulated colorimetric properties are from those of the standard illuminant. Specifically, in the present work, CIE D65 was selected as the reference, following CIE recommendations on uniformity of practice in the evaluation of whiteness of surface colors [26,30], and the 1931 CIE chromaticity coordinates of such standard illuminant were considered as goal to reach for the simulated (x, y). A large number (1000) of chromaticity coordinates were simulated, letting f vary from 0 to 1, obtaining 1000 simulated $\phi(\lambda)$ and corresponding (x, y). Then, the best achievable white coordinates ($(x, y)_{baw}$) were calculated by the spectrum as the simulated (x, y) values that minimize the distance with the coordinates of the reference illuminant. Thereafter, based on the calculated $(x, y)_{baw}$, also the other correspondent minimum-distance color parameters: f_{baw}, CCT_{baw} and CRI_{baw} were identified.

Simulated spectra and a 1931 CIE diagram reporting the simulated (x, y) with varying f are shown in Figure 5.4. For the reported calculation, $\phi^B(\lambda)$ is measured recording a blank LED chip spectrum, using a bare polymer without embedded DCDs as blank sample (see Sec. 5.1.4 for details on experimental configuration). The emission of DCDs ($\phi^{GR}(\lambda)$) is simulated using the PL spectrum of DCDs at λ_{exc} = 465 nm (Figure 3.1e).
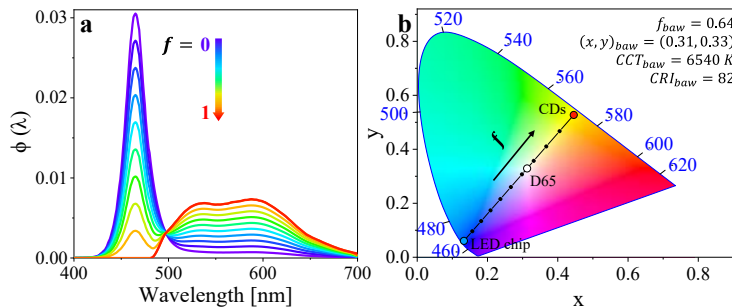
Figure 5.4: (a) simulated $\phi(\lambda)$ obtained combining $\phi^B(\lambda)$ and $\phi^{GR}(\lambda)$ with variable f, according to (5.1); (b) 1931 CIE diagram showing the chromaticity coordinates corresponding to simulated $\phi(\lambda)$ in (a) (black dots), $\phi^B(\lambda)$ (cyan dot), $\phi^{GR}(\lambda)$ (red dot), and D65 standard illuminant (white dot), and line plot obtained by simulating 1000 chromaticity coordinates as a function of f (for f varying between 0 and 1) [1].

The resulting $(x, y)_{baw}$ are very close to those of the standard D65 illuminant, that are (0.31272, 0.32903). Also the CCT_{baw} of 6540 K is very close to that of the reference, that is around 6500 K [26]. Moreover, the resulting CRI_{baw} is >80, that is an acceptable value for most white LED light bulbs [26]. Therefore, the simulation results indicate that, considering the employed blue LED as primary irradiation source, DCDs can effectively serve as color-converting materials, yielding good colorimetric properties of the final white light. Under a fixed experimental geometry, this is achieved once the preparative conditions of the nanocomposites are optimized, making f as close as possible to f_{baw}.

5.1.4. Experimental evaluation of colorimetric properties of DCD nanocomposites

Colorimetric properties of all the prepared nanocomposites are measured under a fixed experimental geometry, mounting the blue InGaN LED excitation source (Kingbright® Blue, peak wavelength: 465 nm) in the HORIBA Fluorolog 3 spectrofluorometer (See Sec. 2.2.4). A photograph and a schematic description of a DCD nanocomposite irradiated with the primary blue LED source are shown in the inset of Figure 5.5b. Photons recorded by the detector are converted in a spectrum of relative spectral density of irradiances ($\phi(\lambda)$) by normalizing the spectral data and expressing the intensities in absolute radiometric units (W/cm^2). From the as-obtained experimental $\phi(\lambda)$, CIE chromaticity coordinates, CCT, and CRI are calculated (Sec.5.2). The obtained measured colorimetric properties are reported in Table 5.2. The chromaticity coordinates are also plotted in a CIE 1931 diagram in Figure 5.5a.

Table A5. 1: Experimentally measured colorimetric properties (CIE chromaticity coordinates, CCT and CRI) of prepared nanocomposite films [1].

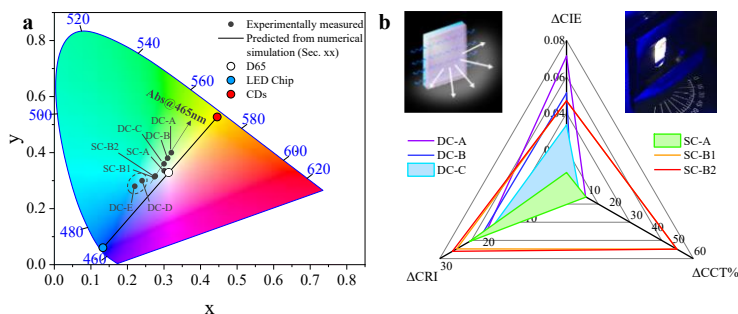| Sample	(x, y)	CCT (K)	CRI
DC-A	(0.32,0.40)	5913	81
DC-B	(0.31,0.38)	6341	80
DC-C	(0.30,0.36)	6902	82
DC-D	(0.24,0.30)	13610	63
DC-E	(0.22,0.28)	19499	59
SC-A	(0.30,0.34)	7100	77
SC-B1	(0.27,0.31)	9894	74
SC-B2	(0.27,0.31)	9894	73

Figure 5.5: (a) CIE 1931 chromaticity diagram reporting experimentally measured coordinates of DCD nanocomposites, simulated theoretical trend (Sec. 5.1.3), and chromaticity coordinates of the blue LED chip and the DCDs; (b) radar chart showing the deviation of experimentally measured CIE chromaticity coordinates, CCT (in %) and CRI for samples DC-A, DC-B, DC-C, SC-A, SC-B1 and SC-B2 (samples DC-D and DC-E are excluded since they do not have green and red bands with comparable intensity) from the colorimetric properties of D65 standard illuminant. The deviations are named ΔCIE, ΔCCT and ΔCRI, detailed procedure for their calculation is provided in Sec. A5.2); the insets of (b) show a sketch describing the irradiation in the employed experimental geometry (left) and a picture demonstrating the white color of sample SC-A under irradiation with the blue InGaN LED chip (right) [1].

The experimental chromaticity coordinates of DCD nanocomposites show a diagonal trend in the CIE 1931 diagram. In particular, the coordinates shift from bottom-left (blue/light blue hues) to top-right (yellow color produced by the green/red components of DCD emission spectrum), following the increase in absorbance at 465 nm of the nanocomposites (Figure 5.3a,c). This tendency reproduces an increase of f (fraction of converted light) in the experimentally measured $\phi(\lambda)$. However, the observed trend of the experimental chromaticity coordinates is not perfectly equal to that of the simulated points (details in Sec. 5.1.3). As explained in that section, the simulated data produce the best achievable white colorimetric properties, i.e. the properties that minimize the deviations from (x, y), CCT and CRI of the D65 standard illuminant. The experimentally measured coordinates show higher deviations that can be accounted for small differences of DCD nanocomposite emission spectra that cannot be easily considered in the simulated data (Sec. 5.1.3).

It is very interesting that the experimental data comprises both drop cast and spin-coated nanocomposites. Therefore, colorimetric properties result to be determined only by nanocomposite thickness, and DCD absorbance and emission properties, while they display no direct dependence on the employed deposition technique. This remarks how different solution-based nanocomposite preparative strategies can be employed to achieve relevant final colorimetric properties, and

therefore, the correct fabrication technique has to be selected according to the desired final necessities.

It is also worth noting that nanocomposites having the lower intensity of red component (DC-D and DC-E) result in chromaticity coordinates that are out of the trend defined by the other samples. This remarks the sensitivity of the final colorimetric properties on the optical emission of DCDs embedded in the nanocomposite. Determined selection of preparation parameters may result in alterations of the fluorophore emission spectra, provoking undesired effects on the final colorimetric properties.

Finally, from examination of colorimetric property deviations of DCD nanocomposites from D65 illuminant (Figure 5.5b), we can observe that SC-A is the sample with the minimum coordinate distance with respect to D65, having chromaticity coordinates of (0.30, 0.34). On the other hand, DC-C has the lowest ΔCCT and ΔCRI (CCT = 6902 K and CRI = 82). This result points out that, in this particular case, two samples obtained by two different deposition methods under opportune modulation of preparation parameters regulating fluorophore concentration and film thickness, yield white colorimetric properties suitable for replicating the D65 colorimetric properties. More in general, it is worth notice that , considering that most common commercial daylight LED-based light bulbs have a CCT of 6500 K or higher and CRI ~80 [26], the colorimetric features of samples fabricated herein (SC-A and DC-C are very notable examples) are feasible for implementation as color-converters in WLED devices.

5.2. NR-CDs for efficient solid state color conversion and lasing

As described in Sec. 3.1.3, NR-CDs consist of NR molecules embedded within a carbonaceous network. This enables a protection of the active fluorophores from environmental degradation, as demonstrated by PB experiments. Moreover, separation of NR molecules by carbonaceous amorphous structures may also possibly inhibit non-radiative energy transfers from fluorophore to fluorophore. Preventing aggregation induced quenching (AIQ) is interesting in the perspective of embedding high concentration of fluorophores in solid state matrices, a very frequent need in solid-state optoelectronic devices [34–36]. Notably, CDs are reported to be often affected by AIQ at the solid state [37]. Additionally, it was commonly documented that also in concentrated solution, the majority of CDs exhibit variations of their emission features, frequently involving a lowering of their quantum efficiency due to interparticle self-quenching [14,17,38].

In this section, the experimental results demonstrate that the unique structure of the NR-CDs guarantees these nanoparticles a remarkable resistance to AIQ. This opens the way to the use of these CDs in lighting devices: in particular, as an example, solid-state polymeric nanocomposites were fabricated to work as color converters in LEDs. Next, concentrated solutions of NR-CDs were exploited to achieve lasing and random lasing in solution. This is a particularly significant result, since lasing from CDs has been so far succeeded only in a very limited number of reported cases, and only few of them in the red region [39,40]. In our approach, reaching lasing activity is facilitated by the consideration that NR is a well-known, although not very efficient, laser dye [41]. However, when enclosed into the carbonaceous core, it is not automatically obvious that the NR molecule can still emit by stimulated emission. Nonetheless, using NR-CDs the PB and AIQ resistance earned from the presence of the carbonaceous matrix can be also exploited to further possibly attain improved lasing performances.

5.2.1. Fabrication of highly concentrated polymeric nanocomposites for color conversion in LEDs

The remarkable resistance of NR-CDs to AIQ is firstly demonstrated examining the fluorescence of the solid-state purified powders of the NR-CDs, compared to the powder of the bare NR dye (Figure 5.6a).
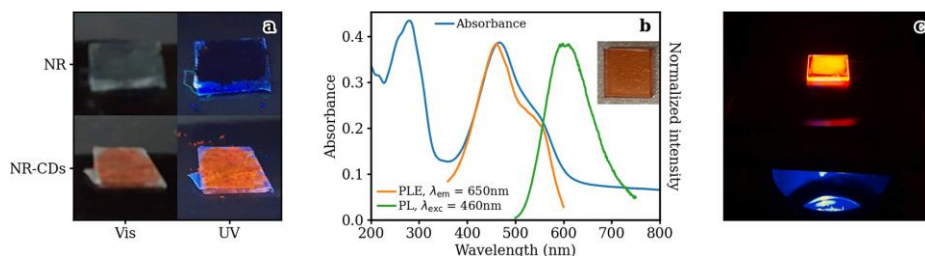
Figure 5.6: (a) Pictures of solid-state powders of NR (top) and purified NR-CDs (bottom) under visible (left) and UV (right) light; (b) UV-Vis absorption, PLE, PL spectra and picture (inset) of a PVA nanocomposite containing NR-CDs, deposited on a quartz substrate; (c) picture of NR-CDs-PVA nanocomposite drop cast on a quartz substrate upon irradiation with a commercial blue InGaN LED chip [2].

As evident, under UV light irradiation, the purified NR-CDs at solid state show a red fluorescence, in contrast to the bare NR dye powder, which undergoes complete AIQ. For molecular dyes, such as NR, AIQ at the solid state can be most often attributed to π−π stacking of the dye molecules [34], increasing nonradiative recombination pathways. On the other hand, the absence of AIQ in NR-CDs can be considered as a clear manifestation of the ability of the carbogenic matrix to prevent such π−π stacking.

Notably, the ability of NR-CDs to resist to AIQ can be exploited for the fabrication of solid-state nanocomposites in which these nanoparticles are embedded in high concentrations, still retaining their emissive properties. This can be very useful for fabricating the color-converting components of semiconductor LED devices [36,37]. As a demonstration of this, a nanocomposite incorporating NR-CDs in a PVA was formulated and deposited onto a quartz substrate. The procedures for the preparation and deposition of these nanocomposites are analogous to those described for color-converting polymer films incorporating DCDs (Sec. 5.1.1).

As can be observed from the spectroscopic characterization in Figure 5.6b, a NR-CD-PVA nanocomposite (here deposited by spin-coating procedure), still shows the nanoparticle emission band, that is centered at 600 nm; on the other hand, the absorption and PLE spectra of the nanocomposite exhibit a very large peak at 460 nm with an underlying component at around 535 nm. This profile is different from that discussed in Sec. 3.1.3 for NR-CDs in solution. Nonetheless, it is very well established that in the NR dye the absorption band at 460 nm is attributed to the excited state of NR in its neutral form [42,43]. Therefore, the appearance of this band in the NR-CDs-PVA may be attributed to an alternation of the equilibrium of the relative concentration of neutral and cationic form of NR in the nanoparticles, following the modification of the chemical surrounding upon embedding the NR-CDs in the polymer film. In this perspective, also the blue-shift of the PL maximum from 620 nm (solution) to 600 nm (PVA nanocomposite) may be interpreted as a

widening of the HOMO-LUMO gap, associated to the decrease in polarity of the chemical environment in the PVA matrix [42]. Finally, as shown in Figure 5.6c, a NR-CDs-PVA film with a thickness of a few hundred micrometers (obtained by drop casting deposition) is able to convert the blue emission of a LED source into orange light. This means that the fluorophore concentration and the film thickness are suitable to achieve a full extinction of the incident radiation, while still retaining an intense fluorescence. This capability therefore demonstrates the practical applicability of these NR-CDs to the fabrication of color-converter components of semiconductor LEDs.

Finally, to demonstrate further potentialities of the NR-CDs in photonics, their capabilities to act as active laser media was analyzed (Figure 5.7).
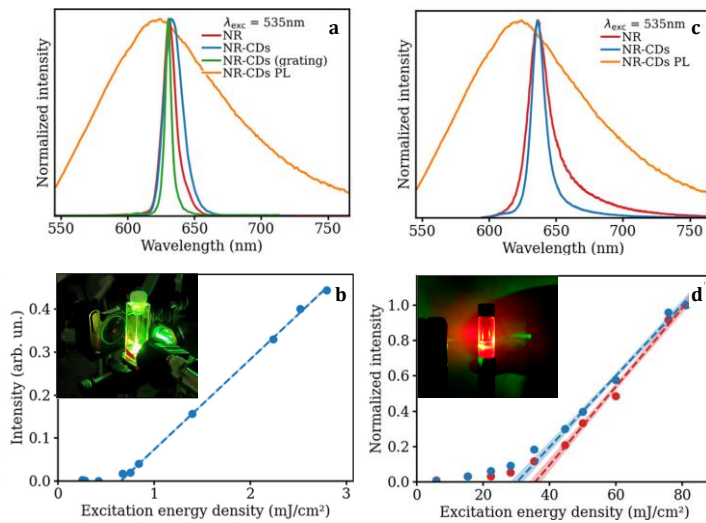

Figure 5.7: *(a) stimulated emission spectra of NR dye and NR-CDs in a Fabry Perot configuration; the green curve is obtained through the substitution of one of the mirrors of the resonant cavity with a grating; (b) output–input response curve and lasing threshold of NR-CDs; the inset shows a picture of the lasing emission from a NR-CD dispersion; (c) random lasing (RL) spectra of NR dye and NR-CDs; (d) output ¬input response curve and lasing threshold of the NR and NR-CDs; the shaded areas represent 1σ confidence intervals; in the inset a picture of red RL obtained by a medium constituted of a mixture of NR-CDs and TiO$_2$ nanoparticles is shown. For all lasing experiments, the pump is at a wavelength of 535 nm. Steady-state PL of NR-CDs are shown as a reference in stimulated emission and RL spectra [2].*

This part of the work, mainly under the responsibility of Dr. A. Terracina, Dr. A. Pramanik, Dr. A. Sciortino and Prof. F. Messina at University of Palermo, involved the homemade set-up of a Fabry-Perot (F-P) resonant cavity, hosting a quartz cuvette, externally pumped with a nanosecond tunable green laser. The

active medium consisted in a very concentrated acidified ethanol dispersion of NR-CDs, whose absorbance at 535 nm was 1.6 O.D. in an optical path of 1 mm. The AIQ resistance NR-CDs, preventing π–π stacking of fluorophores upon concentration increase, was therefore key to attaining a positive gain in the lasing action. A picture of the experimental apparatus is shown in the inset of Figure 5.7b. In this photo, a red spot is observable on the cavity mirror at the back of the picture, testifying the presence of lasing in the red region in the macroscopic resonator. The stimulated emission spectrum of NR-CDs consists in a narrow-band laser output peaking at 630 nm, with a FWHM of about 20 nm, which can be further reduced to 5 nm through the use of an optical grating in place of the end-cavity mirror. The output–input response curve of NR-CD stimulated emission (Figure 5.7b) indicates a threshold of 0.65 mJ/cm^2 per pulse. Corresponding experiments with NR dye yield a threshold of 0.06 mJ/cm^2. Comparing NR-CDs with bare NR molecules, this threshold increase may be attributed to an increase of scattering losses when the active medium is composed of nanoparticles rather than simply by the NR molecules.

Unlike traditional lasing in a Fabry Perot configuration, in a random laser, the optical feedback originates from multiple scattering instead of cavity mirrors. RLs produce an emission resembling that of a laser while simultaneously benefiting from a more straightforward and adaptable laser setup. The multiple scattering can be obtained from various media, such as polymers, crystalline materials, scattering micro-/nano-particles, or a combination of the above scattering systems. RL experiments were conducted with the NR-CDs, taking advantage of the dye embedding in the carbonaceous matrix. In this case, the active medium consisted of a NR-CD dispersion with an absorbance of 1 O.D. at 535 nm (pump wavelength) in a 1 cm optical path, mixed with a solution of TiO$_2$ nanoparticles (~30 nm sized, [2]) employed as scattering agents. RL performances of NR-CDs were compared with those of bare NR, utilizing the same active medium but with a NR solution with the same absorbance at 535 nm instead of NR-CDs. For RL experiments, a cylindrical glass vial was employed instead of a rectangular cuvette. In this way any amplification feedback loop deriving from parallel quartz walls was prevented. As shown in Figure 4.7c, the resulting RL spectrum consists in a very narrow band peaked at 630 nm, with a FWHM of 12 nm. Interestingly, this bandwidth was lower for the NR-CDs, compared to that obtained for the bare NR dye in the same RL experimental conditions (Figure 5.7c), that resulted of 19 nm. Also, the RL threshold for NR-CDs was of 30 mJ/cm^2, lower than that observed for NR, being 36 mJ/cm^2. This was attributed to the participation of the carbonaceous cores of NR-CDs in the RL emission process not only as gain media but also as scatterers, thanks to their structural features (see Figure 3.15d) and nanometric size [44]. Overall, increased scattering observed for NR-CDs compared to NR increases the bandwidth and lasing threshold for the Fabry-Perot cavity experiments. However, this feature results beneficial for RL experiments, were NR-

CDs act as a more efficient RL gain medium, exhibiting overall sharper spectral line width and lower pump intensity thresholds.

Appendix

A5.1 Experimental details on nanocomposite fabrication

Fluorescent powders of CDs were fabricated taking inspiration from already reported procedures [45,46]. The purified CDs pellet obtained at the end of the purification process (Sec. 2.1.5) was embedded in PVP to obtain a chemically stable fluorescent powder, non-hygroscopic and easily processable. In details, 2 mg of purified DCDs were dissolved in MilliQ water (1 mL) in the presence of PVP (0.4 g) under vigorous magnetic stirring. The resulting solution was drop-cast onto the surface of a glass plate where water was left to evaporate firstly at room temperature for ~1 h and then in an oven at 60°C for 2–3 h, forming a compact deposited layer. Then the solid film was scraped off the glass surface and finely ground into a mortar to obtain an emitting CD fluorophore powder.

For nanocomposite films preparation, the previously prepared CD powder fluorophores were added in variable amounts (2–120 mg/mL) to aqueous solutions of PVA (0.2–0.4 g/mL) and kept under magnetic stirring until obtaining an optically clear dispersion. Such dispersions were then employed as inks to deposit fluorescent nanocomposite films onto glass or quartz substrates.

Drop-cast nanocomposites were obtained depositing a drop of ink of a volume of either 50 or 100 µL onto a quartz substrate and leaving the solvent to evaporate. Specifically, in the case of inks with 0.4 g/mL PVA, the solvent was allowed to evaporate slowly at room temperature. For 0.2 g/mL PVA inks, the films were kept on a heating plate at 40°C to accelerate the solvent evaporation.

Spin-coated nanocomposites deposited using a two-step spinning recipe: 30 s at 800–1000 rpm (low speed) and 60 s at 6000 rpm (high speed). This procedure ensured an effective removal of edge beads.

A5.2 Mathematical details underlying simulations and colorimetric property evaluation

Formal definition of quantities in (5.1). The spectral densities of irradiance (in W/cm^2/nm) for the blue and green/red components are called $\Phi^B(\lambda)$ and $\Phi^{GR}(\lambda)$. The spectral density of the total irradiance ($\Phi(\lambda)$) is defined as:

$$\Phi(\lambda) = \Phi^B(\lambda) + \Phi^{GR}(\lambda) \qquad\qquad (A5.1)$$

Considering that colorimetric calculations (including CIE coordinates, CCT, and CRI) rely on normalized spectral irradiance quantities [2], we can employ a dimensionless relative spectral density of irradiance (or relative color stimulus function), identified as $\phi(\lambda)$.

$\phi(\lambda)$ will be given by $\Phi(\lambda)$ (measured by spectroscopic data), divided by a normalization factor (k):

$$\phi(\lambda) = \frac{\Phi(\lambda)}{k} \qquad (A5.2)$$

In general, the normalization constant k can be set according to specific convenience. Herein, we choose to define k as the integrated area of $\Phi(\lambda)$, called A_{TOT} (in W/cm^2) multiplied by 1 nm:

$$k = A_{TOT} \cdot 1nm \qquad (A5.3)$$

where multiplication by 1 nm only serves to ensure that $\phi(\lambda)$ is dimensionless.

We can note that, called A^{GR} and A^B the integrated areas of $\Phi^{GR}(\lambda)$ and $\Phi^B(\lambda)$, the following relations hold:

$$k = (A^{GR} + A^B) \cdot 1nm \qquad (A5.4)$$

$$\Phi^{GR}(\lambda) = A^{GR}\phi^{GR}(\lambda) \cdot 1nm \qquad (A5.5)$$

$$\Phi^B(\lambda) = A^B\phi^B(\lambda) \cdot 1nm \qquad (A5.6)$$

(5.1-5.2) are obtained substituting (A5.4-A5.6) and (A5.2) into (A5.1)

Derivation of f_m and underlying assumptions. We consider a primary source parallel light beam with an in-plane irradiance I_0^S (W·cm^{-2}), characterized by a monochromatic wavelength in the blue, incident on the surface of a DCD nanocomposite slab. While propagating, the primary blue beam is attenuated, and concurrently, part of the absorbed radiation is converted into light at longer wavelengths, forming the green and red emission bands.

Neglecting reflections and scattering at the surface of the nanocomposite, as well as assuming that the generated spectrum is collected integrating over a 360° angle, the irradiance of the attenuated transmitted blue beam (I^S) and of the PL generated in the nanocomposite (I^{PL}) can be easily calculated with the equations:

$$I^S = I_0^S \, e^{-\alpha_B d} \qquad (A5.7)$$

$$I^{PL} = PLQY \left(I_0^S - I^S \right) \qquad (A5.8)$$

where α_B, d and PLQY are the absorption coefficient at the incident wavelength, nanocomposite slab thickness, and PLQY of fluorophores in the nanocomposite, measured exciting at the incident light wavelength.

Both I^S and I^{PL} can be approximated with the areas of their spectral distribution if the spectra are recorded over a sufficiently broad range:

$$I^S \approx A^B \tag{A5.9}$$

$$I^{PL} \approx A^{GR} \tag{A5.10}$$

Substituting (A5.9-A5.10) in (5.3) we obtain:

$$f_m \approx \frac{I^{PL}}{I^S + I^{PL}} \tag{A5.11}$$

and substituting (A5.7-A5.8) into (A5.11) we obtain (5.4).

Calculation of ΔCIE, ΔCCT% and ΔCRI

The deviations ΔCIE, ΔCCT% and ΔCRI were calculated as:

$$\Delta CIE = \left(x_{exp} - x_{D65}\right)^2 + \left(y_{exp} - y_{D65}\right)^2 \tag{A5.12}$$

$$\Delta CCT\% = \frac{\left|CCT_{exp} - CCT_{D65}\right|}{CCT_{D65}} \times 100 \tag{A5.13}$$

$$\Delta CRI = \mathrm{CRI}_{D65} - CRI_{exp} \tag{A5.14}$$

Where CCT_{exp} and CRI_{exp} refer to the experimentally measured properties, and CCT_{D65} = 6500 K and CRI_{D65} = 100 refer to the properties of D65 standard illuminant.

Obtainment of colorimetric properties from PL spectra. Chromaticity Coordinates (CIE 1931 standard 2-degree observer), CCT, and general CRI were determined using MATLAB software (R2021b, v. 9.11.0), supplemented with the pspectro Add-on [63]. The input for colorimetric property calculation comprised the relative spectral density of irradiances, normalized 1 nm-spaced PL spectra in absolute radiometric units (W·cm^{-2}).

Numerical estimation of best achievable white colorimetric properties. Best white chromaticity coordinates were calculated as simulated CIE 1931 chromaticity coordinates minimizing the function:

$$(x_i - x_{D65})^2 + (y_i - y_{D65})^2 \tag{5.15}$$

where x_i and y_i are simulated coordinates and x_{D65} and y_{D65} are the coordinates of D65 illuminant.

References

[1] G. Minervini, A. Madonia, A. Panniello, E. Fanizza, M.L. Curri, M. Striccoli, Nanomaterials 13 (2023) 374.

[2] A. Madonia, G. Minervini, A. Terracina, A. Pramanik, V. Martorana, A. Sciortino, C.M. Carbonaro, C. Olla, T. Sibillano, C. Giannini, E. Fanizza, M.L. Curri, A. Panniello, F. Messina, M. Striccoli, ACS Nano 17 (2023) 21274–21286.

[3] Y. Huo, S. Xiu, L.-Y. Meng, B. Quan, Chemical Engineering Journal 451 (2023) 138572.

[4] Y. Liu, F. Liang, J. Sun, R. Sun, C. Liu, C. Deng, F. Seidi, Nanomaterials 13 (2023) 2869.

[5] M. Moniruzzaman, B. Anantha Lakshmi, S. Kim, J. Kim, Nanoscale 12 (2020) 11947–11959.

[6] M.M. Hussain, W.U. Khan, F. Ahmed, Y. Wei, H. Xiong, Chemical Engineering Journal 465 (2023) 143010.

[7] D. Benner, P. Yadav, D. Bhatia, Nanoscale Adv. 5 (2023) 4337–4353.

[8] K. Jiang, S. Sun, L. Zhang, Y. Lu, A. Wu, C. Cai, H. Lin, Angewandte Chemie International Edition 54 (2015) 5360–5363.

[9] A. Sigov, L. Ratkin, L.A. Ivanov, L.D. Xu, Inf Syst Front (2022).

[10] A. Massaro, Applied Sciences 13 (2023) 4582.

[11] C. Ji, W. Xu, Q. Han, T. Zhao, J. Deng, Z. Peng, Nano Energy 114 (2023) 108623.

[12] S. Gavalas, A. Kelarakis, Nanomaterials 11 (2021) 2089.

[13] Z. Zhu, Y. Zhai, Z. Li, P. Zhu, S. Mao, C. Zhu, D. Du, L.A. Belfiore, J. Tang, Y. Lin, Materials Today 30 (2019) 52–79.

[14] X. Xu, L. Mo, Y. Li, X. Pan, G. Hu, B. Lei, X. Zhang, M. Zheng, J. Zhuang, Y. Liu, C. Hu, Advanced Materials 33 (2021) 2104872.

[15] Y. Chen, M. Zheng, Y. Xiao, H. Dong, H. Zhang, J. Zhuang, H. Hu, B. Lei, Y. Liu, Advanced Materials 28 (2016) 312–318.

[16] Y. Zhang, P. Zhuo, H. Yin, Y. Fan, J. Zhang, X. Liu, Z. Chen, ACS Appl. Mater. Interfaces 11 (2019) 24395–24403.

[17] Y. Zhang, J. Xiao, P. Zhuo, H. Yin, Y. Fan, X. Liu, Z. Chen, ACS Appl. Mater. Interfaces 11 (2019) 46054–46061.

[18] M.D. Tyona, 1 2 (2013) 195–208.

[19] M. Eslamian, Nano-Micro Lett. 9 (2016) 3.

[20] M. Eslamian, F. Soltani-Kordshuli, J Coat Technol Res 15 (2018) 271–280.

[21] N. Chapman, M. Chapman, W.B. Euler, Coatings 11 (2021) 198.

[22] Y. Yu, Z. Wu, L. He, B. Jiao, X. Hou, Thin Solid Films 589 (2015) 852–856.

[23] C. Ehrenborg, (n.d.).

[24] G. Abadias, E. Chason, J. Keckes, M. Sebastiani, G.B. Thompson, E. Barthel, G.L. Doll, C.E. Murray, C.H. Stoessel, L. Martinu, Journal of Vacuum Science & Technology A 36 (2018) 020801.

[25] M.A. Kats, F. Capasso, Applied Physics Letters 105 (2014) 131108.
[26] J. Schanda, International Commission on Illumination, eds., Colorimetry: Understanding the CIE System, CIE/Commission internationale de l'eclairage ; Wiley-Interscience, [Vienna, Austria] : Hoboken, N.J, 2007.
[27] T.-X. Lee, C.-Y. Lin, S.-H. Ma, C.-C. Sun, Opt. Express 13 (2005) 4175.
[28] J. Jarominski, Appl. Opt. 21 (1982) 3190.
[29] J.-S. Li, Y. Tang, Z.-T. Li, Z. Li, X.-R. Ding, L.-S. Rao, IEEE J. Select. Topics Quantum Electron. 23 (2017) 1–7.
[30] C. Oleari, Standard Colorimetry: Definitions, Algorithms, and Software, John Wiley & Sons, Inc, Chichester, West Sussex, UK, 2016.
[31] H.V. Demir, S. Nizamoglu, T. Erdem, E. Mutlugun, N. Gaponik, A. Eychmüller, Nano Today 6 (2011) 632–647.
[32] W. Ding, Y. Wang, H. Chen, S.Y. Chou, Advanced Functional Materials 24 (2014) 6329–6339.
[33] J. Jarominski, Appl. Opt. 21 (1982) 3184.
[34] V.F. Traven, D.A. Cheptsov, C. Lodeiro, J Fluoresc 33 (2023) 799–847.
[35] C.-H. Chen, Y.-T. Tsao, J Sol-Gel Sci Technol 83 (2017) 190–196.
[36] A. P. Green, A. R. Buckley, Physical Chemistry Chemical Physics 17 (2015) 1435–1440.
[37] J. Ren, L. Stagi, P. Innocenzi, Progress in Solid State Chemistry 62 (2021) 100295.
[38] C.J. Reckmeier, J. Schneider, Y. Xiong, J. Häusler, P. Kasák, W. Schnick, A.L. Rogach, Chem. Mater. 29 (2017) 10352–10361.
[39] Y. Zhang, S. Lu, Chem 10 (2024) 134–171.
[40] A. Sciortino, N. Mauro, G. Buscarino, L. Sciortino, R. Popescu, R. Schneider, G. Giammona, D. Gerthsen, M. Cannas, F. Messina, Chem. Mater. 30 (2018) 1695–1700.
[41] B.P. Pathrose, A. Prakash, V.P.N. Nampoori, P. Radhakrishnan, H. Sahira, A. Mujeeb, Optik 156 (2018) 988–993.
[42] M.K. Singh, H. Pal, A.C. Bhasikuttan, A.V. Sapre, Photochemistry and Photobiology 68 (1998) 32–38.
[43] C. Sousa, T. Sá e Melo, M. Gèze, J.-M. Gaullier, J.C. Mazière, R. Santus, Photochemistry and Photobiology 63 (1996) 601–607.
[44] Y. Zhang, L. Wang, Y. Hu, L. Sui, L. Cheng, S. Lu, Small 19 (2023) 2207983.
[45] K. Jiang, X. Feng, X. Gao, Y. Wang, C. Cai, Z. Li, H. Lin, Nanomaterials 9 (2019) 529.
[46] Q. Chang, X. Zhou, G. Xiang, S. Jiang, L. Li, Y. Wang, Y. Li, Z. Cao, X. Tang, F. Ling, X. Luo, Dyes and Pigments 193 (2021) 109478.

6

Sensing Applications

"Nanoparticles are the quantum architects shaping the future of sensing technology. In the hands of brilliant minds, smart chemical sensors emerge as the bridge between the microscopic and the monumental."

Naomi Halas

Abstract

This final chapter section describes the experimental data collection and part of data analysis carried out at Nanobioelectronics and Biosensors group at Catalan Institute of Nanoscience and Nanotechnology (ICN2) during the period of the PhD program spent abroad in Barcelona, Spain. The work is built upon experimental insights and chemical structural details obtained from investigations of synthesis and characterization of RCDs (Sec. 3.2). pH and ROSs sensitivity of RCD fluorescence are capitalized in the use of these nanoparticles as active fluorescent materials in a nitrocellulose platform with smartphone-based optical detection. After suitable calibrations, the platform exhibits cutting-edge capabilities in pH sensing, achieving a resolution of ±0.2 pH units within a range from 2.2 to 7. This is obtained utilizing the dual-band fluorescence of the RCDs for a fluorescence colorimetric revelation technique. Additionally, the platform demonstrates qualitative sensing of AOC, notably showcasing its effectiveness with AA as a model compound, revealing its pH-dependent AOC with a LOD of 20 mg/100 mL. The design of this platform is highly versatile, potentially adaptable to remote environments and non-trained operators. Its profitability for pH sensing spans across diverse samples including biological, wastewater, beverages, and foods. On the other hand, combined with AOC detection, it may gain particular relevance for application in beverages containing high quantities of natural antioxidants.

6.1. RCD functionalized nitrocellulose: a versatile platform for sensing of pH and antioxidant activity

In Sec. 3.2.6-3.2.7, it was demonstrated that RCD fluorescence has noteworthy properties of pH sensitivity. Additionally, Sec. 3.2.5 provided evidence that the RCD fluorescence is substantially affected by the generation of ROSs. The emission spectrum of these CDs consists of a blue and a green PL band, that are respectively ascribed to emission by surface or defect states and to the molecular emission of OH-PAHs embedded within the nanoparticles (Figure 6.1).
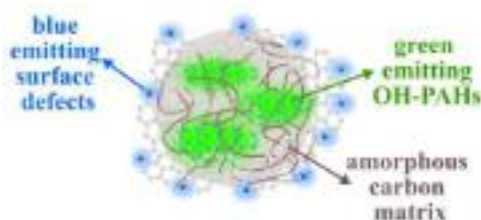

Figure 6.1: *schematic illustration of the hypothesized structure of RCDs following structural, chemical and photophysical characterizations described in Sec. 3.2.*

Herein, the pH and ROS sensitivity of RCDs is harnessed in a portable sensing platform that uses functionalized nitrocellulose as substrate. In the method described here, the RCD fluorescence changes in response to pH are revealed through a smartphone camera, without use of benchtop fluorescence revelation instruments. Moreover, the fluorescence intensity is quantified via a colorimetric image analysis that enables reaching high pH measurement resolutions (up to ±0.2 pH units) in a pH range of 2.2-7.0. Thus, the resulting resolution and dynamic range make this sensing platform well-suited for a wide range of samples and real-world practical applications, including analysis of beverages, foods, wastewaters, biological samples [1–4]. Additionally, the platform is capable of operating with very small sample volumes and does not require periodic calibrations. Therefore, it results compatible with the use by non-specialized personnel and for pH measurement in remote environments [2,5,6]. Overall, these characteristics could make this sensing platform virtually capable of integrating high-resolution pH measurements in advanced manufacturing processes [1,6,7].

Next, the functionalities of the platform can be expanded, demonstrating that it is capable of assessing of AOC of chemical compounds. Specifically, as proof-of-concept the antioxidant molecule AA is selected, as renowned for having AOC tightly dependent on pH. This enables to qualitatively showcase the capabilities of

the mobile sensing strategy to detect antioxidant activity of AA under different pH conditions. The LOD of 20 mg/100 mL makes this sensing platform compatible with the analysis of several beverages rich in AA, such as citrus juices and others [8–11]. Overall, the approach presented herein could have applicative relevance for the monitoring of pH in several applicative areas. Moreover, if combined with AOC evaluation, the developed strategy can be helpful for agrifood-food monitoring of AA-rich products, where both pH and AOC variations of food product over time play a crucial role.

6.1.1. Functionalization of nitrocellulose pads: calibration of RCDs for pH sensing

The preparation of the nitrocellulose substrate consisted in a simple fabrication of circular nitrocellulose pads (CNPs) by printing a hydrophobic wax. The complete experimental procedure is described in Sec. 6.1.4 and visually schematized in Figure 6.2. After their preparation, the CNPs were functionalized by incorporating the RCDs. This was carried out by drop-casting an aqueous RCD dispersion, followed by soft heating to allow water evaporation. Functionalized circular nitrocellulose pads (F-CNPs) were thus obtained.
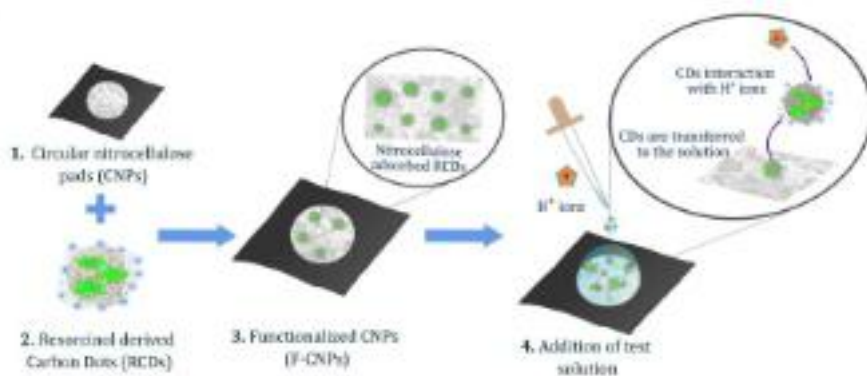

Figure 6.2: *schematic description of the process of fabrication of RCD-functionalized circular nitrocellulose pads (F-CNPs)*

The sensing strategy can be summarized as follows: upon drop-casting a test solution onto the F-CNPs, a fraction of the RCDs immobilized onto the CNPs are solubilized in the aqueous phase and hence transferred to the solution drop atop the CNP (point 4). Once in the aqueous phase, in the case of pH sensing, interaction of RCDs with H$^+$ takes place. This interaction results in an alteration of the RCD fluorescence properties that is analyzed by a smartphone-based fluorescence revelation system, equipped with optical filters (Figure 6.3) (for further technical specifications see Sec. 6.1.4). More specifically, all experiments herein were carried out comparing the fluorescence of a F-CNP wet by a droplet of test solution

with respect to that of an internal reference, being either a reference sample or a blank, as explained in detail in the following sections.
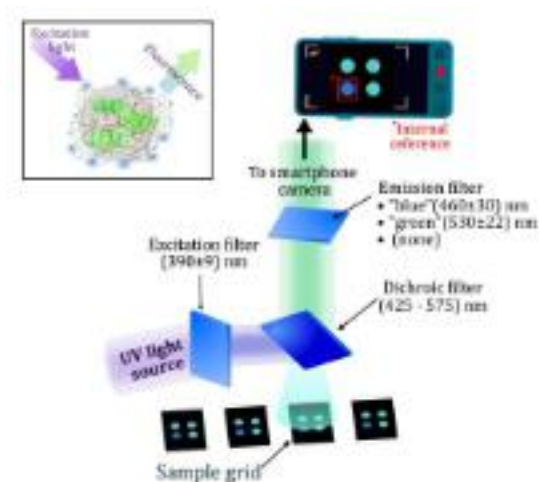

Figure 6.3*: schematic description of the smartphone-based fluorescence revelation system. Optical emission filters with bandwidths of (460±30) and (530±22) nm are labelled as "blue" and "green" emission filters in the following.*

Within our platform, it appears evident that we can maximize the detected fluorescence adjusting the formulation (e.g., nanoparticle concentration or pH) of the initial pristine RCD dispersion. First, the concentration of RCDs deposited in the F-CNPs is a pivotal parameter to calibrate. In fact, the nanoparticle concentration will influence the overall fluorescence intensity. For this purpose, an experiment was carried out in which dispersions of RCDs at increasing concentration were deposited on CNPs. The fluorescence was then revealed using the smartphone-based apparatus (Figure 6.3, Sec. 6.1.4). Smartphone digital pictures were acquired at increasing exposure times, obtained by modulation of the shutter speed in the range 0.2 – 0.5 s and employing blue and green emission optical filters (Figure 6.4a-b). Following acquisition, the digital pictures were processed to separate their three-color channels–Red (R), Green (G) and Blue (B). Details of such image analysis procedure are described in Sec. 6.1.4 and Sec. A6.1. Subsequently, as shown in Figure 6.4c-d, the intensity of each channel is analyzed separately. Then, the fluorescence is evaluated quantitatively from the intensities of B (blue emission filter) or G (green emission filter) channels, as shown in Figure 6.4e-f.
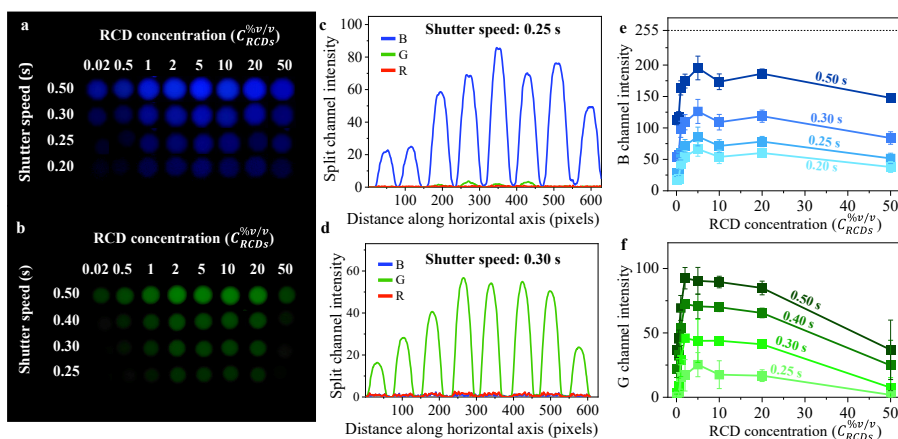
Figure 6.4: *(a, b) smartphone digital pictures, (c, d) plots of B, G and R channels as a function of the distance along the horizontal axis of the picture, and (e, f) resulting B and G channel intensities of F-CNPs drop-casted with RCD dispersions at $C_{RCDs}^{\%v/v}$ from 0.02 to 50%$_{v/v}$. Pictures and B, G channel intensities have been acquired using (a, e) blue emission filter and shutter speed in the range of 0.20-0.50 s and (c, f) green emission filter and shutter speed in the range of 0.25-0.50 s. The upper scale limit of the grayscale range (0 - 255) is highlighted in (e) as a guide for the eye. The error bars are standard deviations calculated from three experiment replicates.*

It is evident from a simple comparison of Figure 6.4a and Figure 6.4c that the utilization of the blue emission filter leads to a fluorescence signal exclusively in the B channel. On the other hand, only some residual intensity is noted in the G channel and the R channel registers only noise. Vice versa, upon the application of the green emission filter, only the G channel reveals a discernible signal, while the B and R channels exhibit noise exclusively. This confirms that the blue and green emission filters, applied to the fluorescence light emitted by the RCDs, allow independent analysis of the spectroscopic blue and green PL bands of the RCDs, centered at around 455 and 520 nm respectively (Sec. 3.2).

Nanoparticle concentration and shutter speed produce evident intensity alterations on the recorded digital pictures. The intensities of B and G channels depicted in Figure 6.4e-f allow quantitative evaluation of these changes. For both B and G channels, the intensity increases linearly with the RCD concentration up to 2%; then, a saturation range is observed in the 2 – 20% interval. Subsequently, a decrease of fluorescence is observed upon further RCD concentration increase up to 50%. Such self-quenching of fluorescence with increasing concentration is a well-known phenomenon for many fluorophores [12–14], including CDs [15–19], and is typically ascribable to re-absorption of emitted photons, due to overlapping of absorption and fluorescence bands. Remarkably, the results in Figure 64 highlight that the dampening due to photon re-absorption is more pronounced for

the G intensity than for B intensity. This tightly agrees with the spectroscopic properties of RCDs (Sec. 3.2.3) and can be explained considering that the green band has a very small Stokes shift. This remarks how changes in RCD spectroscopic features observed in cuvette and using a benchtop spectrofluorometer (Sec.2.2) are retained in the B and G channels after deposition on CNPs and image analysis. It also worth to note that, within the investigated range of shutter speed, the trends of B and G channel intensity with $C_{RCDs}^{\%v/v}$ result independent from the shutter speed. This points out that the exposure time can be flexibly adjusted within the interval from 0.2 to 0.5 s, to optimize the signal-to-noise ratio in the resulting pictures.

Besides nanoparticle concentration, the state of protonation of –CO$^-$ groups of RCDs in another crucial parameter to optimize. In fact, it is determining both for fluorescence characteristics of RCDs (high QY, intensity ratio of blue and green PL bands) and for the sensitivity of these properties to pH variations (Sec. 3.2.3-3.2.7). Within the preparative approach, the protonation state of RCDs can be modified by modifying the pH of the pristine dispersion employed for the CNP functionalization. Overall, our goal is to identify the appropriate combination of RCD concentration and pH of RCD dispersion to attain the best responsivity to pH. At this scope, a calibration was carried out using dispersions at various $C_{RCDs}^{\%v/v}$ and pHs. The detailed procedure of optimization of pristine RCD dispersion is provided in Sec. A6.2. This procedure aimed at finding the best balance between high fluorescence intensity (high image signal-to-noise ratio), low spurious background signals, wide pH dynamic range and high resolution in pH measurements. Based on these quantitative assessments, the dispersion having $C_{RCDs}^{\%v/v}$ of 10% and pH = 8 (denoted as ML0810) was selected as the most favorable to functionalize CNPs for further pH sensing experiments.

6.1.2. *pH sensing with F-CNPs: the fluorescence colorimetry approach*

Achieving a fully operational pH sensing based on the RCDs in the nitrocellulose pads also demands an efficient method to analyze and compare the fluorescence data resulting from the acquired digital pictures. The use of blue or green emission filters during image recording and analysis isolates the blue and green PL bands of the RCDs. However, this leads to a single-channel fluorescence signal. In fact, with applied emission filters, it is not possible to reveal both the blue and green fluorescence bands simultaneously. Moreover, repeating the picture acquisition alternating the two different emission filters would introduce operational complications to the method and more importantly, increase the overall response time. Therefore, to solve this issue, a simple and effective solution was developed herein. This consists in acquiring the digital pictures without emission filters and analyzing them in terms of colorimetric coordinates. As depicted in Figure 6.5, this strategy was applied to attain the pH sensing.
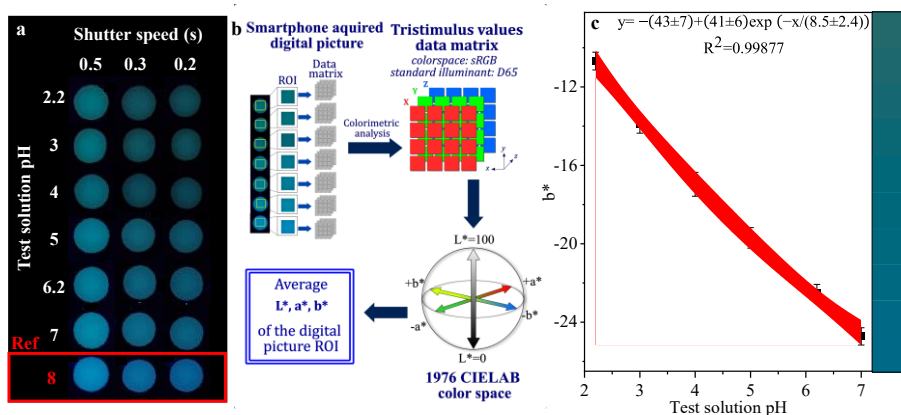
Figure 6.5: *(a) smartphone pictures obtained without emission filters at shutter speeds of 0.5, 0.3 and 0.2 s for F-CNPs functionalized with ML0810 RCD dispersion (dispersion with optimized $C_{RCDs}^{\%v/v}$ and pH, Sec. A.6.2) and drop-casted with test solutions at pH of 8, 7, 6.2, 5, 4, 3, 2.2; (b) schematic description of the image analysis procedure used to obtain the CIELAB (L^*, a^* and b^*) coordinates from each F-CNP; (c) b^* coordinate of F-CNPs (shutter speed 0.5 s) as a function of test solution pH (black squares), fitted using the equation (6.1) (red line). The red shaded area represents the 95% confidence interval, the error bars are standard deviations obtained from three replicates of the same experiment, the color scale legend on the right shows the perceptual colors corresponding to b^* varying in the range of y-axis coordinates for fixed $L^* = 40$ and $a^* = -20$ (approximate average values of L^* and a^* obtained from the image analyses for shutter speed of 0.5 s).*

The digital pictures obtained without emission filters (Figure 6.5a) show a progressive color change from green to blue as the pH of test solution increases from 2.2 to 8. This again, closely agrees with the spectroscopic variation of the blue to green intensity ratio observed upon pH increase (Sec. 3.2.7).

The procedure to obtain colorimetric coordinates from the recorded pictures is schematically explained in Figure 6.5b. The procedure, operated within a suitably written MATLAB script, begins with a quantification of the intensities in the split R, G and B channels separately, using a procedure described in detail in Sec. A6.1 and equivalent to that employed for color quantifications in Sec. 6.1.1 (Figure 6.4). However, in this case, the obtained R, G and B intensities were subsequently converted into X, Y, Z tristimulus values, particularly using sRGB color space (native color space of the pictures) and assuming D65 as standard illuminant, in line with CIE recommendations [20]. Finally, a transformation in the CIELAB 1976 color space was performed [21]. Thus, CIELAB coordinates, averaged on the area of each ROI, were obtained. The variable L* ranges between 0 and 100 and represents how light or dark a color is, with higher values indicating lighter shades. On the other hand, a* measures the color position on the green to red axis,

where negative values represent green tones and positive values represent red tones. Finally, b* indicates the color position on the blue to yellow axis, with negative values for blue tones and positive values for yellow tones.

Results of the colorimetric analyses indicated that a* was affected by high experimental errors, associated to dependence from the R channel intensity, that in our case only contains noise (Figure 6.4b-c). On the other hand, L* was found to be proportional to the overall intensity of the F-CNP fluorescence (Sec. A6.2). This is consistent with the concept that L* represents the perceptual lightness of the observed signal. As detailed in Section A6.2, this variable could also, in principle, be employed for pH determination through a single-channel fluorescence sensing strategy. However, this methodology yields resolutions that do not exceed ±1 pH unit.

Nonetheless, b* was found to effectively capture the perceptual color transition observed in the pictures with changing pH. This becomes more evident when looking at the perceptual colors given by a variation of b* when L* and a* are fixed at typical values obtained in the analyzed pictures (color scale legend in Figure 6.5c). Specifically, the trend of b* as a function of test solution pH could be best fitted using a decreasing exponential function, of the type:

$$y = a_1 + a_2 \exp(x/a_3) \qquad (6.1)$$

yielding $a_1 = 43 \pm 7$, $a_2 = 41 \pm 6$, $a_3 = 8.5 \pm 2.4$ and R^2 of 0.99877. From this fitting curve, the 95% confidence interpolation errors resulted of ±0.2 pH units in the pH range from 2.5 to 6.7 and of ±0.3 pH units in the pH range of 6.7 to 7.0.

This reveals an improvement compared to typical resolution allowed by the most common commercial pH indicator paper strips [22,23]. Recent literature works documented paper- or polymer-based colorimetric pH sensing devices that surpass the capabilities of currently available commercial pH paper strips [2–12]. However, it is worth remarking that these works involved one or more of the following shortcomings: (i) use of expensive sensitive materials for pH detection (e.g. commercial or in-house synthesized indicator dyes), (ii) sophisticated protocols for substrate patterning (e.g. involving laser patterning, customized ink-jet printing), or (iii) dynamic range limited to 3-5 pH units [24–41]. In comparison, the sensing method reported herein relies on environmentally sustainable and cost effective CDs. Moreover, it involves a user-friendly preparation approach and grants pH measurement with uniform resolution across six pH units. Furthermore, the present work highlights the integration of colorimetric analysis on fluorescence data recorded by portable devices, to enable highly accurate sensing measurements, as highlighted by the significantly lower resolution obtained applying a single-channel fluorescence detection (Sec. A.6.2)). Similar colorimetric analysis of fluorescence data obtained by portable devices was reported in very

few previous reports [42,43]. In this work, the fluorescence analysis approach leads to significant improvements of the sensing accuracy, thanks to its capability of harnessing simultaneously the sensing information coming from the blue and the green PL bands of the RCDs. Overall, given the resolution and dynamic range attainable with this method, it appears as an effective combination of accuracy and practical operational efficacy. Therefore, its applicability may extend to various fields in which pH evaluation is critical and particularly when the operational conditions pose challenges for presently established instruments, such as potentiometric pH meters. Similar problems could be pervasive of disparate areas, including biological samples, food chemical analyses, water quality assessment, and others [2–5].

6.1.3. Expanding the potentialities of RCDs in F-CNPs towards AOC monitoring portable devices

To better demonstrate the potential versatility of the developed nitrocellulose-based strategy, a further possibility is harnessing the dampening of the RCD blue PL band due to activity of ROSs (Sec. 3.2.5). This sensitivity of RCDs can be tackled to implement a strategy than enables examining the AOC of antioxidant compounds in the nitrocellulose-based sensing approach. More specifically, AA was chosen as target to explore the capabilities of the proposed method. AA is a well-established and extensively studied antioxidant and it is used as a reference in various AOC assays [44–46]. Moreover, it is well-known for having AOC characteristics closely dependent on pH and concentration [47–53]. Therefore, it is an excellent candidate to better investigate the potentialities of the fabricated nitrocellulose platform.

To introduce AOC assessment of AA in this sensing method, first, CNPs previously functionalized with RCDs were drop-casted with test solutions at different pHs, containing AA in different concentrations (Figure 6.6). After test solution addition, the F-CNPs were kept under a UV light source to induce generation of ROSs in the sample (Sec. 3.2.5) [54]. Then, the fluorescence color of such UV-treated F-CNPs was compared to that of non-UV-treated F-CNPs (dark F-CNPs). The color difference between the two samples was compared measuring the b^* colorimetric coordinate and then calculating their difference (Δb^*). These experiments required particular precautions for the optimization of CNP functionalization and shutter speed of digital pictures that differed to that of pH sensing experiments, as explained in detail in Sec. 6.1.4.
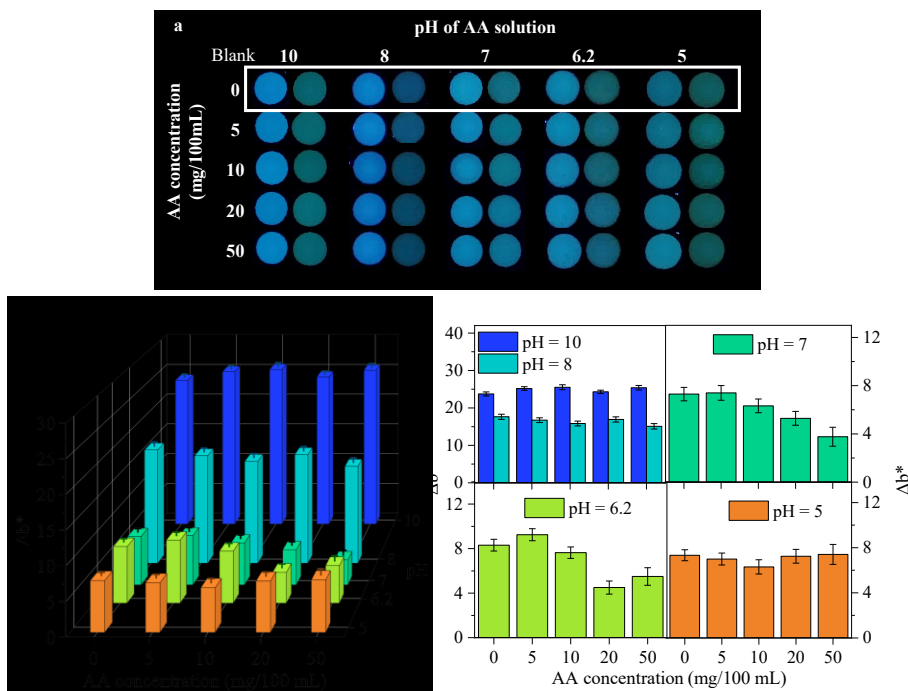
Figure 6.6: (a) smartphone digital pictures (shutter speed: 2 s) of dark (left) and UV-treated (right) CNPs functionalized with RCDs (MilliQ water, $C_{RCDs}^{\%v/v}$ =10%) and drop-casted with test solutions at pH of 10, 8, 6.2 and 5 and containing AA in concentration of 0, 5, 10, 20 and 50 mg/100 mL; (b) 3D bar plot showing the Δb* (difference of b* between dark and UV-treated samples) as a function of pH and AA concentration; (c) visualization of the Δb* as a function of AA concentration, subdivided in four panels representing the different pH ranges. Error bars are standard deviations obtained replicating three times the same experiment.

For all investigated pH and AA concentration, the recorded pictures show a decrease in intensity and color shift from blue to green between the dark and UV-treated samples. This is tightly correlated to the spectroscopic dampening of the blue band observed in RCD photobleaching experiments (Sec. 3.2.5) and it is ascribable to the surface chemical group degradation taking place in the RCDs.

Interestingly, this can enable the use of the RCDs as indicators for the activity of antioxidants, e.g., AA. In fact, antioxidants in general have scavenging capabilities and consequently, subtract ROSs from the solution. Therefore, in their presence, RCDs are expected to undergo a diminished level of photochemical degradation. Since a high photochemical degradation is reflected in a high color change (Δb*), the activity of antioxidants should manifest as a decrease of the observed Δb*.

Distinguishing similar alterations of Δb^* is very challenging with the only naked eye inspection. However, performing the colorimetric analysis on the digital pictures, the quantitative assessment of b^* and of its variations is possible. This analysis, whose outcomes are depicted in Figure 6.6b-c, reveals that, for test solutions at pH of 6.2 and 7, at AA concentrations of 20 and 50 mg/100 mL, the Δb^* is reduced with respect to the blank solutions (0 mg/100 mL AA). Such decrease in photobleaching of RCDs must be ascribed to increased ROS scavenging activity of AA with its concentration, being the only variable changing between blank samples and the test solutions. Therefore, this points out that AA has a measurable AOC in the investigated conditions of pH and concentration.

Notably, this result aligns with previous studies illustrating that the ROSs scavenging ability of AA, particularly towards singlet oxygen (the predominant ROS produced by UV irradiation of aqueous solutions containing dissolved O_2 [55]), is maximum exactly in the pH range of roughly 6 – 7. This pH range is in fact generally associated with maximum scavenging efficiency thanks to the high ratio of ascorbate to ascorbic acid, coupled with a relatively high stability of the AA solution [47,48,53,56–60].

The concentration range at which the AOC of AA is detected suggests potential significant relevance of this method for food analysis, especially for various types of fruit juices, extracts or natural beverages [49,50,52,61–70]. For example, most commercial citrus fruit juices have AA content of at least 30-40 mg/100 mL. Moreover, the UV treatment employed in the developed method to generate ROSs could be simply upscaled to industrial technologies, where employed for monitoring the stability of antioxidant in liquid foods after some industrial food-processing steps. UV technologies have undergone a huge implementation increase in the agrifood sector, for microbial disinfection, pasteurization and sanitization of products, surfaces, machineries, packages, etc. [54,71,72]. For instance, UV industrial-scale pasteurization of fruit juices is currently a very widely and actively examined opportunity [73,74]. In fact, UV technologies are being preferred to the more traditional thermal pasteurization of the liquid beverages, because they allow microorganism inactivation while preventing protein denaturation and better preserving the taste, freshness, color and external appearance of the products [73–77]. The method developed here could be simply implemented in similar technologies using the industrial-scale UV irradiation setups for the UV treatment of F-CNPs and a very limited volume of sample. More in general, similar portable chemical sensing platform could contribute to the integration of rapid and reliable chemical sensing in such automated industrial processes.

6.1.4. Experimental details

Fabrication of RCD-functionalized nitrocellulose pads and smartphone-based fluorescence detection. A nitrocellulose membrane strip (Unisart® CN95, Sartorius) was patterned to create CNPs with a diameter of 2.5 mm spaced by a 1.5 mm distance. The pattern was created by printing a black hydrophobic wax using a Xerox ColorQube 8580 solid ink printer. After printing, the nitrocellulose strip was kept on a hot plate at 90°C for 30 s to allow diffusion of the hydrophobic wax across the entire width of the nitrocellulose.

After their preparation, the CNPs were functionalized by drop-casting 2 µL of a pristine aqueous dispersion of RCDs, followed by drying on a hot plate at 50°C for 15-20 min, until complete water evaporation. After the preparation of the F-CNPs, a typical sensing experiment consisting in drop-casting 2 µL of a test solution onto the F-CNPs was carried out.

After test solution casting, the fluorescence was analyzed with a Microscopy Cube Assembly (TLV-U-MF2, THORLABS©), equipped with an excitation filter (MF390-18, 390±9 nm), a dichroic filter (MD416 425 - 575 nm) and optional emission filters (MF460-60, 460±30 nm, referred to as "blue emission filter" in the following or MF530-43, 530±22 nm, referred to as "green emission filter" in the following). The employed setup allowed irradiating and analyzing four F-CNPs in each single acquisition. For pH sensing experiments, each pool of four pads contained one pad drop-casted with a pH 8 McIlvaine buffer, that was used as internal reference, while for AOC experiments, one of the four pads was a blank test solution (0 mg/100 mL AA).

The fluorescence of the F-CNPs added with test solutions was detected recording digital pictures with a smartphone camera (Realme GT NEO 3T) in manual mode, autofocus, ISO at 100 and adjusting the shutter speed in order to optimize the exposure conditions.

Preparation of RCD dispersions for CNP functionalization and test solutions. To prepare the dispersions of RCDs for F-CNPs fabrication, a stock dispersion of RCDs 1.6 mg/mL was prepared by dissolving the dried purified RCD powders in a 10^{-3} M NaOH aqueous solution. This stock dispersion was then diluted opportunely to obtain the aqueous RCD dispersions for F-CNPs fabrication. Dilution of the pristine RCD dispersion and its pH were optimized separately for the pH sensing and AOC evaluation experiments, as described in Sec. 6.1.2 and Sec. 6.1.3. For RCD concentration calibration experiment (Sec. 6.1.1), the dispersions were formulated at pH = 10 to optimize colloidal stability and maximize the detected fluorescence signal intensity of the F-CNPs.

In Sec. 6.1.1-6.1.3, the concentration of RCDs in the pristine dispersions is expressed as volume-to-volume percentage concentration referred to the stock solution:

$$C_{RCDs}^{\%v/v} = \frac{V_{stock}}{V_T} \times 100 \qquad (6.2)$$

where V_{stock} is the volume of stock dispersion diluted in a total volume V_T of pristine RCD dispersion for F-CNP fabrication.

Preparation of buffers. McIlvaine (citrate-phosphate) buffer solutions at pH ranging from 8 to 2.2 were obtained mixing stock solutions of 0.1 M citric acid and 0.2 M Na_2PO_4 in different volume ratios up to reaching a final volume of 5 mL [78]. Carbonate-Bicarbonate buffer at pH 10 was analogously obtained by mixing adequate volumes of 0.1 M stock solutions of Na_2CO_3 and $NaHCO_3$.

AOC evaluation experiments. For experiments aimed at monitoring the AA stability in solution as a function of pH and its concentration (Sec. 6.1.3), the CNPs were functionalized with RCD aqueous dispersions in MilliQ water, with $C_{RCDs}^{\%v/v} = 10\%$. The test solutions were obtained dissolving AA in concentrations ranging from 5 to 50 mg/100 mL in McIlvaine buffers at pH of 5, 6.2 and 7 or in carbonate-bicarbonate buffer at pH of 10. For each experiment, two F-CNPs were drop-casted with the same test solution, and only one of them was kept under UV irradiation, by placing the F-CNP under a UV lamp (Analytik Jena B-100AP Series, irradiance: 20 mW/cm^2, source-sample distance: 2.54 cm) for 10 min, while the other was kept in dark environment for the same amount of time.

Appendix

A6.1 Validation of image analysis by MATLAB script using ImageJ software

Herein, image analyses were performed using a purposely written MATLAB script, to quantitatively assess the emission of RCDs in F-CNPs. The script, written in MATLAB software (R2023b, v.23.2.0.2365128) operated a R, G, B channel splitting of a rectangular region of interest (ROI) manually selected within each fluorescent F-CNP in each digital picture. The intensities of the R, G and B channel were thus encoded in a suitable data matrix. Then, the average intensities of the R, G, and B channels on the whole ROI were computed and expressed as values in the grayscale range (0 – 255).

To evaluate the accuracy and reproducibility of such image analysis protocol, a comparative examination was carried out using another well-established image analysis software. Specifically, the ImageJ software was selected for such comparison, due to its open-source availability and current widespread use for channel splitting and other types of colorimetric analysis in portable optical sensor devices [33,79–83]. The present comparative study employed the digital pictures resulting from the calibration of nanoparticle concentration and shutter speed (Figure 5.2). On such pictures, fluorescence quantification was performed using the MATLAB script and then repeated using the ImageJ software. Specifically, in ImageJ, the color quantification was carried out selecting: Image>Color>Split Channels (Figure A5.1). The right panels in Figure A6.1 show the results of the channel splitting procedure operated with both image analysis methods.
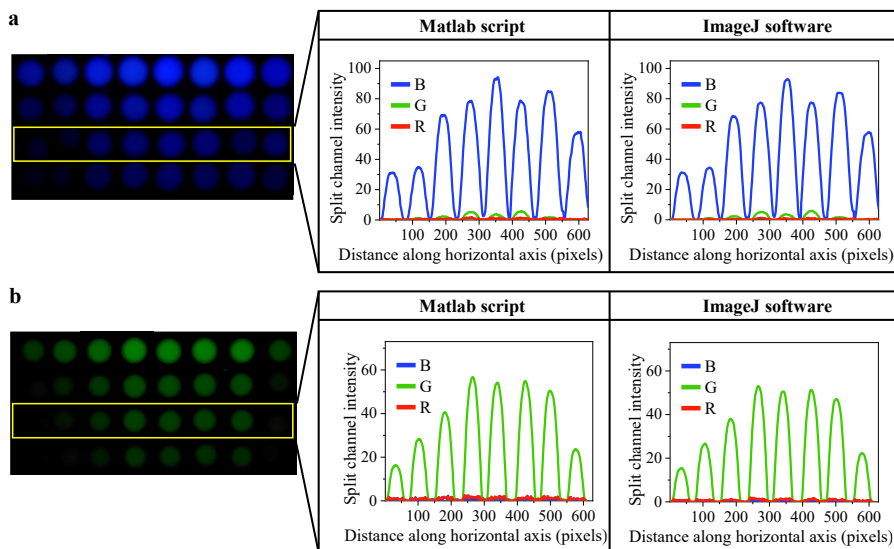
Figure A6.1: *comparative study of MATLAB script and ImageJ software: the rectangular area highlighted in the digital pictures in (a) and (b) was analyzed using both protocols; the panels on the right report the intensities of the split channels as a function of the distance along the horizontal axis of the picture.*

No noticeable differences are detected between the two image analysis protocols, either when the blue or the green emission filter are applied. In fact, the B channel in (a) and G channel in (b) show equal grayscale valued intensities, demonstrating a congruence in the quantified fluorescence intensity from either of the two software. This demonstrates that both image analysis protocols are equally capable of correctly separating the fluorescence signal between the channels and to correctly quantify its intensity.

A6.2   Calibration of RCD pristine dispersions for pH sensing

Conditions for pH measurements were optimized operating on RCD pristine dispersion, namely, by calibrating their $C_{RCDs}^{\%v/v}$ and pH. The examined conditions are listed in Table A6.1.

Table A6.1: *pristine RCD dispersions at different $C_{RCDs}^{\%v/v}$ and pH tested for calibration of F-CNPs for pH sensing.*

RCD Dispersion Code	Buffer (type, concentration, pH)	$C_{RCDs}^{\%v/v}$ (‰v/v)
ML0705	Mcllvaine, 0.1 M, pH=7	5
ML0720	Mcllvaine, 0.1 M, pH=7	20
ML0805	Mcllvaine, 0.1 M, pH=8	5
ML0810	Mcllvaine, 0.1 M, pH=8	10
ML0820	Mcllvaine, 0.1 M, pH=8	20
CB1005	Carbonate–Bicarbonate, 0.1 M, pH=10	5
CB1020	Carbonate–Bicarbonate, 0.1 M, pH=10	20

A comparative assessment of the capabilities of each of these solutions in terms of sensitivity, dynamic range and resolution of pH measurement was conducted. Digital pictures were recorded without emission filter, to allow simultaneous revelation of the blue and green PL bands (Figure A6.2).
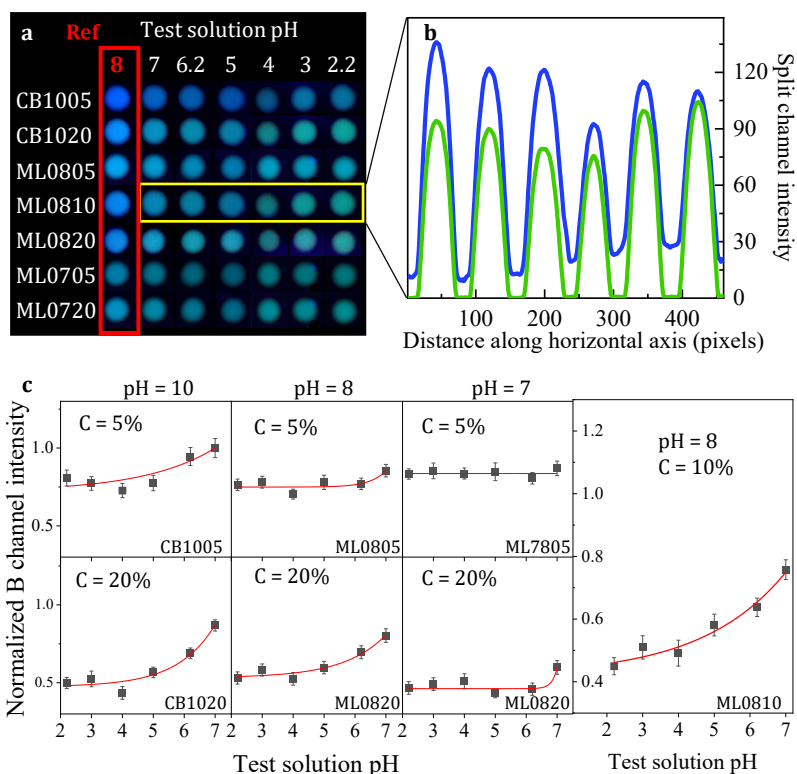
Figure A6.2*: (a) smartphone digital pictures of CNPs drop-casted with RCD dispersions listed in Table A6.1; shutter speed is 0.2 s for all the images; (b) B (blue line) and G (green line) split channel intensity as a function of horizontal distance in the picture for the ML0810 dispersion; (c) B channel intensity as a function of test solution pH for all the tested RCD dispersions (black squares) fitted using (A6.1) as model equation (red lines. The intensities are normalized dividing by the B channel intensity of the reference (test solution at pH 8), error bars are calculated as standard deviations considering three replicates of the same experiment.*

As can be observed from Figure A6.2b, when the channel splitting procedure is applied on the non-optically-filtered pictures, both B and G split channels result having fluorescence intensity. However, these digital pictures exhibit marginally increased noise, and particularly, a spurious background that is captured by the B channel. This noise can be easily explained as a small background fluorescence coming from the CNPs (Figure A6.3). This stray fluorescence light at λ>425 nm cannot be filtered by the dichroic filter, but only by emission filters. However, the potentially adverse impact of the fluorescence background on the resulting fluorescence data can be treated as a parameter to optimize trough proper adjustment of the pristine RCD dispersion. In particular, the $C_{RCDs}^{\%v/v}$ and pH of the

pristine RCD dispersion were calibrated to decrease the background fluorescence and increase the sensitivity, dynamic range and accuracy of pH measure.
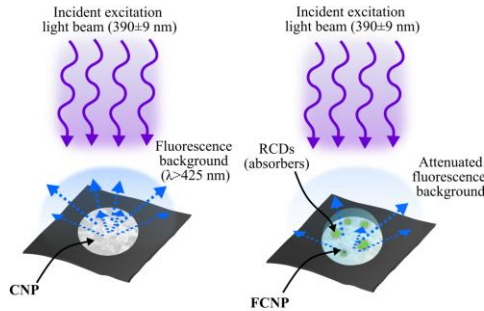

Figure A6.3: *schematic description of RCDs in F-CNPs acting as incident light absorbers, reducing the fluorescence background in final digital pictures.*

In Figure A6.2c, the intensity the B channel obtained from each non-optically filtered image is plotted as a function of the test solution pH. The intensity of the B channel is taken here as a monitoring variable for the calibration procedure. This approach is preferred to the analysis of colorimetric coordinates (L^*, a^* and b^*) because they display more complex relationships with RCD dispersion parameters ($C_{RCDs}^{\%v/v}$ and pH). Conversely, the B channel intensities allowed a very direct monitoring of the effect of changing $C_{RCDs}^{\%v/v}$ and pH in the pristine RCD dispersion. To achieve a quantitative assessment of these dependences, the normalized B channel intensities were fitted using the following equation as model:

$$y = B + A \exp\left(\frac{x}{2.3026}\right) \tag{A6.1}$$

where y represents the normalized B channel intensity and x the test solution pH, B is a background factor and A is a pre-exponential constant. The use of this model stems from the simple premise that the fluorescence quenching is linearly dependent on the concentration of added H+. This assertion can be validated from the quenching experiment shown in Figure 6.3. A more formal derivation of the same formula can also be made using static quenching theory [84].

The results of this fitting procedures were employed to quantify the obtained pH sensing performances in the following way: B was taken as a measure to estimate the background in the fluorescence data, while other pH sensing characteristics (dynamic range, sensitivity, pH measurement resolution) were estimated evaluating the errors of interpolation on the x axis from the fitted curve. Such interpolation errors (σ) were calculated with a 95% accuracy in different pH ranges, as shown in Table A6.2.

Table A6.2: fitting parameters employed to estimate optimal conditions for the RCDs dispersions used in CNPs functionalization for pH sensing, namely the presence of background noise in the fluorescence data (B) and the resolution of pH measurement as the 95% confidence errors of interpolation on x axis (σ), calculated at the indicated pH values or ranges.

RCD Dispersion Code	B ($\times 10^{-1}$)	σ (pH≤4)	σ (pH = 4.5)	σ (pH=5.5)	σ (pH = 6)
ML0705	8.1±0.4	>1	>1	>1	>1
ML0720	4.6±0.2	>1	>1	>1	>1
ML0805	7.5±0.2	>1	>1	>1	>1
ML0810	4.2±0.5	>1	0.9	0.7	0.65
ML0820	5.3±0.3	>1	>1	0.95	0.8
CB1005	8.1±0.4	>1	>1	>1	>1
CB1020	4.7±0.4	>1	>1	0.95	0.7

From this analysis it can be observed that the background noise can be optimized acting on $C_{RCD}^{\%v/v}$. In fact, RCD dispersions with $C_{RCD}^{\%v/v} = 5\%$ result in a high background noise, having a B generally higher than at least 0.75. On the other hand, higher RCD concentration such as 10 and 20% can lower the observed background up to around 0.4-0.5. First, it should be noted that increases of $C_{RCD}^{\%v/v}$ in the tested range do not produce variations of neither the B nor the G channel intensity, being in the calibration range where the dependency of fluorescence intensity from RCD concentration is flat (Sec. 6.1.1, Figure 6.4). In turn, the increase of $C_{RCD}^{\%v/v}$ can help the extinction of the spurious fluorescence background. This can be explained considering that increasing $C_{RCD}^{\%v/v}$ increases the concentration of absorbers in the aqueous phase, leading to an attenuation of fluorescence stray light (Figure A6.3).

The pH of pristine RCD dispersion further influences the pH sensing characteristics, regulating the protonation of –CO⁻ groups of the constituent molecules of the nanoparticles (Sec. 3.2.8). A pH of 7 is not capable of producing a

sufficient pH sensitivity for all the tested $C_{RCD}^{\%v/v}$. A pH of 8 or 10 and $C_{RCD}^{\%v/v}$ of 10-20% is necessary to achieve pH sensing, making the dispersions ML0810, ML0820 and CB1020 the most suitable. Specifically, considering all the combinations of $C_{RCD}^{\%v/v}$ and the buffered pH (Table A6.1), and the quantitative evaluation in Table A6.2, ML0810 results as the pristine RCD dispersion leading to the highest accuracies in the largest pH dynamic range. This can be explained considering the pH and $C_{RCD}^{\%v/v}$ conditions of this dispersion as a good compromise between fluorescence intensity (and hence high signal-to-noise ratio in the images), pH dynamic range and resolution.

In contrast to conditions of pristine RCD dispersion, picture acquisition parameters, such as the shutter speed, produced feeble variations of normalized B channels. As an example, Figure A6.6 shows the B channel intensities for the dispersion ML0810 acquired at shutter speed of 0.2, 0.3 and 0.5 s.
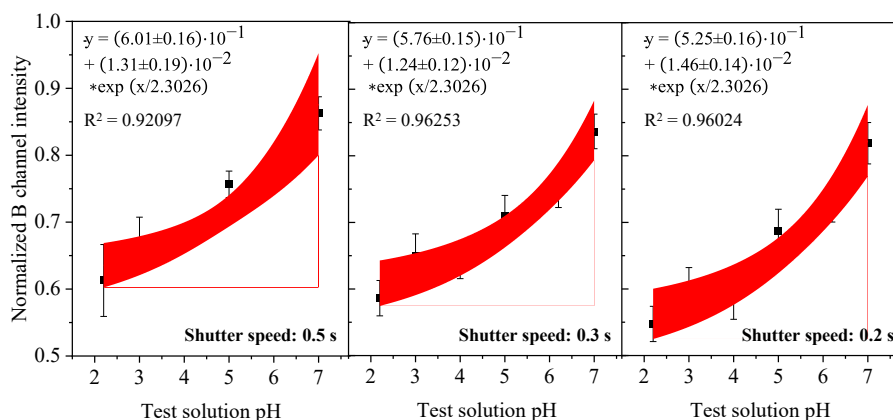

Figure A6.4: *normalized B channel intensity as a function of test solution pH (black squares), fitting curve (red lines) and 95% confidence interval (red shaded area) for the ML0810 dispersion obtained at shutter speeds of 0.5 s (left), 0.3 s (center) and 0.2 s (right); the insets show the fitting parameters within the model equation (A6.1) and the R^2 coefficient of the fitting. The intensities are normalized dividing by the B channel intensity of the test solution at pH 8 used as reference; error bars are calculated as standard deviations considering three replicates of the same experiment.*

As it can be observed, the fitting parameters did not undergo considerable variation as a function of the shutter speed. Therefore, the resulting sensing performances, such as those listed in Table A6.1 were negligibly affected by exposure time in the 0.2-0.5 s range, compared to variations of $C_{RCD}^{\%v/v}$ and pH of the pristine RCD dispersion.

In principle, the fitted curves in Figure A6.4 could be used for pH determination in a single-channel fluorescence strategy. However, as observed in Table A6.2, also in the most optimized conditions, the pH resolution, measured as 95% confidence errors of interpolation on x axis is not higher than ±0.7 pH units. It is worth noting that also the trends of L* obtained from CIELAB colorimetric analysis of F-CNP fluorescence (Sec. 6.1.2) as a function of test solution pH could be fitted using (A6.1) as model equation, similarly to the normalized B channel intensities (Figure A6.5).
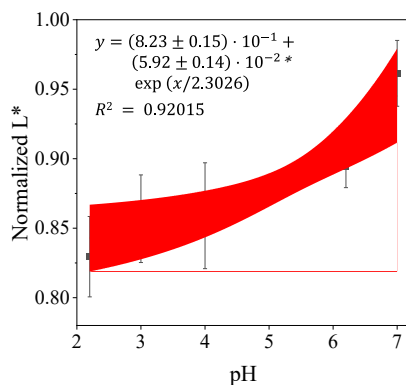

The plot shows normalized L* versus pH, with the fitting equation:
$$y = (8.23 \pm 0.15) \cdot 10^{-1} + (5.92 \pm 0.14) \cdot 10^{-2} * \exp(x/2.3026)$$
$$R^2 = 0.92015$$

Figure A6.5: *normalized L* as a function of test solution pH (black squares), fitting curve (red line) and 95% confidence interval (red shaded area) obtained for shutter speed of 0.5 s. Normalization of L* is performed by diving for the L* of the internal reference sample at pH = 8.*

This observation can be easily elucidated by recognizing that in the present case, both L* and B channel intensities are directly proportional to the overall fluorescence intensity collected from the F-CNPs. However, also considering L* does not result in very high performance in terms of achievable pH resolution. In fact, calculating the pH resolution from interpolation of fitted curve Figure 6.6 reveals a resolution that does not exceed ±1 pH unit.

References

[1] R. Hinojosa-Meza, E. Olvera-Gonzalez, N. Escalante-Garcia, J.A. Dena-Aguilar, M. Montes Rivera, P. Vacas-Jacques, Applied Sciences 12 (2022) 7038.

[2] L. Manjakkal, S. Dervin, R. Dahiya, RSC Advances 10 (2020) 8594–8617.

[3] M.T. Ghoneim, A. Nguyen, N. Dereje, J. Huang, G.C. Moore, P.J. Murzynowski, C. Dagdeviren, Chemical Reviews (2019).

[4] W. Xiao, Q. Dong, Catalysts 12 (2022) 1124.

[5] Y. Tang, L. Zhong, W. Wang, Y. He, T. Han, L. Xu, X. Mo, Z. Liu, Y. Ma, Y. Bao, S. Gan, L. Niu, Membranes 12 (2022) 504.

[6] R. Kumar, H. Nguyen, B. Rente, C. Tan, T. Sun, K.T.V. Grattan, Micromachines 13 (2022) 1224.

[7] M. Al-Jeda, E. Mena-Morcillo, A. Chen, Micromachines 13 (2022) 2143.

[8] T.C.P. Veettil, B.R. Wood, Sensors 22 (2022) 4528.

[9] A.M. Pisoschi, A.F. Danet, S. Kalinowski, Journal of Analytical Methods in Chemistry 2008 (2009) e937651.

[10] K. Benadouda, S. Sajid, S.F. Chaudhri, K.J. Tazally, M.M.K. Nielsen, B.K. Prabhala, Beverages 9 (2023) 5.

[11] R. Ghosh, P. Kline, BMC Research Notes 12 (2019) 268.

[12] W. Bae, T.-Y. Yoon, C. Jeong, PLOS ONE 16 (2021) e0247326.

[13] J. Wachlmayr, C. Hannesschlaeger, A. Speletz, T. Barta, A. Eckerstorfer, C. Siligan, A. Horner, Nanoscale Advances 4 (2022) 58–76.

[14] W.F. Watson, R. Livingston, The Journal of Chemical Physics 18 (2004) 802–809.

[15] Y. Song, S. Zhu, S. Xiang, X. Zhao, J. Zhang, H. Zhang, Y. Fu, B. Yang, Nanoscale 6 (2014) 4676–4682.

[16] J. Wang, Y. Yang, X. Liu, Materials Advances 1 (2020) 3122–3142.

[17] F. Zu, F. Yan, Z. Bai, J. Xu, Y. Wang, Y. Huang, X. Zhou, Microchim Acta 184 (2017) 1899–1914.

[18] C. Wei, S. Hu, F. Liang, Z. Song, X. Liu, Chinese Chemical Letters 33 (2022) 4116–4120.

[19] C.J. Reckmeier, J. Schneider, Y. Xiong, J. Häusler, P. Kasák, W. Schnick, A.L. Rogach, Chem. Mater. 29 (2017) 10352–10361.

[20] J. Schanda, International Commission on Illumination, eds., Colorimetry: Understanding the CIE System, CIE/Commission internationale de l'eclairage ; Wiley-Interscience, [Vienna, Austria] : Hoboken, N.J, 2007.

[21] J. Schanda, in: M.R. Luo (Ed.), Encyclopedia of Color Science and Technology, Springer, New York, NY, 2016, pp. 185–188.

[22] J. Guo, L. Qiu, Z. Deng, F. Yan, Polym. Chem. 4 (2013) 1309–1312.

[23] (n.d.).

[24] J. Noiphung, M.P. Nguyen, C. Punyadeera, Y. Wan, W. Laiwattanapaisal, C.S. Henry, Theranostics 8 (2018) 3797–3807.

[25] Y. Li, Y. Wang, S. Chen, Z. Wang, L. Feng, Analytica Chimica Acta 1154 (2021) 338275.

[26]   H. Zhang, A. Hou, K. Xie, A. Gao, Sensors and Actuators B: Chemical 286 (2019) 362–369.

[27]   N. Lopez-Ruiz, V.F. Curto, M.M. Erenas, F. Benito-Lopez, D. Diamond, A.J. Palma, L.F. Capitan-Vallvey, Anal. Chem. 86 (2014) 9554–9562.

[28]   K. Huo, J. Zhang, T. Lin, Y. Zhang, Y. Liu, X. Liu, Dyes and Pigments 219 (2023) 111574.

[29]   L. Wang, M. Li, W. Li, Y. Han, Y. Liu, Z. Li, B. Zhang, D. Pan, ACS Sustainable Chem. Eng. 6 (2018) 12668–12674.

[30]   D. Öztürk, İ. Ömeroğlu, B. Köksoy, C. Göl, M. Durmuş, Dyes and Pigments 205 (2022) 110510.

[31]   Z. Yan, X. Zhang, C. Bao, H. Tang, Q. Zhao, L. Hu, J. You, Sensors and Actuators B: Chemical 262 (2018) 869–875.

[32]   T. Taweetanavanich, B. Wanno, T. Tuntulani, B. Pulpoka, C. Kaewtong, J Chinese Chemical Soc 66 (2019) 493–499.

[33]   T. Lee, H.-T. Lee, J. Hong, S. Roh, D. Yeon Cheong, K. Lee, Y. Choi, Y. Hong, H.-J. Hwang, G. Lee, Analytical Methods 14 (2022) 4749–4755.

[34]   N. Pourreza, H. Golmohammadi, Talanta 131 (2015) 136–141.

[35]   O.R. Chanu, A. Kapoor, V. Karthik, Materials Today: Proceedings 40 (2021) S64–S68.

[36]   E.V. Ermakova, A.V. Bol'shakova, A. Bessmertnykh-Lemeune, Sensors 23 (2023) 2978.

[37]   T.H. Nguyen, T. Venugopala, S. Chen, T. Sun, K.T.V. Grattan, S.E. Taylor, P.A.M. Basheer, A.E. Long, Sensors and Actuators B: Chemical 191 (2014) 498–507.

[38]   K. Abe, K. Suzuki, D. Citterio, Anal. Chem. 80 (2008) 6928–6934.

[39]   J. Ling, G. Naren, J. Kelly, T.S. Moody, A.P. de Silva, J. Am. Chem. Soc. 137 (2015) 3763–3766.

[40]   A. Abdollahi, A. Mouraki, M.H. Sharifian, A.R. Mahdavian, Carbohydrate Polymers 200 (2018) 583–594.

[41]   S. Movafaghi, M.D. Cackovic, W. Wang, H. Vahabi, A. Pendurthi, C.S. Henry, A.K. Kota, Advanced Materials Interfaces 6 (2019) 1900232.

[42]   J. Yang, Z. Li, Q. Jia, Sensors and Actuators B: Chemical 297 (2019) 126807.

[43]   Biosensors and Bioelectronics 231 (2023) 115290.

[44]   M. Olszowy-Tomczyk, Chem. Pap. 75 (2021) 6157–6167.

[45]   A.F. Danet, in: Antioxidants - Benefits, Sources, Mechanisms of Action, IntechOpen, 2021.

[46]   N. Bibi Sadeer, D. Montesano, S. Albrizio, G. Zengin, M.F. Mahomoodally, Antioxidants 9 (2020) 709.

[47]   J. Du, J.J. Cullen, G.R. Buettner, Biochimica et Biophysica Acta (BBA) - Reviews on Cancer 1826 (2012) 443–457.

[48]   D. Njus, P.M. Kelley, Y.-J. Tu, H.B. Schlegel, Free Radical Biology and Medicine 159 (2020) 37–43.

[49]   X. Yin, K. Chen, H. Cheng, X. Chen, S. Feng, Y. Song, L. Liang, Antioxidants (Basel) 11 (2022) 153.

[50]   B.A. Wagner, G.R. Buettner, Advances in Redox Research 9 (2023) 100077.

[51]   G.B. Golubitskii, E.V. Budko, E.M. Basova, A.V. Kostarnoi, V.M. Ivanov, J Anal Chem 62 (2007) 742–747.

[52] J. Campbell, W.G. Tubb, Can. J. Res. 28e (1950) 19–32.

[53] B.H.J. Bielski, A.O. Allen, H.A. Schwarz, J. Am. Chem. Soc. 103 (1981) 3516–3518.

[54] T. Koutchma, Ozone: Science & Engineering 30 (2008) 93–98.

[55] A.P. Demchenko, Methods Appl. Fluoresc. 8 (2020) 022001.

[56] P.-T. Chou, A.U. Khan, Biochemical and Biophysical Research Communications 115 (1983) 932–937.

[57] S. Saha, M.N. Roy, in: A.H. Hamza (Ed.), Vitamin C, InTech, 2017.

[58] R.H. Bisby, C.G. Morgan, I. Hamblett, A.A. Gorman, J. Phys. Chem. A 103 (1999) 7454–7459.

[59] R.J. Wilson, A.E. Beezer, J.C. Mitchell, Thermochimica Acta 264 (1995) 27–40.

[60] T.-S. Yang, D.B. Min, Journal of Food Science 74 (2009) C718–C722.

[61] A.A. Khalil, A.A. Khan, A. Khalid, Z. Abid, C. Proestos, Z.F. Bhat, M.U. Shahbaz, R.M. Aadil, Ultrasonics Sonochemistry 98 (2023) 106534.

[62] V. Spínola, E.J. Llorent-Martínez, P.C. Castilho, Journal of Chromatography A 1369 (2014) 2–17.

[63] H.S. Farah, J.F. Alhmoud, A. Al-Othman, K.M. Alqaisi, A.M. Atoom, K. Shadid, A. Shakya, T. AlQaisi, Systematic Reviews in Pharmacy 11 (2020).

[64] R.I. Dave, N.P. Shah, International Dairy Journal 7 (1997) 435–443.

[65] C. Shang, T. Zhang, J. Xu, N. Zhao, W. Zhang, M. Fan, Food Chemistry: X 19 (2023) 100790.

[66] A.-L. Herbig, C.M.G.C. Renard, Food Chemistry 220 (2017) 444–451.

[67] M. Sultana, E.S. Chan, P. Janarthanan, W.S. Choo, LWT 188 (2023) 115388.

[68] A. Wagner, S. Dussling, A. Nowak, L. Zimmermann, P. Bach, M. Ludwig, K. Kumar, F. Will, R. Schweiggert, C.B. Steingass, Eur Food Res Technol 249 (2023) 1771–1784.

[69] Md.A. Wazed, Md.A.M. Sheikh, Md. Akhtaruzzaman, Md.S. Awal, N.H.M.R. Mozumder, Journal of Agriculture and Food Research 14 (2023) 100773.

[70] E. Jeney-Nagymate, P. Fodor, British Food Journal 110 (2008) 296–309.

[71] A. Chawla, A. Lobacz, J. Tarapata, J. Zulewska, Applied Sciences 11 (2021) 7285.

[72] R. Quevedo, J.M. Bastías, T. Espinoza, B. Ronceros, I. Balic, O. Muñoz, R. Quevedo, J.M. Bastías, T. Espinoza, B. Ronceros, I. Balic, O. Muñoz, Scientia Agropecuaria 11 (2020) 257–266.

[73] T. Koutchma, Food Bioprocess Technol 2 (2009) 138–155.

[74] I. Kijpatanasilp, K.A. Shiekh, S. Jafari, R.W. Worobo, K. Assatarakul, Foods 12 (2023) 2725.

[75] W.A. Bazaraa, H.A. Eissa, S.A. Helmy, M.T. Ramadan, R.M. Aboelhaggag, Food Sci. Technol. Int. 29 (2023) 757–764.

[76] S. Basak, L. Shaik, S. Chakraborty, Food Chemistry Advances 2 (2023) 100333.

[77] C.-W. Liao, M.-C. Hung, C.-Y. Wang, B.-Y. Chen, LWT 183 (2023) 114887.

[78] T.C. McIlvaine, Journal of Biological Chemistry 49 (1921) 183–186.

[79] C. Parolo, A. Sena-Torralba, J.F. Bergua, E. Calucho, C. Fuentes-Chust, L. Hu, L. Rivas, R. Álvarez-Diduk, E.P. Nguyen, S. Cinti, D. Quesada-González, A. Merkoçi, Nat Protoc 15 (2020) 3788–3816.

[80]   D. Calabria, M. Guardigli, P. Severi, I. Trozzi, A. Pace, S. Cinti, M. Zangheri, M. Mirasoli, Sensors 21 (2021) 5432.

[81]   M. Arciuli, G. Palazzo, A. Gallone, A. Mallardi, Sensors and Actuators B: Chemical 186 (2013) 557–562.

[82]   J.S. Gomes, R.M.F. de Sousa, J.F. da S. Petruci, Anal. Methods 14 (2022) 2471–2478.

[83]   A. Sena-Torralba, R. Álvarez-Diduk, C. Parolo, A. Piper, A. Merkoçi, Chem. Rev. 122 (2022) 14881–14910.

[84]   J.R. Lakowicz, Principles of Fluorescence Spectroscopy, 3rd ed., Springer US, 2006.

Concluding remarks

To summarize, this study addressed some of the unsolved issues in the preparation of CDs and on their widespread adoption in technological devices.

Three synthetic strategies were examined. In the synthesis of DCDs, *in-situ* PEI passivation produced CDs with an intense red PL component, providing a significant improvement of the solvothermal synthetic methods that use citric acid and urea as precursors. The synthesis of RCDs in open vessel enabled accurate monitoring of emitting species formation reactions, providing unique insights into the chemical mechanisms governing the emission properties of CDs. Finally, the synthesis of NR-CDs set up an innovative approach in which the final CDs properties can be designed a-priori through accurate selection of the molecules used as carbonaceous source.

Investigations of PB resistance of CDs led to pinpoint interesting relationships between nanoparticle chemical composition and resistance to photodegradation, which is a key technological aspect, as well as investigating the role of molecular fluorophores in nanoparticle emission. Combining colloidal chemistry methods and ultrafast spectroscopy, coupling of AuNPs with CDs was shown to produce a remarkable enhancement of red emission component of CDs. This work emphasized the coupling CDs with metal nanoparticles in nano-hybrids as effective post-synthetic strategy for enhancement of CDs optical properties.

The outstanding optical properties of CDs, combined with their AIQ resistance were employed for validating their feasibility for applications in optoelectronic and photonic based devices. Lasing and RL action was demonstrated for NR-CDs, while both NR-CDs and DCDs were successfully exploited for the fabrication of color-converting layers for potential application in WLEDs. Moreover, for DCDs, a combined numerical and experimental investigation of their colorimetric properties proved their viability for implementation in these devices.

Finally, the pH and ROS sensitivity of RCDs was suitably employed and combined with a smartphone-based fluorescence colorimetric detection to develop a portable chemical sensing platform for analyses of pH and AOC. The sensing device not only shows high resolution in pH detection and good qualitative AOC of evaluation capabilities but is also potentially easily integrable for automated detections and remote environments.

The obtained results provide substantial new insight on several aspects of the synthesis and the optical properties of this fascinating class of innovative nanomaterials and demonstrate their versatility in a wide range of applications.